Image-guided Simulation for Augmented Reality during Hepatic Surgery

Nazim Haouchine

To cite this version:

Nazim Haouchine. Image-guided Simulation for Augmented Reality during Hepatic Surgery. Computer Science [cs]. Université de Lille1, 2015. English. NNT : . tel-01254439v2

HAL Id: tel-01254439

https://inria.hal.science/tel-01254439v2

Submitted on 22 May 2022

Thesis submitted to obtain the title of
Doctor of Philosophy of the
University of Lille 1

Doctoral School of Engineering Science
Field: Computer Science

Image-guided Simulation for Augmented Reality during Hepatic Surgery

Prepared at **Inria** by

NAZIM HAOUCHINE

Defended on January 26^{th} 2015

Jury members:

Advisors:	Stephane COTIN	Research Director, Inria
	Marie-Odile BERGER	Research Director, Inria
Co-advisor:	Jeremie DEQUIDT	Associate Professor, Lille University
Reviewers:	Adrien BARTOLI	Professor, Auvergne University
	Jocelyne TROCCAZ	Research Director, CNRS
Examiners:	Danail STOYANOV	Senior Research Fellow, University College London
	Nassir NAVAB	Professor, Technische Universitat Munchen
President:	Gery CASIEZ	Professor, Lille University

ABSTRACT

Image-guided Simulation for Augmented Reality during Hepatic Surgery

Abstract: The main objective of this thesis is to provide surgeons with tools for pre and intra-operative decision support during minimally invasive hepatic surgery. These interventions are usually based on laparoscopic techniques or, more recently, flexible endoscopy. During such operations, the surgeon tries to remove a significant number of liver tumors while preserving the functional role of the liver. This involves defining an optimal hepatectomy, i.e. ensuring that the volume of post-operative liver is at least at 55% of the original liver and the preserving at hepatic vasculature. Although intervention planning can now be considered on the basis of preoperative patient-specific, significant movements of the liver and its deformations during surgery data make this very difficult to use planning in practice. The work proposed in this thesis aims to provide augmented reality tools to be used in intra-operative conditions in order to visualize the position of tumors and hepatic vascular networks at any time. To achieve this we propose the following main steps:

- Modeling the liver biomechanics (and deformations due to breathing motion), and the inclusion of the pressure created by blowing Co2 during surgery.
- Tracking features points on the surface of the liver in the endoscopic images and perform 3D reconstruction of the liver surface.
- Visualization of internal structure during the intervention, taking into account the intra-operative deformations.
- Real-time non-rigid registration of 3D liver model on the laparoscopic image.

Keywords: Image-guided Simulation, Biomechanical Modeling, Real-Time Augmented Reality, Computer Assisted Surgery, Minimally Invasive Surgery, Visual Tracking, 3D Reconstruction, Non-rigid Registration.

RÉSUMÉ

Simulation Guidée par l'Image pour la Réalité Augmentée durant la Chirurgie Hépatique

Résumé:

L'objectif principal de cette thèse est de fournir aux chirurgiens des outils d'aide à la décision pré et per-opératoire lors d'interventions minimalement invasives en chirurgie hépatique. Ces interventions reposent en général sur des techniques de laparoscopie ou plus récemment d'endoscopie flexible. Lors de telles interventions, le chirurgien cherche à retirer un nombre souvent important de tumeurs hépatiques, tout en préservant le rôle fonctionnel du foie. Cela implique de définir une hépatectomie optimale, c'est à dire garantissant un volume du foie post-opératoire d'au moins 55% du foie initial et préservant au mieux la vascularisation hépatique. Bien qu'une planification de l'intervention puisse actuellement s'envisager sur la base de données pré-opératoire spécifiques au patient, les mouvements importants du foie et ses déformations lors de l'intervention rendent cette planification très difficile à exploiter en pratique. Les travaux proposés dans cette thèse visent à fournir des outils de réalité augmentée utilisables en conditions per-opératoires et permettant de visualiser à chaque instant la position des tumeurs et réseaux vasculaires hépatiques. Pour y parvenir nous proposons les étapes principales suivantes :

- Modélisation de la biomécanique du foie (déformations et mouvement dû à la respiration), ainsi que la prise en compte de la pression créé par insufflation de Co2 durant l'intervention.
- Suivi de points caractéristiques sur la surface du foie dans les images endoscopiques et Reconstruction 3D de la surface du foie.
- Visualisation de la planification lors de l'intervention en prenant en compte les déformations per-opératoires.
- Recalage temps réel non rigide du modele 3D du foie sur l'image.

Mots-clés: Réalité Augmentée, Simulation Biomechanique Temps Réel, Chirurgie Minimallement Invasive, Reconstruction 3D, Suivi Visuel, Chirurgie Guidée par l'Image, Recalage non-rigid.

LIST OF PUBLICATIONS

Below is a partial list of my publications. Only the publications which were produced while I was working on my PhD between 2012 and 2014 are listed.

Journal Papers

[1] N. Haouchine, S. Cotin, I. Peterlik, J. Dequidt, M. Sanz Lopez, E. Kerrien and M.-O. Berger. *Impact of Soft Tissue Heterogeneity on Augmented Reality for Liver Surgery*. Visualization and Computer Graphics, IEEE Transactions on, 2014b **- *Presented at Siggraph Asia 2014* -**

[2] N. Haouchine, J. Dequidt, A. Bilger, M.-O. Berger and S. Cotin. *Elastic Augmented Reality from a Single View*. Visualization and Computer Graphics, IEEE Transactions on (Submitted), 2015

International Conference Papers

[3] N. Haouchine, J. Dequidt, E. Kerrien, M.-O. Berger and S. Cotin. *Physics-based Augmented Reality for 3D Deformable Object*. In *VRIPHYS - Virtual Reality Interaction and Physical Simulation*, pages 31–38, Darmstadt, Germany, 2012

[4] N. Haouchine, J. Dequidt, M.-O. Berger and S. Cotin. *Deformation-based Augmented Reality for Hepatic Surgery*. In *MMVR 20 - Medecine Meets Virtual Reality*, pages 182–188, San Diego, USA, 2013a

[5] N. Haouchine, J. Dequidt, I. Peterlik, E. Kerrien, M.-O. Berger and S. Cotin. *Image-guided simulation of heterogeneous tissue deformation for augmented reality during hepatic surgery*. In *Mixed and Augmented Reality (ISMAR), 2013 IEEE International Symposium on*, pages 199–208, 2013b **- *Best Paper Award : Honourable Mention* -**

[6] N. Haouchine, J. Dequidt, I. Peterlik, E. Kerrien, M.-O. Berger and S. Cotin. *Towards an Accurate Tracking of Liver Tumors for Robotic Assisted Surgery*. In *Robotic and Automotion (ICRA), 2014 IEEE International Conference on*, 2014d

[7] N. Haouchine, J. Dequidt, M.-O. Berger and S. Cotin. *Single View Augmentation of 3D Elastic Objects*. In *Mixed and Augmented Reality (ISMAR), 2014 IEEE International Symposium on*, 2014c **- *Top Ranked Paper* -**

[8] J. Bosman, N. Haouchine, J. Dequidt, I. Peterlik, S. Cotin and C. Duriez. *The Role of Ligaments: Patient-Specific or Scenario-Specific ?* In *International Symposium on Biomedical Simulation 2014*, 2014

[9] R. Plantefeve, N. Haouchine, J.-P. Radoux and S. Cotin. *Automatic Alignment of pre and intraoperative Data using Anatomical Landmarks for Augmented Laparoscopic Liver Surgery*. In *International Symposium on Biomedical Simulation 2014*, 2014

[10] H. Talbot, N. Haouchine, J. Dequidt, I. Peterlik, C. Duriez, H. Delingette and S. Cotin. *Surgery Training, Planning and Guidance Using the SOFA Framework*. In *Eurogrpahics 2015, Medical Prize (Accepted)*, 2015 ***- Eurographics Medical Prize Winner -***

National (French) Conference Papers

[11] N. Haouchine, S. Cotin, J. Dequidt, E. Kerrien and M.-O. Berger. *Réalité augmentée pour la chirurgie minimalement invasive du foie utilisant un modèle biomécanique guidé par l'image*. In *Reconnaissance de Formes et Intelligence Artificielle (RFIA) 2014*, 2014a **(in french)**

CONTENTS

CHAPTER 1

GENERAL INTRODUCTION

Liver diseases cause around 700.000 deaths worldwide per year [WHO]. The increasing number of deaths due to liver diseases has encouraged the medical community, scientific groups as well as governments to take actions to reduce this number.

Considerable advances in medicine have seen the emergence of new surgery techniques such as Minimally Invasive Surgery (MIS). In this technique, the surgeon does not interact directly with organs but with instruments via trocars inserted through small incisions on the abdomen. The surgeon can observe these instruments on a monitor retrieving a video stream captured by an endoscopic camera inserted through the navel. This is obviously less painful for the patient and the healing period is shorter. In addition, bleeding and risks of infection are considerably reduced. This is why MIS techniques are nowadays widely used. Despite MIS procedure is considered as a well-established technique, it remains quite complex from a surgical skill standpoint, mainly because of the poor visual feedback and due to the loss of direct manipulation. To enrich this visual feedback, several solutions have been proposed in the literature. The introduction of optics in the abdomen has naturally led the research community to investigate the use of Augmented Reality (AR) to guide the surgeon during the procedure. Indeed, internal structures, such as tumors and vessels, can be modeled from pre-operative data and superimposed on the intra-operative image, offering an elegant and effective solution to reduce the surgical complexity.

The work presented in this thesis focuses on the elaboration of an AR framework for guidance and assistance during MIS. Several works in this field have been proposed, with elegant approaches and convincing results. These approaches are however limited to rigid organs, or consider the deformations negligible, which is, in practice not a valid assumption, especially when dealing with the liver, considered as a hyper-elastic organ. We aim at bringing a solution that permits to establish a coherent AR system that takes into account soft-tissue deformations. This is done by combining processing of image data acquired with a camera (that allows to achieve important tasks such as 3D reconstruction and tracking of organs) and modeling liver deformations using real-time simulation (that faithfully translate liver behaviour). We show throughout this manuscript, with both theoretical and practical elements, that our method can be a viable solution to this problem.

Manuscript Organisation

This thesis is organized progressively from the modeling of soft-tissue behaviour and the analysis of endoscopic images to the development of an augmented reality framework for hepatic surgery capable of handling elastic liver behaviour.

Chapter 2 introduces the three major fields that were studied during this thesis: *i)* Minimally invasive hepatic surgery where we first describe the liver, its anatomy, its pathology and its surgery and then introduce some techniques of Computer Assisted Surgery, *ii)* Biomechanical simulation of living tissues, where we give the necessary background concerning computational mechanics and its application to medical simulation and *iii)* Surgical vision, where we describe the techniques proposed in the literature for estimating deformable organ motion and shape.

Chapter 3 we propose an efficient real-time algorithm for recovery and augmentation of highly elastic objects in a single view context. Using a rough estimation of the material elasticity and the adequate boundary constraints, large deformations can be efficiently handled. We present experiments in a general context where various elastic objects are used since a ground truth can easily be computed, and in the context of augmented reality for minimally invasive liver surgery with surgical data.

Chapter 4 we present an approach that relies on the computation of image information acquired with stereo endoscopic camera, to drive a heterogeneous mechanical model capable of faithfully translating the liver behaviour. Our approach for three-dimensional liver surface reconstruction is introduced where we present a clusters-based filter that aims to add robustness to temporal tracking of liver deformations. The biomechanical liver model that accounts for vessels heterogeneity is described and our non-rigid registration approach expressed as an energy minimization is introduced.

Chapter 5 , we confront our framework against three experimental scenarios. First, we demonstrate with computer-generated data whether and where an heterogeneous model differs from an homogeneous one for the prediction of tumor location. Second, our approach is tested on an actual laparoscopic procedure performed on a human liver, allowing us to qualitatively estimate how our approach could perform in a real surgical environment. Third, we rely on a realistic phantom liver to quantitatively measure the error between simulation and ground truth. We further propose several strategies to add robustness to visual tracking, and we discuss the importance of the material stiffness in the modeling liver soft-tissue.

Chapter 6 concludes this thesis and opens new research directions such as initial alignment of pre- and intra-operative data, intuitive visualization of volumes during augmentation and handling occlusions that may hinder the visual tracking.

CHAPTER 2

RESEARCH BACKGROUND

Contents

2.1 Introduction

The work presented in this thesis focuses on the elaboration of an augmented reality framework for the guidance and assistance of surgeons during minimally invasive surgery. Several works in this field have been proposed, with elegant approach and convincing results. These methods share a common ground: processing data derived from cameras (or similar sensors). The analysis of these data has permitted the understanding of surgical scenes and the achievement of important tasks such as 3D reconstruction, tracking of organs and surgical tools, as well as the estimation of the camera pose and the detection of critical regions of interest such as vessels.

One of the characteristics of a surgical scene is the deformation of soft-tissue organs. Thus, the proposed methods that aim to establish a coherent augmented reality framework in surgery have tried to incorporate such a characteristic in their algorithm following several strategies. These studies mainly cover the heart and kidneys, and this, because the deformation occurs in a quasi-rigid or cyclical manner, which allows to model the deformation in a robust manner. Nevertheless, when dealing with hepatic surgery, elastic and unpredictable deformations occur. The inclusion of these deformations are essential in the elaboration of our framework. We introduce, in addition to vision analysis, the modeling and simulation of mechanical behaviour of the liver.

We present in this chapter, the three major fields that were studied throughout this thesis: Minimally invasive hepatic surgery and Computer Assisted Surgery, biomechanical simulation of living tissues and surgical vision. We first describe the liver, its anatomy, pathology and surgery. We then describe the current techniques proposed in the literature for estimating soft-tissue organ motion and shape. Finally, we give the necessary background concerning computational mechanics and its application to medical simulation.

2.2 Hepatic Surgery

This section covers hepatic surgery, including the liver anatomy and diseases and recent techniques used in operating rooms for the liver surgery. First, the liver anatomy is briefly described, where only the aspects modeled in our study are highlighted i.e. texture for visual tracking, ligaments for boundary conditions and vessels representing the main source of heterogeneity. Hepatic diseases are then addressed and the liver surgery is described to introduce minimally invasive hepatic surgery. Finally, a brief overview of computer-assisted surgery techniques is given.

2.2.1 Liver Anatomy

The liver is a vital organ normally present in the human body, in the upper right quadrant of the abdomen Maton et al. (1994). The liver has a wide range of functions, including detoxification of various metabolites, protein synthesis, and the production of biochemicals necessary for digestion. The liver is necessary for survival, and there is currently no way to compensate the absence of the liver functions in the long term, although new liver dialysis techniques can be used in the short term.

Structure and texture The liver is a roughly triangular organ which extends across the entire abdominal cavity just inferior to the diaphragm. Most of the liver's mass is located on the right side of the body where it descends inferiorly towards the right kidney. The liver is made of very soft, pinkish-brown tissues encapsulated by a connective tissue capsule. This capsule is further covered and reinforced by the peritoneum of the abdominal cavity, which protects the liver and holds it in place within the abdomen.

The liver consists of 4 distinct lobes - the left, right, caudate, and quadrate lobes (cf Figure 2.1).

- The left and right lobes are the largest lobes and are separated by the falciform ligament. The right lobe is about 5 to 6 times larger than the tapered left lobe.
- The small caudate lobe extends from the posterior side of the right lobe and wraps around the inferior vena cava.
- The small quadrate lobe is inferior to the caudate lobe and extends from the posterior side of the right lobe and wraps around the gallbladder.

Connections to surrounding organs The peritoneum connects the liver in 4 locations: the coronary ligament, the left and right triangular ligaments, and the falciform ligament. Anatomically, these connections are not true ligaments; rather, they are condensed regions of peritoneal membrane which supports the liver.

- The wide coronary ligament connects the central superior portion of the liver to the diaphragm.
- Located on the lateral borders of the left and right lobes, respectively, the left and right triangular ligaments connect the superior ends of the liver to the diaphragm.
- The falciform ligament runs inferiorly from the diaphragm across the anterior edge of the liver to its inferior border. At the inferior end of the liver,

the falciform ligament forms the round ligament (ligamentum teres) of the liver and connects the liver to the umbilicus. The round ligament is a remnant of the umbilical vein which carries blood into the body during foetal development.

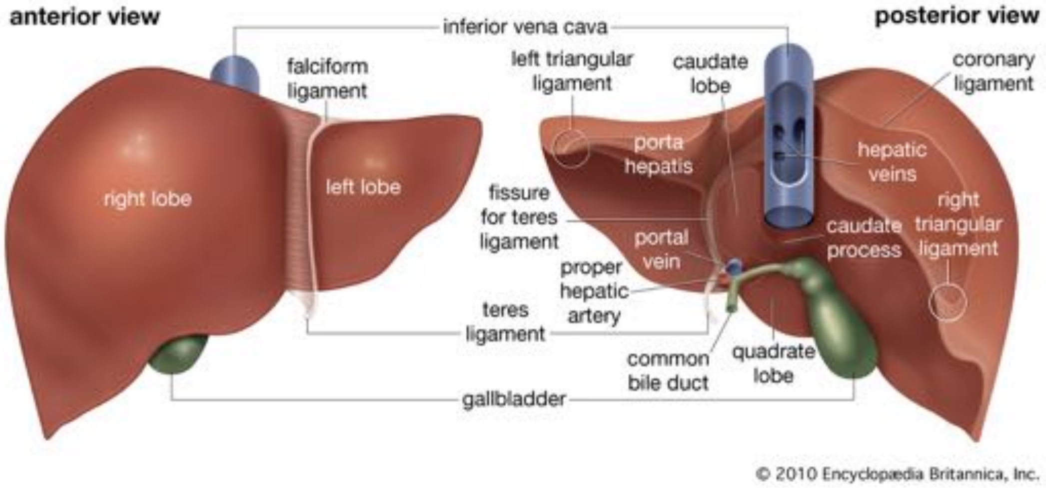

© 2010 Encyclopædia Britannica, Inc.

Figure 2.1: Human Liver Anatomy (Encyclopedia Britannica).

The tubes which carry the bile through the liver and gallbladder are known as bile ducts and they form a branched structure known as the biliary tree. The bile produced by liver cells drains into microscopic canals known as bile canaliculi. The countless bile canaliculi come together into many larger bile ducts found throughout the liver.

Vascular Network The blood supply of the liver is unique among all organs of the body due to the hepatic portal vein system. Blood travelling to the spleen, stomach, pancreas, gallbladder, and intestines passes through capillaries in these organs and is collected into the *hepatic portal vein.* The hepatic portal vein then delivers blood to the liver tissues where the content of the blood is divided up into small vessels and processed before flowing throughout the rest of the body. The blood going out of the liver tissues is collected in the hepatic veins which lead to the *vena cava* and return to the heart. The liver also has its own system of arteries and arterioles which provide oxygenated blood to its tissues just like any other organ.

The internal structure of the liver is made of around 100.000 small hexagonal functional units known as lobules. Each lobule consists of a central vein surrounded by 6 hepatic portal veins and 6 hepatic arteries.

2.2.2 Liver Diseases and Cancer

Liver diseases (also called hepatic diseases) are caused by the perturbation of any liver function that causes illness. The liver is responsible for many critical functions within the body. The loss of those functions can cause significant damage to the body. There are more than a hundred kinds of liver diseases, the most spread one are : Hepatitis, fatty liver disease, alcoholic liver disease and Cirrhosis. These diseases can form several types of tumors that cause liver cancer. The liver can be affected by primary liver cancer, which arises from the liver, or by cancers which form in other parts of the body and then spread to the liver. Most liver cancers are secondary or metastatic, meaning it started elsewhere in the body. At this stage, the surgery, either with resection (removal of the tumor) or a liver transplant, offers the only reasonable chance to cure liver cancer.

A surgery where a part of the liver is removed is called *partial hepatectomy*. This operation is attempted only if the patient is healthy enough for surgery and all of the tumor can be removed while enough healthy liver can be left. Unfortunately, most liver cancers cannot be completely removed. Often, the cancer is in too many different parts of the liver, is too large, or has spread beyond the liver.

When it is available, a liver transplant may be the best option for small liver cancers. At this time, liver transplants can be an option for those with tumors that cannot be removed with surgery, either because of the location of the tumors or because the liver is too affected for the patient to withstand removing part of it. In general, it is used to treat patients with small tumors (either 1 tumor smaller than 5 cm across or 2 to 3 tumors no larger than 3 cm) that have not invaded nearby the blood vessels.

2.2.3 Minimally Invasive Hepatic Surgery

In the last decades, considerable advances in medicine have seen the emergence of Minimally Invasive Surgery (MIS) (also called laparoscopic surgery). In this procedure, surgical instruments and an endoscopic camera are inserted into the abdominal cavity through small incisions (usually 5 mm - 15 mm) in contrast to open surgery where incisions are larger. The surgeon manipulates these instruments by watching a monitor displaying a video stream acquired from the endoscopic camera (see Figure 2.2).

Procedure

Under general anaesthesia, the procedure requires a few small incisions in the abdomen (cf figure 2.3), which are used as trocar ports. Usually two to four plastic trocars of 11 mm and 12 mm diameter are placed to insert rigid surgical instruments. Another trocar is needed for the laparoscopic camera, which gives a magnified view of the instruments and anatomy. The surgeon selects all ports

Figure 2.2: Surgeons perform laparoscopic stomach surgery

by palpation of external anatomic landmarks. The optimal choice of the instrument ports provides full access to the whole operation region as well as adequate surgeon dexterity.

The key element in laparoscopic surgery is the laparoscope. Usually, it has an oblique 30° optic to gain a wider perspective by rotating it about its own axis. This is especially useful when inserting the laparoscope camera relatively parallel to an organ surface and for looking behind objects Stephen and Eubanks (2004). To provide better visualization and exposure to the surgeons, CO_2 is insufflated into the abdomen to enlarge the surgeon's working volume (cf figure 2.3). This gas is used because it is common to the human body and can be absorbed by the tissues and removed by the respiratory system Peng et al. (2009). It is also non-flammable, this is important because electrosurgical devices are commonly used in laparoscopic procedures.

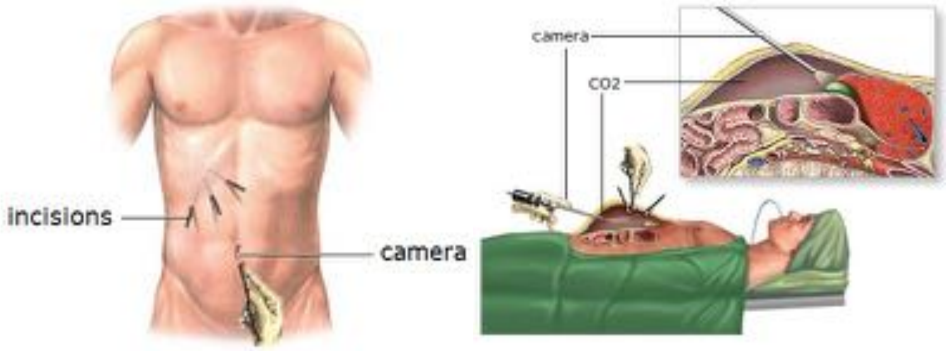

(a) **(b)**

Figure 2.3: Minimally Invasive Surgery procedure: (a) Incisions for laparoscopic surgery and (b) CO2 insufflated into the abdomen and camera insertion.

There are two types of laparoscopic camera : a *telescopic rod lens system*, that is usually connected to a video camera (single chip or three chips with high horizontal image resolution of more than 750 lines), or a *digital laparoscope* where the charge-coupled device is placed at the end of the laparoscope, eliminating the rod lens system. Also attached is a fibre optic cable system connected to a ’cold’ light source (halogen or xenon), to illuminate the operative field, inserted through a 5 mm or 10 mm cannula or trocar to view the operative field Janie Fuller et al. (2003). The laparocopic camera is equipped with a cold light to illuminate the working space as illustrated in Figure 2.4.

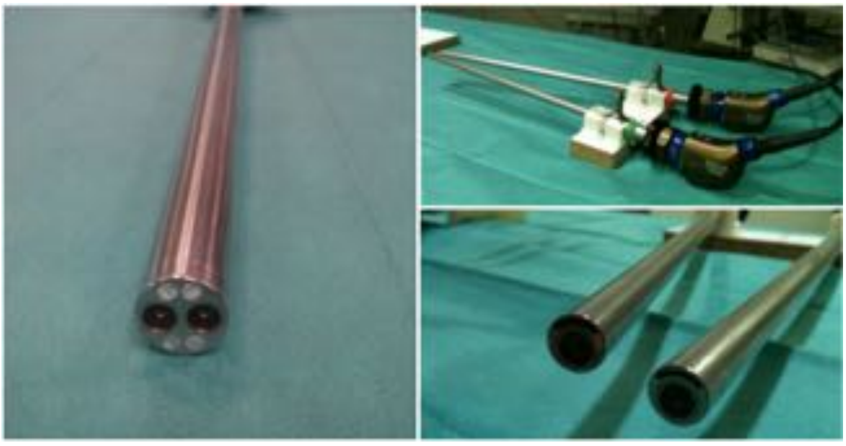

Figure 2.4: Stereo endoscope of the Da Vinci robot and two mounted monocular camera from Karl Stroz Endoscopy.

Benefits and outcomes

Although open surgery is still very common, many procedures are now performed with minimally invasive techniques for their advantages for the patient (reduced pain and short recovery time). From a surgical skill standpoint these procedures are quite complex mainly because the visual feedback is relatively incomplete or poor and due to the loss of direct organ manipulation.

The main advantage of laparoscopic surgery Stephen and Eubanks (2004) is the reduction of hemorrhaging, minimizing the need for blood transfusion. In addition, the small incisions reduce the exposure of internal organs to possible external contaminants thus decreasing the risk of infections.

While laparoscopic surgery is clearly advantageous in terms of patient outcomes, the procedure is more difficult from the surgeon’s perspective when compared to traditional open surgery Marvik et al. (2005). Indeed, the surgeon has a limited range of motion and suffers from a poor depth perception. In addition, the surgeon must use tools to interact with organs rather than manipulating them directly with its hands. The tool endpoints move in the opposite direction to the surgeon's hands due to the pivot point, making laparoscopic surgery a non-intuitive procedure Janie Fuller et al. (2003). These disadvantages lead to the emergence of new techniques to help and assist the surgeon during MIS known as Computer Assisted Surgery.

2.3 Computer Assisted Surgery

Computer assisted surgery (CAS) also known as computer assisted intervention (CAI) or image guided surgery (IGS) uses advanced techniques in robotic and computer science to improve the surgical procedures and provide decision support Marvik et al. (2005). The assistance can take several forms : pre-processing of scanned data using image processing techniques, robotic surgery and telesurgical procedure, surgical simulation for planning and diagnosis, and surgical navigation. In practice, these fields cannot be dissociated and can be used together at several stages (pre-operatively, and intra-operatively) to facilitate the procedure.

Figure 2.5: Robotic-Assistance Surgery : ZEUS surgical plateform (left) and Da Vinci plateform (right).

2.3.1 Robotic-assisted Surgery

Surgery has greatly benefited from advances in robotics Hungr et al. (2012). The major advance of the last decades is the introduction of teleoperated surgical platforms for MIS. These plateforms permit to control a slave robot (which holds the surgical tools and the endoscope) from a distant master console that transmits the surgeons gesture.

Currently, only two commercial platforms have been developed (illustrated in Figure 2.5) the Zeus Robot from Computer Motion and the DaVinci Robot from Intuitive Surgical (nowadays the DaVinci platform is the only commercially available surgical platform).

Such platforms provide surgeons with superior visualization, enhanced dexterity, precise movements and ergonomic confort, making it possible for complex surgical procedures to be performed in a minimally invasive fashion. Their current limitations reside mostly in restoring haptic feedback and visualization enhancement Westebring et al. (2008).

2.3.2 Virtual patient

Creating a virtual image of the patient is considered as the most important component of CAS with well-established imaging modalities, such as ultrasound, MRI, CT, X-rays L. Soler (2000). The patient virtual image is essential for diagnosis in medical procedures and pre-operative planning. With the emergence of new techniques of imaging and the advances in image processing as well as computer graphics, medical imaging quickly muted to 3D data visualization and fusion, trying to offer the surgeon enriched information and the possibility to visualize organs of the patient in 3D (see Fig 2.6-a).

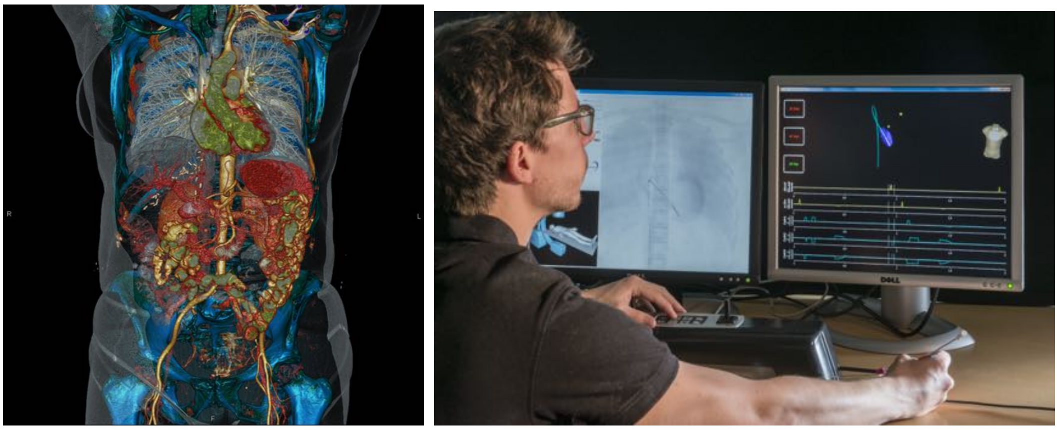

(a) (b)

Figure 2.6: Computer Assisted Surgery : (a) 3D virtual patient built from CT Imaging (b) VR Simulator for Cardiology Training.

2.3.3 Surgical Simulation

The main purpose of medical simulation is to properly train students in different medical fields using advanced technology. In addition, around 100.000 deaths are recorded annually due to medical mistakes, medical simulation can be a solution to reduce this number. We can find in the literature several research studies on medical simulation Marescaux et al. (1997); Ayache et al. (1998); Talbot et al. (2014); Selmi et al. (2013) as well as commercial simulators dedicated to training for different types of surgery (see Fig 2.6-b). In addition to training, medical simulation can be used pre-operatively, to plan surgical procedures or intra-operatively during surgeries as a decision support, where it appears to be an essential aspect of tomorrow's surgery.

2.3.4 Augmented Reality for Surgery

One of the aims of surgical navigation is to provide surgeons with enriched visual feedback while performing interventions. It can be used for example to avoid critical areas such as vessels or to highlight the position of a tumour during an hepatectomy. With the advances in surgical vision and the ability to compute virtual organs pre-operatively, Augmented Reality has been considered as a suitable technology for CAS and leads the community to propose several methods to bring AR in surgery.

Augmented Reality (AR) is the synthesis of real and virtual imagery. In contrast to Virtual Reality (VR), in which the user is immersed in an entirely artificial world, AR overlays extra information on real scenes. AR could overlay simple highlights, arrows or text labels into the user's view or more complicated graphics like 3D models or animations Klein (2006). Ronald Azuma offered a definition Azuma (1997) that Augmented Reality combines real and virtual and is interactive, real time and registered in 3D.

One of the first studies on Augmented Reality for laparoscopy was proposed by Fuchs et al. Fuchs et al. (1998). This work focused on AR visualization for laparoscopic surgery by the extraction of depth from the laparocopic camera. In the context of surgical guidance, Suthau and Hellwich (2002) presented a concept work for AR in medical applications using a Head-Mounted Display. Since then, a number of medical AR systems have implemented the concept. In the MEDARPA (MEDical Augmented Reality for Patient) Wesarg S. (2004), an AR system to support MIS, only rigid transformations between the pre and intra-operative images were considered and computed from markers attached to the patient's body. Marescaux et al. Marescaux (2004) reported the first real-time AR-assisted laparoscopic adrenalectomy using manually assisted deformable registration. Yet many challenges remain unsolved in order to obtain real time fully automatic registration methods for deformable organs without the need to fix markers on the patient. A number of techniques have been proposed to increase accuracy of tracking and registration of AR systems in surgery. A hybrid tracking method for surgical augmented reality was proposed by Fischer et al. Fischer et al. (2007). Still in the context of rigid registration, the system combines IGS equipment for infrared tracking and image-based tracking and is capable of superimposing tumor in video see-through AR and tracking instruments.

Most of the early contributions are dedicated to rigid organs or assume that elastic deformations between pre-operative and intra-operative data are negligible. In practice, large elastic deformations may occur due to breathing or due to the interaction of the organ with the surgeon's tools. Past attempts to perform AR on deformable organs made use of markers or navigation aids placed close to the area of navigation targets Teber et al. (2009) or required interaction to refine elastic registration between pre and intra-operative data Nicolau et al. (2011). Others Figl et al. (2010) built pre-operatively a dynamic 4D model of the heart which is registered to intra-operative data using ECG. Su et al. (2009) proposed a 3D-3D iterative closest point (ICP) registration with an image-based tracking to superimpose the 3D model onto laparoscopic images for kidney partial resection. Since kidney do not actually undergo elastic deformations during surgery the 3D-3D registration is performed in a rigid manner. These methods have shown the feasibility of automatic AR systems in surgery but put constraints on the operating room, required interaction or are dedicated to specific - i.e. cyclic-deformations.

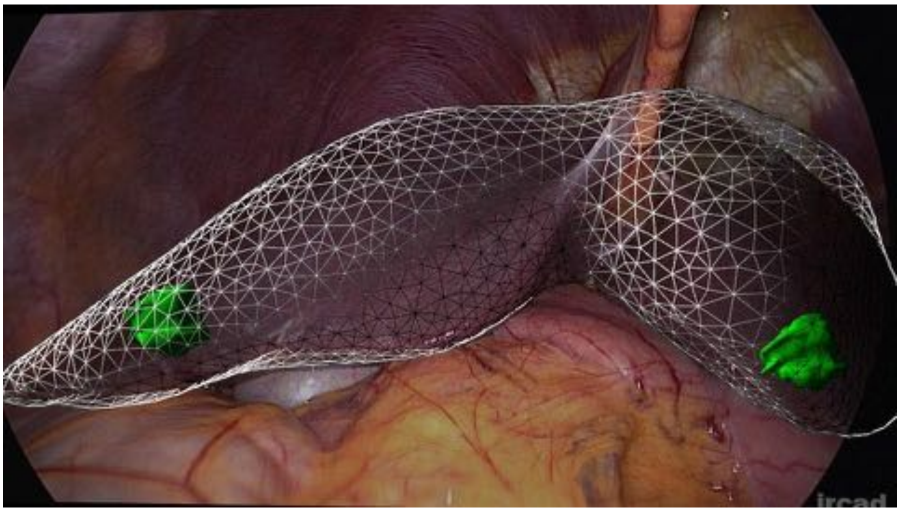

Figure 2.7: Augmented reality for laparoscopic liver surgery. The purpose behind AR in surgery is to visualize internal structures such as tumors, superimposed on the video stream, in 3D and in real-time.

Recently, significant advances have been realized towards automatic registration between pre and intra-operative data in MIS. In the context of laparoscopy and with monocular images, Kim et al. (2012a) proposed a robust solution to track and augment a deformable surgical site using shape from shading and conformal mapping. However, their method only retrieves surface deformation and cannot ensure an accurate augmentation of inner structures. Puerto-Souza et al. Puerto-Souza and Mariottini (2013) proposed a matching algorithm called Hierarchical Multi-Affine capable of long-term tracking for augmentation during partial nephrectomy. This approach estimates a set of affine transformations from clusters of features in order to relocate occluded or missing features for a coherent spatio-temporal mesh registration.

Computer Assisted Surgery appears to be an essential aspect of tomorrow's surgery, it becomes necessary in most of medical routines. These techniques where proved to be efficient in pre-operative context, mainly in the processing of virtual image of patient. However, they still have limits to deploy intra-operatively, where the procedure complexity makes it challenging to guarantee a successful surgery assistance. Augmented Reality has the potential to become a well-established technique for surgical navigation. In the last decades, significant advances have been made in this area both theoretically and practically, with real case studies. But most of the contributions do not consider non-rigid behaviour of organs, which can be highly damaging when targeting medical applications where accuracy is critical. We propose in this thesis to bring simulation in the operating room, by performing augmented reality taking into account elastic behaviour of human organs. We show that with this combination internal structures such as tumors can be accurately located by propagating surfacic liver motion acquired form laparoscopic camera. Thus, this combination involves two main domains: Processing of laparoscopic image with advanced surgical vision techniques, and simulation of liver elasticity using mechanically-based approaches.

2.4 Surgical Vision

Processing image data of the targeted environment is the first step towards an Augmented Reality application. With the emergence of MIS and the introduction of optics in the surgical procedure routines, computer vision techniques naturally appear as an appropriate support for surgical navigation and guidance. Thus, in the last decades, several research groups have investigated new methods and approaches to understand surgical scenes. Among all the specialization that appeared in this field, the most widely studied one is the estimation of organ motion.

Estimating organ motion involves two main steps: 3D reconstruction of organ shapes and its temporal visual tracking. In the following we give an overview of actual techniques for shape recovery during MIS, using several types of acquisition modality, and we describe the current techniques proposed for a robust and accurate visual tracking of organ soft-tissue. In this section, these two steps are addressed where we only focus on estimating the organ shape and motion. Surgical instrument tracking Allan et al. (2013) is not covered here.

2.4.1 Three-dimensional Shape Recovery

Many methods have attempted to recover 3D information on the organ from intra abdominal images, these methods can be divided into two main categories (see Figure 2.8): active techniques where the image is enriched to facilitate its processing, like projecting patterns or lights. Generally, this enriching is done through hardware modifications on optical devices or additional sensors, and passive techniques that only rely on processing endoscopic images where no additional information is needed. Both active and passive techniques have advantages and disadvantages and have been studied by the community.

Active Techniques

In order to acquire distance information during laparoscopic surgery, Penne *et al.* Penne et al. (2009) introduced Time-of-Flight technique (ToF) via endoscope optics. By measuring the time that the signal takes between the camera and the target object (for instance an organ), this approach is able to perform depth measurement at 20 fps. One of the advantages of ToF approach is that it requires a small range to build a depth map which can be suitable knowing the restricted working space of laparoscopic surgery. However, the *in-vivo* tests Groch et al. (2012) recently performed suggest that ToF camera is not yet significant for clinical uses.

Another active method used in laparoscopic surgery is Structured Light Maurice et al. (2011); Albitar et al. (2007). In this method, a known pattern is projected onto the organ using a calibrated projected, the projected image is acquired with a monocular camera and processed in order to reconstruct 3D shape of the targeted object. The projector and optical sensor can be mounted on the same endoscopic device or can be separated. In both cases, it consists of a detection-correspondence-triangulation step. This method gives accurate and robust 3D reconstruction, and performs well in case of featureless tissue, which can be of interest for surgical context. Nevertheless, the quite heavy hardware modifications and their cost make this technique not practical and hardly applicable.

Photometric Stereo Collins and Bartoli (2012a); Herrera et al. (2013) has recently been introduced as an alternative to strong hardware tuning. This method aims to reconstruct surface normals of an object with images taken from the same viewpoint under several illumination conditions. Based on a standard monocular laparoscope modified with three colour filters (red, green and blue) placed at its tip (without physical dimension changes), Collins and Bartoli

(2012a) propose to extend PS to closed-range constraint for 3D Reconstruction in Laparoscopy. This method, tested on *in-vivo* pig liver, gives significant 3D reconstruction and represents a practical and very inexpensive solution. However, its major limitation consists of the illumination perturbation that may occur when dealing with highly reflective organs such as the liver.

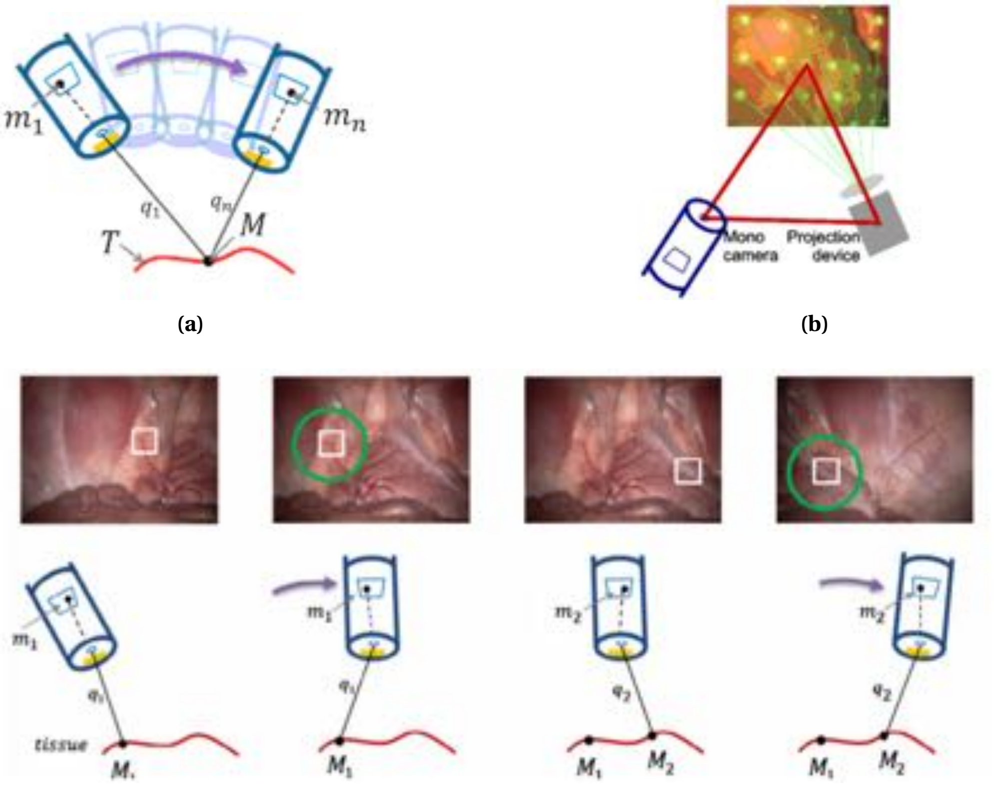

(a) (b)

(c)

Figure 2.8: Three-dimensional organs shape recovery with (a) structure from motion, (b) structured light and (c) simultaneous localisation and mapping. (Courtesy of Maier-Hein et al. (2013))

Passive Techniques

Since passive techniques are based on processing endoscopic images, the proposed methods for 3D reconstruction are mainly inspired by classic computer vision algorithms. However, where computer vision techniques perform well on non-surgical data, visual complexity of the intra-abdominal scene makes the direct translation of these algorithms difficult without a specific tuning and additional visual cues.

Stereoscopy in MIS has been widely studied in the last decades Stoyanov et al. (2005); Stoyanov (2012); Richa et al. (2010a); Su et al. (2009); Chang et al. (2013); Rohl et al.; Pratt et al. (2010), with very effective methods and significant results, it currently represents the most feasible technique for 3D reconstruction when dealing with *in-vivo* data. Sparse 3D reconstruction was studied for robotic assisted intervention Stoyanov et al. (2005) as well as for registration purpose Su et al. (2009), using stereo correspondence to register sparse 3D shape of targeted organs with pre-operative 3D models. Using a growing seed technique, Stoyanov et al. Stoyanov (2012) are able to perform dense reconstruction on *in-vivo* data. By imposing spatial and temporal constraints, this method is able to reconstruct dense 3D scene flow accurately and efficiently. This dense reconstruction is based on the propagation of information starting from a sparse set of candidate seed matches. The growing scheme also permits to reject outliers and ensures uniqueness and symmetry in the estimated flow. This method has been improved using convex optimisation Chang et al. (2013) to face texture-less area issues. Other techniques Richa et al. (2010a,b) take advantage of motion template in order to handle deformations and reduce specular highlight issue by ensuring a temporal consistency.

Many of the exposed techniques can achieve real-time thanks to GPU implementation and have been tested on *ex-vivo* and *in-vivo* data, making stereoscopy a promising technique for 3D liver reconstruction during MIS. Nevertheless, robustness regarding specular highlights, texture-less organ tissues and occlusions remain its major limitations, in addition to disturbance coming from smoke and blood that may highly affect the stereo-matching. Moreover, despite the fact that the stereo-endoscopic devices (DaVinci Camera or Karl Storz Camera) are currently used in clinical routine, they are rarely used compared with classical monocular laparoscopic cameras. This can be explained by the fact that in the early days of MIS, stereoscopic technology was not mature enough to be considered in the Operating Rooms.

To overcome the need of stereo-endoscope, several monocular-based approaches have been proposed, these methods take advantage of camera motion to simulate multiple camera or exploit shading properties of the organ.

Hu et al. (2007) proposed to use Structure-from-Motion (SfM) in laparoscopic surgery for 3D reconstruction of environment from multiple endoscopic views. In this method, false feature correspondences are detected by imposing trilinear constraints using three images instead of classical epipolar constraints between two images. The use of Simultaneous Localisation and Mapping (SLAM) in laparoscopy was studied by Mountney et al. (2006). One of the main advantages of SLAM is that with the several observations of a particular environment the uncertainty of 3D reconstruction can be modelled and reduced.

Both SfM and SLAM assume a rigid environment, which is not the case when dealing with laparoscopic liver surgery, where deformations from breathing and heart beating occur. For that purpose, deformable SfM has been introduced to handle the non-rigid organ behaviour Collins and Bartoli (2011) and cyclic motion model for cardiac and respiratory motion was incorporated into SLAM framework Mountney and Yang (2010) to predict organ deformations. While these techniques show promising results, their real robustness and accuracy are not yet assessed.

With a laparoscopic camera surrounded by a light source, Shape-from-Shading techniques have naturally appeared as a feasible solution. By using shading and specular information acquired from a single image view, and an appropriate light model, 3D shape of organs can be recovered Collins and Bartoli (2012b) in surgical context. In this study, a non-parametric light model is used allowing the modeling of different endoscopic cameras. However, complex reflectance properties of the organ tissues make the exploitation of shading not practical. To improve reconstruction and homogenize the recovered 3D shape, an alternative solution which combines SfS with SfM Malti et al. (2012) has recently been proposed, making a step forward for future research.

2.4.2 Visual Tracking of Organ Tissue

Visual tracking aims to temporally locate the position of the targeted organ and to provide the evolution of tissue behaviour over time (cf Figure 2.9). Depending of the needs, these positions can be in 2D deduced directly form images, or in 3D where a reconstruction stage is required.

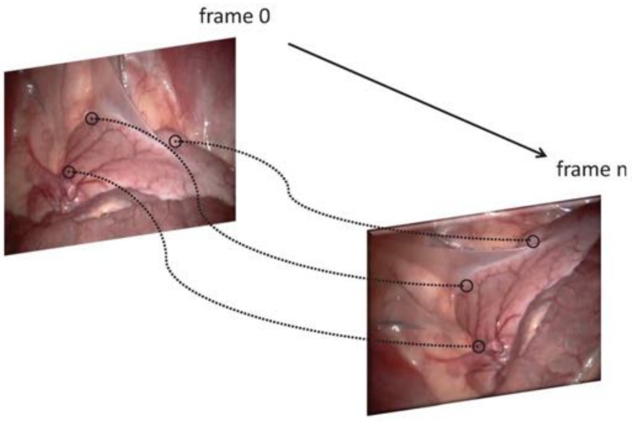

Figure 2.9: Tracking tissue locations in endoscopy (courtesy of Yip et al. (2012))

The main contribution in this area relies on the detection of salient landmarks (or features) on the surface of the organ (see Figure 2.10). Features detection is an important research area in computer vision, where a large number of feature detectors have been proposed Mikolajczyk et al. (2005) and tested on MIS data Mountney et al. (2010). Once the landmarks are selected, an algorithm for searching correspondences over frames is usually applied. These correspondences can be found using an assumption on the organ motion in two consecutive frames Stoyanov (2012), or by searching for image similarities (*feature matching*) between the frames Puerto and Mariottini (2012).

Endoscopic images represent a quite complex data for computer vision, since the presence of specular highlight and instrument may disturb the tracking. For that reason, the research community has focused on providing accurate and robust methods for long-term tracking. To do so, hybrid methods have been proposed to counteract the unreliability of each single method. In Stoyanov et al. (2005) a combination of maximally stable extremal regions (MSER) Matas et al. (2004) and the traditional gradient based image features Shi and Tomasi (1994) is used for salient landmark selection. These landmarks are tracked using a modified Lucas-Kanade optical flow Lucas and Kanade (1981a) extended to stereoscopic images. This approach was further improved by incorporating the scale invariant feature transform (SIFT) Lowe (2004a) to increase tracking robustness Richa et al. (2010a). In Elhawary and Popovic (2010a), a simple combination of the speeded up robust feature (SURF) Bay et al. (2008) method and optical flow algorithm is proposed for heart surface tracking.

To cope with occluded regions, Puerto-Souza *et al.* Puerto (2011) proposed a Hierarchical Multi-Affine matching algorithm capable of long-term tracking for augmentation during partial nephrectomy. This approach estimates a set of affine transformations from clusters of features in order to relocate missing features to obtain a coherent spatio-temporal mesh registration.

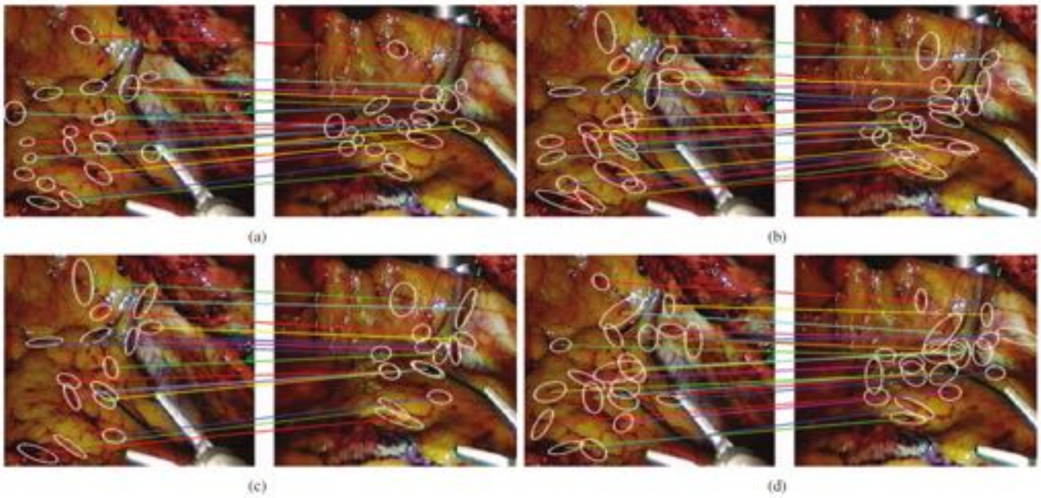

Figure 2.10: Detectors and Descriptors with the (a) Affine-Invariant Anisotropic Region detector (b) Harris-Affine (c) Hessian-Affine (d) MSER. (courtesy of Giannarou et al. (2013))

Other techniques rely on the use of temporal or physical models to avoid occlusion by a prediction step Pratt et al. (2010). Using spatio-temporal constraints, Richa *et al.* Richa et al. (2010c) proposed to exploit the quasi-periodicity of heart beating motion to reduce tracking disturbances by using time-varying dual Fourier series as a prediction model that also permits to handle occluded surface.

Features algorithms that exhibited the highest density and temporal persistency are the SIFT and SURF, both in terms of detector Mikolajczyk et al. (2005) and descriptor Mikolajczyk and Schmid (2005). These methods can hardly achieve real-time processing required in intra-operative context. A recent evaluation Yip et al. (2012) reports that a combination of the STAR feature detector M. Agrawal and Blas (2008) and binary robust independent elementary features M. Calonder and Fua (2010), can perform in real-time while maintaining high feature density and tracking accuracy. Recently, Giannarou et al. (2013) proposed an affine-invariant anisotropic feature detector dedicated to surgical data. The detector is coupled with an Extended Kalman Filter (EKF) to allow accurate identification and matching, and the exploitation of a GPU implementation leads to reach real-time performance.

A wide range of feature detectors and descriptors have been developed by the computer vision community. The application of these techniques to surgical vision has faced significant limitations due to the complexity of surgical environment in terms of soft tissue deformation and changing visual appearance. To counteract these limitations, most of studies consider that the deformations are small or cyclic, thus they can be subject to a predictive model to detect and reduce outliers. When dealing with elastic liver this assumption can not be considered since large elastic deformations occur, and motion estimation is more prone to outliers. In this thesis, we propose a method for 3D reconstruction and tracking of liver deformations recovered from endoscopic images. This method is less prone to disturbance since it does not totally depend on images, but relies on geometrical processing of the reconstructed 3D point cloud. In addition, we take advantage of the ability of the liver biomechanical model to estimate deformations where no features are tracked, to reduce the density of features and apply very strict detection, matching and tracking filtering. Thus, a long-term tracking of 3D features is possible, permitting an efficient non-rigid registration.

2.5 Modeling Non-rigid Objects

The choice of an appropriate deformable model is important to model organ deformations. In this section we give a brief overview of popular methods used for the modeling of non-rigid objects. We mainly highlight the approaches which were adopted by computer vision, namely physically-based models, mass-spring systems, learned models and parametric shape warping.

2.5.1 Physically-based Models

that Mechanical models are very popular in both Computer Graphics and Computer Vision. Their ability to translate physical behaviour of objects with fidelity is a major feature for applications such as medical imaging Sermesant et al. (2003); Baumann et al. (2009) and medical simulation Courtecuisse et al. (2014). From a computer vision point of view, mechanical models have been used as regularization of image fitting taking into account erroneous measurements. For example, the Active Contour Models (Snakes) Kass et al. (1988a) attempt to minimize an external energy associated to image contour and and internal physical energy associated to the model. This method was extended to handle volume data Shen et al. (2011). In Schaerer et al. (2010), a dynamic model based on the equation of dynamics for elastic materials is proposed, where forces measured on the image drive the model towards object boundaries. The organ is supposed to be homogeneous and the forces measured on MRI volumes, though noisy, are available everywhere in the structure.

Most of the time, simple models based on linear elasticity are considered. For tracking heart beat Pratt et al. (2010) used a 4D scan of the heart coupled with a biomechanical model. It is controlled by surface constraints created by features extracted from a stereovision stream and allows quite accurate overlay of internal structures. This approach is however limited to cyclic movements where no large deformations nor surgeon manipulation occurs. In Speidel et al. (2011), intra-operative registration between stereo endoscopic images and pre-operative modeling of the liver based on biomechanical properties was proposed. A linear and a Neo-hookean elastic model are considered and the accuracy of registation is assessed on a phantom. The results are slightly better with the second model but the model is not suitable for real time simulation.

Mechanical models permit an accurate non-rigid registration while producing a coherent visual deformations. Their limitations reside in their complexity and their cost in computing. In addition, a prior knowledge of the object physical properties is necessary.

2.5.2 Mass-spring System

Mass-springs System is a very intuitive deformable model Miller (1988). In this model, the deformation is approximated by a set of point masses connected by massless springs. Instead of going through a discretization stage, the model offers directly a discrete model which only requires the solution of a system of coupled ordinary differential equations.

The main advantage of mass-spring system is its computational efficiency, where real-time can easily be achieved. Its disadvantage is that it generates non-realistic deformations. Indeed, it is difficult to link the stiffness of the springs to real physical parameters. Furthermore, mesh resolution impacts heavily on the deformations making the model mesh dependant. Despite these drawbacks, mass-spring systems are used by the research community Ibai et al. (2014) and in commercial medical simulators.

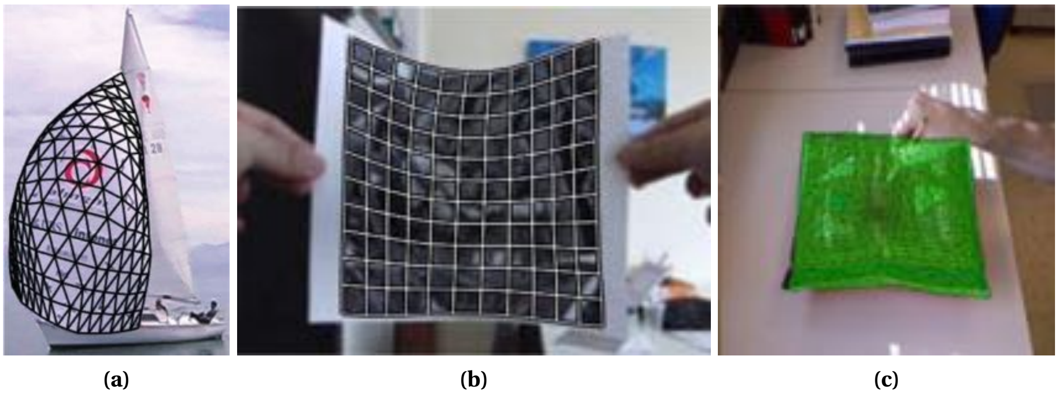
(a) (b) (c)

Figure 2.11: Deformable models: (a) Learned model Salzmann et al. (2007b) (b) Parametric model Bartoli (2008) (c) Mass-spring systems Ibai et al. (2014).

2.5.3 Learned Non-rigid Models

Instead of trying to estimate a deformation with unknown physical parameters, learning models permits to infer shape statistics from a training data which groups the possible shape configurations. These models have been used in computer vision for tracking 2D face deformations using Active Shapes Models Cootes et al. (1995) or Active Appearance Models Matthews and Baker (2004). They have also been used for 3D non-rigid shape recovery from a single view Salzmann et al. (2007b); Salzmann and Fua (2011).

Learned non-rigid models are considered very effective for many applications since they do not need a priori knowledge material parameters. However, when dealing with deformable surface, the mesh includes many degrees of freedom. Building a correct database that will define all the possible deformations with such a large number of degrees of freedom is an amount of work. As an alternative, many approaches rely on the use of a regularization of parametric shape models, aiming to reduce the number of mesh vertices using control points which interpolate the deformation in order to obtain a finer mesh description.

2.5.4 Shape Parametrization

Parametric models are widely used in computer vision as warps functions for image deformations. Where a large variety of warps functions exist in the literature, the most popular warps are those based on Radial Basis Functions (RBF) such as the Thin-Plate Spline (TPS) Bookstein (1989) and those based on the tensor-product, called Free-Form Deformations (FFD) Sederberg and Parry (1986) using cubic B-spline or Beziers volumes.

Thin-plate Spline is a radial basis function that specifies an approximation function which minimizes its internal bending energy. It has been successfully applied for modeling non-rigid surface Bartoli (2008) and has been extended from affine to projective transformations. The TPS is very attractive, thanks to its flexibility in placing control points which drive the deformation, thus recent works take advantage of TPS for the modeling of heart tissue deformation Richa et al. (2010a); Lim and Yang (12005).

The basic idea of Free-form Deformation model is to deform an object by manipulating an underlying mesh of control points. The resulting deformation controls the shape continuous of the 3D object and produces a smooth transformation. FFD's have been previously applied to tracking and motion analysis in medical imaging Rueckert et al. (1999) and non-rigid surface Bartoli and Zisserman (2004a); Pizarro and Bartoli (2012). The disadvantage of standard FFD is their lack of ability to model local deformations.

Shape Parametrization models are straightforward to implement in real-time and are flexible since they rely on the manipulation of the mesh nodes or outlying control points. Nevertheless, the absence of internal properties makes them unsuitable for creating realistic biomechanical deformations.

Depending on the application, several methods can be considered for modeling deformation. Mechanical models are used for application when the accuracy is critical such as medical non-rigid registration but rely on the prior estimation of the material parameters. Mass-spring systems are considered as a quasi-physical models and are widely used in computer graphics since they are intuitive and computationally fast. Nevertheless, they suffer from accuracy. One can use the learned models when dealing with a limited amount of deformations like human face deformations or parametric models that are very effective for inelastic non-rigid surfaces like papers or cloths, or for cyclic deformations such as heart beating. The last two are however dedicated to surface deformations.

Although, mechanical models are seldom reported in image-based non-rigid recovery since a prior knowledge of the material property is needed to correctly estimate the deformation, and are computationally expensive and most of the time very complex. They are the most suitable for the modeling of liver tissue where large, unpredictable deformations occur. Recent advances in medical simulation have permitted to reach a trade-off between stability, real-time achievement and accuracy which lead us to investigate their usability for medical augmented reality. In addition, we aim at augmenting the liver internal structures like tumors. Thus, a volumetric representation is necessary to propagate into the volume, the liver deformations processed from image data, for an accurate tumor localisation.

2.6 Physics-based Modeling

Our method involves the modeling and simulation of liver deformation, accounting for vessels and tumors. Simulation of liver tissue deformations has been studied both by computer graphic and medical simulation groups. The non-linear visco-elastic behaviour of the liver makes its modeling very challenging. In addition to the various features which have to be considered in order to correctly translate the behaviour of the liver tissue such as anisotropy, large deformations or tissue heterogeneity, the real-time aspects of the simulation is considered as one of the most important features in medical context. The real-time constraint leads the community to propose several deformable models to find the best compromise between stability, accuracy and performances.

In this section we give the necessary background concerning computational mechanics and its application to medical simulation. We first give definitions related to continuum mechanics, then we describe the Finite Element Method that discretizes the domain covering linear and non-linear models. Finally, time integration is treated and real-time approaches that permit medical uses are exposed.

2.6.1 Continuum Elasticity

The most common approach to describe the deformation of an object is the *Lagrangian* view (where fluids are commonly described by the *Eulerien View*). It permits to define a deformed object based on its initial (undeformed) state and by a set of material parameters that define the way it deforms under external loads.

Displacement field

The displacement field permits to determine for each particle in the initial configuration its position in the deformed configuration. Let us define the rest shape as a continuous connected subset M of $\mathbb{R}^3$, we call material coordinates, the coordinates $m \in M$ of a point in the object. The object leaves its rest shape to a deformed configuration when forces are applied, thus a point originally at location $\mathbf{m}$ will be defined by its new *spatial coordinates* at location $\mathbf{x}(\mathbf{m})$. Since new locations can be defined for all material coordinates $\mathbf{m}$, the vector field $\mathbf{x}$ can be defined on M. Otherwise, the deformation can also be specified by the *displacement* vector field $\mathbf{u}(\mathbf{m}) = \mathbf{x}(\mathbf{m}) - \mathbf{m}$ defined on M.

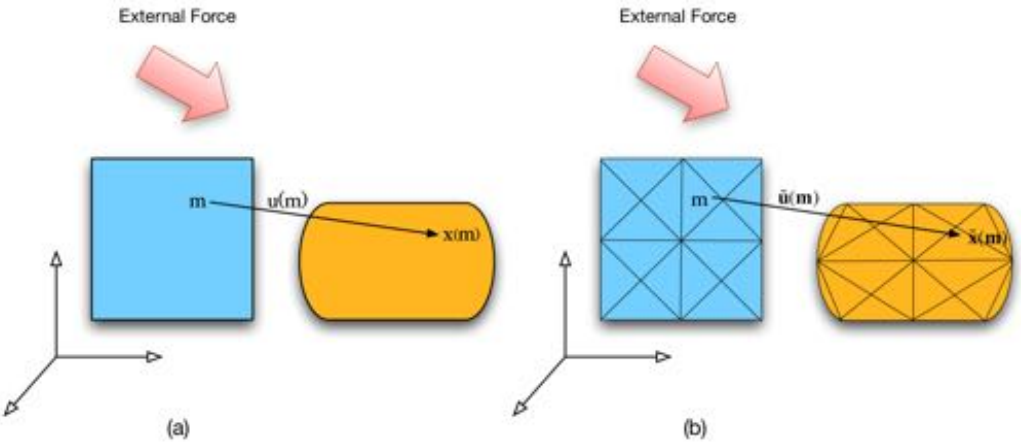

Figure 2.12: In the finite element method, a continuous deformation (left) is approximated by a sum of (linear) basis functions defined inside a set of finite elements (right)

Strain tensor

We introduce the notion of *strain tensor* (noted ε) reflecting the local deformations (elongation, compression, bending, twisting or shearing) of a displacement field at a given point in the field. The elastic strain tensor ε can be computed from $\mathbf{u}(\mathbf{m})$ (ε is a dimensionless quantity which, in the linear one-dimensional case, is simply $\Delta l / l$). That strain must be measured in terms of spatial variations of the displacement field $\mathbf{u} = \mathbf{u}(\mathbf{m}) = (u, v, w)^T$ since a spatially constant displacement field represents a translation of the object with no strain.

Several approaches exist in the literatures to compute the stress tensor. The reader may refer to Nealen et al. (2006), for a comparison of different stress tensors and their implication on the behaviour of objects. However, the two frequently used elastic strains in the field of real-time simulation are the Green's nonlinear strain tensor and the Cauchy's linear strain tensor:

$$\varepsilon_G = \frac{1}{2}(\nabla u + (\nabla u)^T + (\nabla u)^T \nabla u) \tag{2.1}$$

and

$$\varepsilon_C = \frac{1}{2}(\nabla u + (\nabla u)^T) \tag{2.2}$$

where the symmetric tensor $\varepsilon_G \in \mathbb{R}^{3\times3}$ is the Green's nonlinear strain tensor and $\varepsilon_G \in \mathbb{R}^{3\times3}$ its linearization, called Cauchy's linear strain tensor. The gradient of the displacement field is the 3 by 3 matrix below:

$$\nabla \mathbf{u} = \begin{bmatrix} \frac{\partial u}{\partial x} & \frac{\partial u}{\partial y} & \frac{\partial u}{\partial z} \\ \frac{\partial v}{\partial x} & \frac{\partial v}{\partial y} & \frac{\partial v}{\partial z} \\ \frac{\partial w}{\partial x} & \frac{\partial w}{\partial y} & \frac{\partial w}{\partial z} \end{bmatrix} \tag{2.3}$$

Stress tensor

Stress tensor defines the internal forces of the material that permit to maintain a coherent environment, for example, it ensures the inability to stretch or compress an object to infinity. In other words, the stress tensor $\sigma \in \mathbb{R}^{3\times3}$ defines the state of stress for each material point **m** in the deformed configuration. Under the Cauchy's law, internal forces of an object can be defined by its surface forces. Thus, Cauchy stress tensor σ maps the normal to a surface **n** to the traction vector **t** acting on that surface, according to:

$$\mathbf{t} = \mathbf{n} \cdot \sigma \tag{2.4}$$

where

$$\sigma = \begin{bmatrix} \sigma_{11} & \sigma_{12} & \sigma_{13} \\ \sigma_{21} & \sigma_{22} & \sigma_{23} \\ \sigma_{31} & \sigma_{32} & \sigma_{33} \end{bmatrix} \tag{2.5}$$

The Cauchy stress tensor refers to the current configuration, that is, it is a measure of force per unit area acting on a surface in the current configuration. Since this current configuration is not always known, one can use the *Piola-Kirchhoff tensor* which can express the stress from its rest shape.

Constitutive law

In practice, the strain tensor ε and the stress tensor σ are closely related. Indeed, the displacement of a point in the object will generate forces, which will constrain that displacement. This relation, called the *constitutive law* (or material law), depends on the material properties that are often experimentally obtained.

Linear Elasticy The most popular constitutive law in computer graphics is the Hooke's material law with a linearised Green-Lagrange tensor under the hypothesis that the displacements are small. This linear elastic law consider that the elongation is proportional to the force and is as follows:

$$\sigma = 2\mu\varepsilon + \lambda tr(\varepsilon) I \tag{2.6}$$

λ and μ are the Lamé coefficients that can be deduced from the Young Modulus E and the Poisson coefficient ν which belong to the material's physical properties:

$$\lambda = \frac{E\nu}{(1+\nu)(1-2\nu)} \qquad \mu = \frac{E}{2(1+\nu)} \tag{2.7}$$

$$E = \frac{\mu(3\lambda+2\mu)}{\lambda+\mu} \qquad \nu = \frac{\lambda}{2(\lambda+\mu)} \tag{2.8}$$

The Poisson coefficient describes the compressibility of the material (0: perfectly compressible, 0.5: perfectly incompressible) while the Young Modulus describes the stiffness of the material. Often, the linear elastic law of equation Eq 2.6 is formulated as follows:

$$\sigma = \mathbf{E} * \varepsilon \tag{2.9}$$

where $\mathbf{E}$ is a rank for tensor which relates the coefficients of the stress tensor linearly to the coefficients of the strain tensor. Note that, the elastic energy $\mathbf{W}$ can be written simply as a function of the linearized strain and stress tensors:

$$\mathbf{W} = \frac{1}{2} tr(\varepsilon \cdot \sigma) \tag{2.10}$$

This linear relation is mathematically very convenient and allows to perform pre-computation, which leads to fast computation and very efficient algorithms which is a major requirement in surgical simulators. Thus, this model has been deployed for real-time simulation of elastic deformations in the context of surgery simulation Bro-nielsen and Cotin (1996); Cotin et al. (1999); Szekely et al. (2000), with correct visual rendering and haptic feedback. Its usability is however dependent on the type of surgery and the structure of the modelled organ, and limited to a certain range of deformations, to ensure the validity of the small displacement hypothesis (less than 10% of the size of the mesh).

Non-linear Elasticity Although the hypothesis of linearity can give a good approximation in the case of small deformations, it is often violated when dealing with large deformations under manipulation of surgical instruments. This may introduce significant errors and unrealistic distortions of the mesh. Figure 2.13 illustrates the limitations of using linear elastic models.

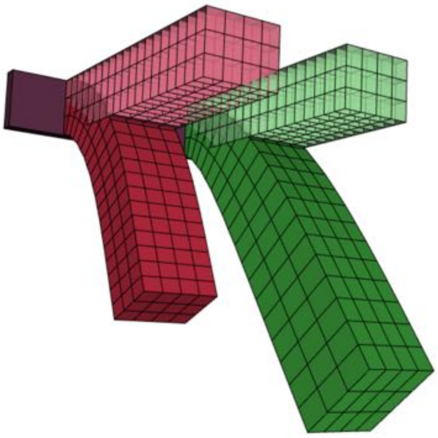

Figure 2.13: Comparison between non-linear (red) and linear (green) models with two beams with the same mechanical properties deformated under the effect of the gravity: The limitation of using linear elastic models reside in the simulation of large deformations when we notice a visually aberrant deformation.

Modeling such deformations involves the expression of stress with the current deformation, making the formalization and computation of such a relation much more complex. Overall, the energy **W** involved in the deformation of an hyper-elastic material (non-linear elasticity) is given by:

$$\sigma = \frac{\partial \mathbf{W}(\varepsilon)}{\partial \varepsilon} \tag{2.11}$$

We obtain here a general expression that relates stress to strain.

Several non-linear models have been proposed in surgical simulation trying to faithfully reproduce organs behaviour Picinbono et al. (2003); Miller et al. (2007); Comas et al. (2008); Marchesseau et al. (2010). The major issue resides in their ability to perform real-time achievement while ensuring accuracy and stability.

2.6.2 The Finite Element Method

At this stage, we describe a set of equations that govern the physical behaviour of an object. These equations must be integrated throughout the area, which results in an infinite number of equations. The Finite Element Method (FEM) is a popular method for finding approximate solutions of Partial Differential Equations (PDE's) on irregular grids or meshes. It is worth mentioning that alternatives to FEM exist such as finite differences method Terzopoulos et al. (1987), finite volume method Teran et al. (2003) or boundary element method James and Pai (1999).

Domain Discretization

The essential characteristic of this approach is the discretization of a continuous domain into a set of discrete sub-domains. In our case, the volume of the deformable object is generally discretized using a mesh composed of linear elements (triangles, tetrahedra, hexahedra, etc.) where shape functions are defined. This leads to continuous representations with varying levels of continuity (linear, quadratic, etc.).

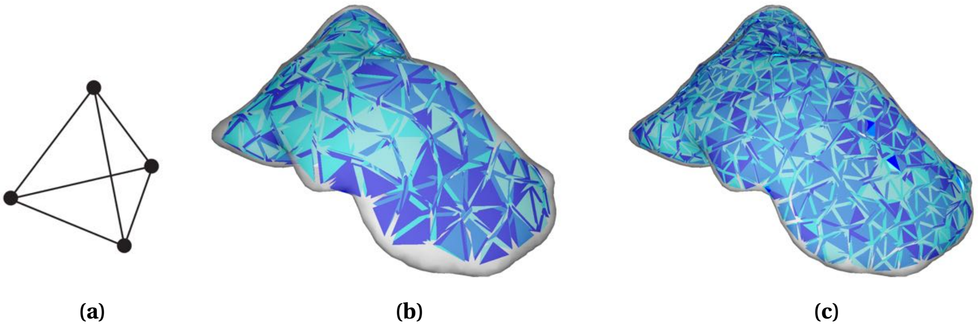

Figure 2.14: Domain discretization: (a) P1 linear tetrahedral element, (b) liver FEM model with 1563 elements (c) liver FEM model with 3205 elements

The choice of the type of elements that compose the mesh is very important, since it directly impacts the accuracy and the performance of the simulation. Triangles are usually used for 2D representation while tetrahedra and hexahedra are used for 3D. The elements are generated from surface meshes and must cover all the volume of the object without any overlapping. In addition, each element has an interpolation equation (or shape function) that defines the variation of the quantity within the element. Very often, this shape function is polynomial with an order chosen to be the lowest one possible.

The most popular elements used in the literature are P1 linear tetrahedral elements (see Figure 2.14). These elements are the simplest elements in 3D: each element has four nodes $n =\in \{1, \ldots 4\}$ and interpolation functions are linear. The simplest linear function in 3D is defined as:

$$\gamma(x_1, x_2, x_3) = a + bx_1 + cx_2 + dx_3 \tag{2.12}$$

Numerical solution

The partial differential equation to be solved and governing dynamic elastic materials is given by:

$$\rho\ddot{\mathbf{x}} = \nabla\sigma + \mathbf{f} \tag{2.13}$$

where ρ is mass density of the material and f are externally applied forces such as gravity. Divergence operator turns the 3 × 3 stress tensor back into a 3-vector:

$$\nabla \cdot \sigma = \begin{bmatrix} \sigma_{xx,x} + \sigma_{xy,y} + \sigma_{xz,z} \\ \sigma_{yx,x} + \sigma_{yy,y} + \sigma_{yz,z} \\ \sigma_{zx,x} + \sigma_{zy,y} + \sigma_{zz,z} \end{bmatrix} \tag{2.14}$$

representing the internal force resulting from a deformed infinitesimal volume. The FEM is used to turn a PDE into a set of algebraic equations which are then solved numerically. To this end, the domain M is discretized into a finite number of disjoint elements (i.e. a mesh). Instead of solving for the spatially continuous function $\mathbf{x}(\mathbf{m}, t)$, one only solves for the discrete set of unknown positions $\mathbf{x}_i(t)$ of the nodes of the mesh. First, the function $\mathbf{x}(\mathbf{m}, t)$ is approximated using the nodal values by:

$$\tilde{\mathbf{x}}(\mathbf{m}, t) = \sum_i \mathbf{x}_i(t)\mathbf{b}_i(\mathbf{m}) \tag{2.15}$$

where $\mathbf{b}_i()$ are fixed nodal basis functions also known as the Kronecker Delta property which value is 1 at node i and 0 at all other nodes. In the most general case of the Finite Element Method, basis functions do not have this property. In that case, the unknowns are general parameters which can not be interpreted as nodal values. Substituting $\tilde{\mathbf{x}}(\mathbf{m}, t)$ into Eq. 2.14 results in algebraic equations for $\mathbf{x}_i(t)$. In Galerkin approach finding the unknowns $\mathbf{x}_i(t)$ is viewed as an optimization process. When substituting $\mathbf{x}(\mathbf{m}, t)$ by the approximation $\tilde{\mathbf{x}}(\mathbf{m}, t)$ the infinitely dimensional search space of possible solutions is reduced to a finite dimensional subspace. In general, no function in that subspace can solve the original PDE. The approximation will generate a deviation or residue when substituted into the PDE. In Galerkin method, the approximation which minimizes the residue is sought, i.e. an approximation whose residue is perpendicular to the subspace of functions defined by (Eq. 2.15) is computed.

Very often, a simple form of the Finite Element method is used for interactive simulation of deformable objects. In this method, both masses and (internal and external) forces are lumped to the vertices. Nodes in the mesh are treated like mass points in a mass-spring system while each element acts like a generalized spring connecting all adjacent mass points. Forces acting on the nodes of an element due to its deformation are computed as follows (see for instance (O'Brien et al., 1999): given the positions of the vertices of an element and the fixed basis functions, the continuous deformation field $\mathbf{u}(\mathbf{m})$ inside the element can be computed using (Eq. 2.16). From $\mathbf{u}(\mathbf{m})$, the strain field $\varepsilon(\mathbf{m})$ and stress field $\sigma(\mathbf{m})$ are computed. The deformation energy of the element is then given by:

$$\mathbf{E} = \int_{v} \varepsilon(\mathbf{m}) \bullet \sigma(\mathbf{m}) d\mathbf{m} \tag{2.16}$$

where the dot ($\bullet$) represents the component-wise scalar product of the two tensors. The forces can then be computed as the derivatives of the energy with respect to the nodal positions. In general, the relationship between nodal forces and nodal positions is non-linear. However, linear PDE yields linear algebraic systems which can be solved more efficiently and more stably than non-linear ones. Thus, a vast majority of the work done in the area of real-time deformable models using FEM was based on linear elasticity equations.

2.6.3 Time Integration

The core mechanical equations based on Newton's second law is given by Equation 2.13 in a non-linear ordinary differential equation system that can be written:

$$\mathbf{Ma} = \mathbf{f}(\mathbf{x}, \mathbf{v}) \tag{2.17}$$

where $\mathbf{x}$, $\mathbf{v}$, and $\mathbf{f}$ are respectively the position, velocity and force vectors, $\mathbf{a}$ is the acceleration and $\mathbf{M}$ the mass matrix. $\mathbf{f}(\mathbf{x}, \mathbf{v})$ defines both internal forces of the physical model and the external forces applied on the object such as gravity, interaction contacts or friction.

This system of equations gives an expression of the forces applied to the simulated objects depending on the current state. We need now to numerically solve (i.e. integrate) this system of equations over time.

There exists a number of integration schemes Hauth et al. (2003). Most of the studies in computer graphics relate the forward euler (explicit) and backward euler (implicit) integration scheme.

Explicit scheme or forward Euler, is the simplest integration scheme where integrals are evaluated with the left-hand rectangle method. Its advantage is that it is easy to implement. However, it is stable only if the time step Δt is smaller than a stability threshold (This condition is known as the Courant-Friedrichs-Lewy (CFL) stability condition). This threshold can be very small for stiff objects, and if violated can lead simulation to explode.

Implicit scheme or backward Euler can counteract the stability issue of the explicit integration by adding quantities at the next time step using right-hand rectangle method. We describe here implicit schemes which were used in this thesis, since it provides stability with relatively large time steps.

Let's consider the time interval $[t, t+h]$ which length h is called time step. Integrating from t to $t+h$ which updates velocities and positions based on accelerations at the end of the time step can be described as:

$$\begin{cases} \mathbf{M}\cdot\mathbf{a}_{t+h} = \int_{t+h}^{t} \mathbf{f}(\mathbf{x}_t,\mathbf{v}_t)dt \\ \mathbf{v}_{t+h} = \mathbf{v}_t + \int_{t+h}^{t} \mathbf{a}dt \\ \mathbf{x}_{t+h} = \mathbf{x}_t + \int_{t+h}^{t} \mathbf{v}dt \end{cases} \tag{2.18}$$

The evaluation of integrals $\int_{t+h}^{t}\mathbf{f}(\mathbf{x}_t,\mathbf{v}_t)dt$, $\int_{t+h}^{t}\mathbf{a}dt$ and $\int_{t+h}^{t}\mathbf{v}dt$ using the backward euler scheme is as follows

$$\begin{cases} \mathbf{M}\cdot\mathbf{a}_{t+h} = \mathbf{f}(\mathbf{x}_{t+h},\mathbf{v}_{t+h}) \\ \mathbf{v}_{t+h} = \mathbf{v}_t + h\mathbf{a}_{t+h} \\ \mathbf{x}_{t+h} = \mathbf{x}_t + h\mathbf{v}_{t+h} \end{cases} \tag{2.19}$$

The resolution of this system implies the resolution of a non-linear system, since $\mathbf{f}(\mathbf{x}_{t+h},\mathbf{v}_{t+h})$ depends on $\mathbf{x}_{t+h}$ and $\mathbf{v}_{t+h}$ which are not known at the end of the time step. Thus, to solve this system non-linear function $\mathbf{f}(\mathbf{x}_{t+h},\mathbf{v}_{t+h})$ is approximated by a first order approximation of a Taylor series expansion:

$$\mathbf{f}(\mathbf{x}_{t+h},\mathbf{v}_{t+h}) \approx \mathbf{f}(\mathbf{x}_t,\mathbf{v}_t) + \mathbf{K}\cdot(\mathbf{x}_{t+h}-\mathbf{x}_t) + \mathbf{B}\cdot(\mathbf{v}_{t+h}-\mathbf{v}_t) \tag{2.20}$$

where **K** is the stiffness matrix and **B** the damping matrix. When combining equations 2.20 and 2.19 and let $\mathbf{dv} = h\mathbf{a}_{t+h} = \mathbf{v}_{t+h} - \mathbf{v}_t$, we obtain the final linearized system

$$\underbrace{(\mathbf{M} - h\mathbf{B} - h^2\mathbf{K})}_{\mathbf{A}}\cdot\underbrace{\mathbf{dv}}_{x} = \underbrace{h\mathbf{f}(\mathbf{x}_t,\mathbf{v}_t) + h^2\mathbf{K}\cdot\mathbf{v}_t}_{\mathbf{b}} \tag{2.21}$$

This equation is a linear system where **A** and **b** are known and x is the unknown. Solving this type of systems was largely studied with a high number of methods which aim to solve the system in an efficient fashion. A popular method to efficiently solve this problem is the Conjugate Gradient (CG) iterative solver Baraff (1998); Saad (2003). This iterative method can be tuned to achieve accuracy as well as speed by controlling the number of iterations and residual error threshold or by using pre-conditioning techniques Courtecuisse et al. (2014). The CG iterative solver, however suffers from convergence issues for ill-conditioned matrices, which can appear for inhomogeneous materials or meshes with varying element sizes. Thus, some studies report the use of direct solver (such as LDL or LU Trefethen and Bau (1997)) when dealing with non-homogeneous tissue Peterlík et al. (2012).

2.6.4 Achieving Real-time Simulation

As mentioned previously, the computation time of the previous algorithms is a major aspect to consider when dealing with medical applications. In order to reach real-time, several stages of the algorithm can be optimized. Some approaches focus on a specific formulation of the constitutive law of the deformable object Comas et al. (2008); Müller and Gross (2004), others rely on the optimization of the solver necessary to solve the linear system of equations resulting from FEM formulation Barbič and James (2005); Bro-nielsen and Cotin (1996); Allard et al. (2011), while a few approaches choose the adequate time integration scheme Miller et al. (2007); Hauth et al. (2003).

Physics-based modeling of liver tissue represents an important part of this thesis. Since our goal is to provide a coherent augmented reality method for surgery guidance, elastic behaviour of the liver is a key aspect to be considered. We aim to bring simulation of soft-tissue in the operating rooms as in the last decades, medical simulation was mainly used for surgery training and plaining. Nevertheless, it is important to point out that this work uses well-established methods, that have been previously developed. Our contributions in this field consists of the appropriate definition of external forces which emanate from the images and on the validation, through experiments, of the usability of real-time simulation in an intra-operatively context.

2.7 Conclusion

We have presented in this chapter the medical context that motivates this work. We have described minimally invasive surgery with its benefits and limitations that pushed the emergence of new techniques in computer assisted surgery. One of these techniques resides in the use of Augmented Reality in operating rooms which still has several problems to be solved. Among all the current limitations of surgical Augmented Reality, we focused on the correct modeling of soft-tissue which is, in most of the literature, considered as rigid or negligible. We have presented the current techniques for 3D reconstruction and tracking of human organs which represent the first stage towards medical augmented reality and gave an overview of the main numerical techniques for computing deformation of elastic bodies in real-time.

In the following chapter, we present an approach for recovering 3D shape of the liver under large elasticity, using a non-linear mechanical model and image data acquired from a monocular camera only. Tests on minimally invasive images are conducted and comparison with related techniques is provided where we show that non physical approaches lack to correctly capture image deformations.

CHAPTER 3

3D RECONSTRUCTION OF ELASTIC OBJECTS FROM A SINGLE VIEW

Contents

3.1 Introduction

As stated in the previous chapter, our aim is to estimate three-dimensional motion of the liver during MIS from an endoscopic camera. In this context, several techniques exist, using various types of optics and sensors (structured light, stereoscopy, time-of-flight, photometry ...). Nevertheless, most of the time, minimally invasive surgery relies on the use of a monocular endoscope without any additional hardware modification. Thereby, we investigate here the 3D recovery and augmentation of liver surface from a single view.

3D recovery and augmentation of deformable objects in a monocular context is a challenging problem with many potential applications in computer graphics, augmented reality and medical imaging. The difficulties originate from the fact that several 3D shape configurations lead to the same 2D projection on the image, which leads to obtain various ambiguities and make the problem under-constrained. To overcome this problem, various approaches have been considered with the aim to provide additional contraints and solve the ambiguities. Many approaches introduced deformation models, which are often learned from training data and derive models with few degrees of freedom. A lot of papers have been devoted to inelastic materials such as papers, sails, clothes ... and make use of inextensibilty constraint, ensuring that the distance between points remains constant. Other geometric or shading constraints have been proposed to handle materials that can stretch. However, the additional constraints that are used are not always suited to the properties of the object.

In this chapter, we propose an efficient real-time algorithm for recovery and augmentation of highly elastic objects in a monocular context. Using a rough estimation of the stiffness of the targeted object and the adequate boundary constraints, our method outperforms state-of-the-art approaches. We present experiments in a general context where various elastic objects are used since a ground truth can easily be computed, and in the context of augmented reality for minimally invasive liver surgery with surgical data.

3.2 Prior Works on Non-rigid Shape Recovery

In the early works on augmented reality for deformable objects, registration of images of a deforming surface was obtained by computing dense 2D/2D transformations using points correspondences. A parametric representation of deformation or regularization techniques were needed to prevent excessive wrinkling of the surface in the presence of erroneous correspondences. In Bartoli and Zisserman (2004b), they take advantage of a rich texture information to perform points matching between images, allowing a 2D deformation motion model to be computed using Radial Basis Mapping. Pilet et al. (2008) proposed

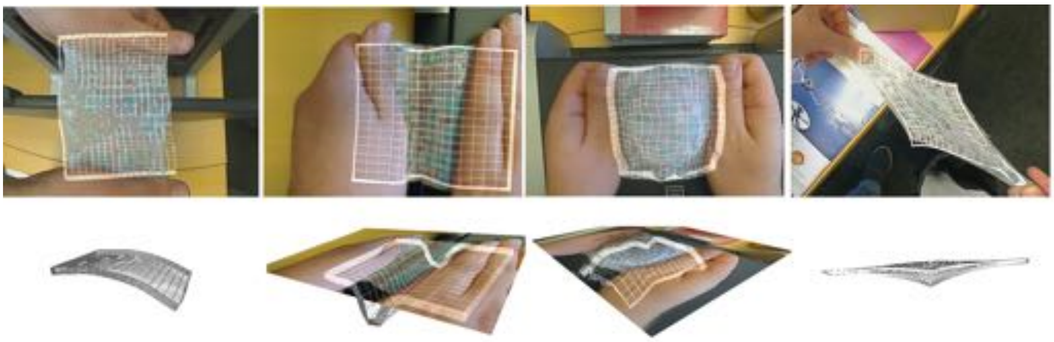

Figure 3.1: Three-dimensional reconstruction and augmentation of elastic objects from a single view under several elongations. Our approach is able to handle extensibility of the material when undergoing elongation. (top) Camera view of the re-textured elastic object and (bottom) the recovered 3D shape showed in a different view.

a template-based fast and robust tracking for handling deformations. This approach uses a set of wide baseline feature matches assuming a well textured surface and combines 2D deformable meshes with a robust estimation technique. Zhu and Lyu (2007) demonstrated that a Finite Newton algorithm and an efficient factorization method can reduce the number of iterations of the previous method to solve the optimization problem. In order to handle the more challenging case of deformation with self occlusions, Gay-Bellile et al. (2010) considered the occluded pixels as self-occlusion area that forces the wrap to shrink instead of outliers. Inspired by this self-occlusion shrinking method, Hilsmann et al. (2010) proposed an approach exploiting an optical flow extended by a specific illumination model which jointly estimates deformation and illumination and can cope with self-occlusions through an occlusion map computed from local statistical color models. In Pizarro and Bartoli (2012), self occlusions are detected as outliers based on the assumption that the surface to detect is locally smooth.

However, these methods based on 2D image transformations are well suited to smooth deformations but are not suitable for highly elastic objects. In fact, elastic deformations in 3D space can lead to highly complex 2D deformations in the image plane, especially due to self occlusions, making inappropriate the use of regularization contraints. For these reasons, state-of-the art methods perform 3D reconstruction of deformable surfaces using template-based techniques. Recovering the 3D shape of a deformable surface from a monocular video and a template (a *reference* image of the surface for which the 3D shape is known) can be ambiguous. Therefore, additional consistency constraints are required to solve ambiguities. The inextensibility constraint is widely used to recover and augment objets as sheets of paper, sails, tee-shirts... Shen et al. (2010); Perriollat et al. (2011). Methods differ in the way that inextensibility is considered as a hard constraint or a penalty term and also in the efficiency of convex or non-convex optimization associated to the procedure. In the general case, global smoothness constraints are common to resolve the ambiguities of 3D reconstruction. Many papers ressort to a linear description of feasable object deformation. Most of the time, it is generated from a representative sample of possible shapes using a dimensionality reduction process Salzmann et al. (2007b); Salzmann and Fua (2011).

Some works attempt to overcome the need to provide plausible constraints on the deformation by using richer sources of information. In Moreno-Noguer et al. (2009) a closed-form solution constrained by shading information was introduced to capture stretching surface. This method assumes a Lambertian surface with a single point light source and yield good results. However, strong assumptions on lighting make the method hard to generalize in all environments. Other methods have been designed to cope with non smooth deformations, as folding. Salzmann et al. (2007a) proposed to solve the problem as a convex minimization of the reprojection error formulated as a Second Order Cone Programming (SOCP). The method restricts the motion from one frame to the next but does not impose unwarranted surface smoothness, making it possible to recover sharp folds.

Recently, many examples of mechanical-based tracking methods have emerged. For instance the approach in Agudo et al. (2012), where a combination of Finite Element Modelling with an Extended Kalman Filter showed the efficiency of physics-based methods. In Wuhrer et al. (2012), a linear finite element method is used to predict the deformation. The approach described in Malti et al. (2013) relies on the minimization of a stretching energy subject to external image constraints. The problem is formalized as a non-linear minimization that unifies geometric constraints assuming a projective camera and mechanical constraints and local linear elasticity. This method showed effective results by considering the Poisson ratio as the unique mechanical parameter but the framework is not built to handle high elastic deformations.

3.3 Non Linear Elastic model

The choice of a relevant constitutive model is essential as it will determine the set of deformations we are able to capture and estimate while discriminating non-plausible material configurations induced by the errors of tracking. Two important assumptions are also made in order to reduce the complexity of the deformation model and the number of related parameters. First, the material of the deformable object will be *homogeneous* meaning that a uniform deformation will lead to equal (in magnitude) forces for any points of the object. Second, the material will also be considered as *isotropic* meaning that the response to a deformation is independent of the orientation of the deformation. Moreover, the computation time is also a key constraint as the targeted application should be *interactive*. Interactive (or at least computationally fast) models for deformable solids have been a major topic in the computer graphics community. Several reports or surveys have been published to provide an exhaustive overview of state-of-the-art methods Gibson and Mirtich (1997); Nealen et al. (2006); Sifakis and Barbic (2012). In that context, Saint Venant-Kirchhoff model Sifakis and Barbic (2012) appears to be an ideal compromise because it is able to handle non-linear deformations, is rotationally invariant and is simple enough compared to other non-linear models and therefore can be computed at interactive rates. Several downsides however exist such as incorrect stress estimation under extreme compression and sometimes the requirement to use non-linear solvers to compute the motion over time. Incorrect stress estimation under any large deformation is not a major issue in our case since we are interested in capturing an accurate deformation field and since the stress field is not measurable with camera images. Recent works on simulation or on haptics rendering have proposed computationally fast non-linear solvers such as Silcowitz-Hansen et al. (2010) which leverages the pre-requisites of the use non-linear solvers with Saint Venant-Kirchhoff model.

A Saint Venant-Kirchhoff (StVK) material is a material for which the Green-Lagrange strain tensor $\mathbf{E} \in \mathbb{R}^{3x3}$ is computed as a non-linear (quadratic) function of the deformation gradient $\mathbf{F} \in \mathbb{R}^{3x3}$ as:

$$\mathbf{E} = \frac{1}{2}(\mathbf{F}^T\mathbf{F} - \mathbf{I}) \tag{3.1}$$

where $\mathbf{I} \in \mathbb{R}^{3x3}$ is the identited matrix. The computation of the strain tensor maybe computationnally intensive and several approaches have been investigated for interactive uses. For instance, Barbic and James Barbič and James (2005) used model reduction and pre-computation reduced coordinates while Zhong *et. al.* Zhong et al. (2005) used pre-computed relation between surface and internal nodes. In the following, the elegant approach of Kikuuwe *et. al.* Kikuuwe et al. (2009) is chosen since it does not require pre-computation nor does it make any assumption on the deformations that will be generated. To do that, fast computation is conducted using dedicated simple data-structures (tetrahedron-sharing edge-pairs). We will detail the main points of Kikuuwe *et. al.*.

If v is a point in the deforming medium and v_0 is its initial location, $\mathbf{F}$ can be expressed as $\mathbf{F} = \frac{\partial v}{\partial v_0}$ Since $\mathbf{E}$ is symmetric, its form is as follows:

$$\mathbf{E} = \begin{bmatrix} \epsilon_{xx} & \epsilon_{xy} & \epsilon_{zx} \\ \epsilon_{xy} & \epsilon_{yy} & \epsilon_{yz} \\ \epsilon_{zx} & \epsilon_{yz} & \epsilon_{zz} \end{bmatrix} \tag{3.2}$$

and the 6 independent coefficients may be placed in a single vector ϵ using Voigt notation:

$$\epsilon = [\epsilon_{xx}, \epsilon_{yy}, \epsilon_{zz}, 2\epsilon_{xz}, 2\epsilon_{yz}, 2\epsilon_{zx}]^T \tag{3.3}$$

Computing $\mathbf{E}$ is often conducted by using a strain energy density w that will be integrated over the whole deforming medium X through the following equation:

$$\mathbf{E} = \int_X w \, dX \tag{3.4}$$

An isotropic homogeneous Saint Venant-Kirchhoff material has w expressed as follows:

$$w = \epsilon^T \mathbf{D} \epsilon / 2 \tag{3.5}$$

where $\mathbf{D} \in \mathbb{R}^{6x6}$ is the following matrix:

$$\mathbf{D} = \begin{bmatrix} \lambda + 2\mu & \lambda & \lambda & 0 & 0 & 0 \\ \lambda & \lambda + 2\mu & \lambda & 0 & 0 & 0 \\ \lambda & \lambda & \lambda + 2\mu & 0 & 0 & 0 \\ 0 & 0 & 0 & \mu & 0 & 0 \\ 0 & 0 & 0 & 0 & \mu & 0 \\ 0 & 0 & 0 & 0 & 0 & \mu \end{bmatrix} \tag{3.6}$$

where λ and μ are *Lamé* coefficients and can be computed thanks to the elastic parameters of the material E and ν. E is the Young's modulus and is a measure of the stiffness of the material while ν is the Poisson's ratio and estimates the compressibility of the material.

For a deforming medium of arbitrary shape, it is often convenient to discretize the shape using elementary and simple elements. Tetrahedral decomposition is often considered since efficient meshing algorithms exist. For a tetrahedron t, let us consider the edge e among the 6 possible edges of t, e being connected two vertices v_i and v_j. Be $l_e = v_i - v_j$ and $l_e^0 = v_i^0 - v_j^0$. Assuming that the deformation gradient **F** is constant in the neighborhood of t and has the value $\mathbf{F}_t$, l_e can be estimated as $\mathbf{F}_t l_e^0$. The equation (3.1) can be used to write:

$$\begin{aligned} l_e^T \mathbf{E}_t l_e &= \tfrac{1}{2} l_e^T (\mathbf{F}_t^T \mathbf{F}_t - I) l_e \\ l_e^T \mathbf{E}_t l_e &= \tfrac{1}{2} (\| l_e \|^2 - \| l_e^0 \|^2) \end{aligned} \tag{3.7}$$

l_e^0 can also be written in Voigt notation using the variable q_e^0 defined as:

$$q_e^0 = \begin{bmatrix} (v_i.x - v_j.x)^2 \\ (v_i.y - v_j.y)^2 \\ (v_i.z - v_j.z)^2 \\ (v_i.x - v_j.x)(v_i.y - v_j.y) \\ (v_i.y - v_j.y)(v_i.z - v_j.z) \\ (v_i.z - v_j.z)(v_i.x - p_j.x) \end{bmatrix} \tag{3.8}$$

where for each value $.x$, $.y$, $.z$ is the first / second / third component of the considered vector. The previous equation is rewritten by using Voigt notations as:

$$q_e^{0T} \epsilon_t = \frac{1}{2} (\| l_e \|^2 - \| l_e^0 \|^2) \tag{3.9}$$

This equation is considered for a single edge e but is suitable for the other edges. By considering the 6 edges of the tetrahedron t, we obtain the following equation:

$$\mathbb{Q}_t \epsilon_t = \frac{1}{2} \mathbb{L}_t \tag{3.10}$$

where $\mathbb{Q}_t = [q_0^0, q_1^0, q_2^0, q_3^0, q_4^0, q_5^0]^T$ (q_e for the 6 possible edges) and $\mathbb{L}_t = [\| l_0 \|^2 - \| l_0^0 \|^2, \| l_1 \|^2 - \| l_1^0 \|^2, \ldots]^T$ (again for the 6 possible edges). It should be noted that $\mathbb{Q}_t \in \mathbb{R}^{6x6}$ and $\mathbb{L}_t \in \mathbb{R}^6$. $\mathbb{Q}_t$ is invertible if the 4 points are not linearly dependent and therefore ϵ_t can be estimated as:

$$\epsilon_t = \frac{1}{2} \mathbb{Q}_t^{-1} \mathbb{L}_t \tag{3.11}$$

enabling to compute the strain energy in the tetrahedron t with

$$W_t = \epsilon_t^T \, \mathbf{D} \, \epsilon_t / 2 \tag{3.12}$$

Therefore, the total strain energy $W = \sum W_t$ of the medium as a function of the edge lengths of the tetrahedral mesh and elastic parameters. Eventually, the forces exerted on the vertices can be computed as:

$$f(v) = \frac{\partial W}{\partial v^T} \tag{3.13}$$

For computation purposes, a global stiffness matrix is also computed as:

$$K(v) = \frac{\partial f(v)}{\partial v} \tag{3.14}$$

as it allows for a displacement dv (such as $v' = v + dv$) of the mesh vertices to compute the resulting forces as:

$$f(v) = K(v) \times dv \tag{3.15}$$

This is a convenient equation that relates forces to any displacement of the vertices but again it should be reminded that the matrix $K(v)$ should be recomputed after every deformation to remain valid.

3.4 Problem Formulation

When dealing with elastic surface, additional penalty functions are used to obtain a well-constrained system. These constraints are often based on the inextensibility property of the surface to be recovered. Since such constraints cannot be considered in our case, we propose to consider the elastic registration as a stretching energy minimization problem that accounts for the internal forces of the mechanical and external forces emanated from the visual tracking.

3.4.1 Required assumptions

In order to ensure a good shape recovery and a well-posed system, we assume that the following data are available:

- The projective matrix P assuming fixed camera under a full projective model.
- The correct initial alignment of the mesh (in rest configuration) on the image.
- A set T of paired points between the set of features $U = \{u_i \in \mathbb{R}^2\}$ from visual tracking and the mesh vertices $V = \{v_i \in \mathbb{R}^3\}$ related to the mechanical model.
- The material stiffness that represents the elasticity of the mechanical model.

3.4.2 Initialization

At initialization, each feature u_i is associated with a 3D point U_i by intersection of the line of sight with the surface. U_i is expressed as a barycentric combination of facet vertices, following:

$$U_i = a_i v_1 + b_i v_2 + c_i v_3 \tag{3.16}$$

where $v_{i;1\leq i\leq 3}$ are the vectors of 3D vertex coordinates and (a_i, b_i, c_i) the barycentric coordinates of U_i. We assume that this linear relation remains valid during the deformation.

3.4.3 Image Fitting

We propose to consider the features displacement as a stretching energy defined as

$$E_s = \sum_{i\in T} \frac{1}{2} k \| u_i - P(U_i) \|^2 \tag{3.17}$$

where k can be seen as a stiffness and is experimentally chosen to be the same order of magnitude of the Young's modulus.

3.4.4 Boundary Conditions

In order to obtain a system that is sufficiently constrained to give good results, we add to the system a set B of boundary constraints by using the hard constraint:

$$v_i = Q_i \; for \; i \in B \tag{3.18}$$

where Q_i are the known boundary conditions that can be seen as a set of fixed vertices. The boundary conditions are necessary to yield good results. These boundary conditions are most of the time quite natural and specify how the object is linked to its environment such as an object fixed to a table or contained by an obstacle (illustrated in Figure 3.7).

3.4.5 Energy Minimization

The minimization problem is then formulated as a constrained minimization between internal elastic energy and stretching energy and can be written as follows:

$$\begin{array}{rl} minE(v) & = \sum_t W_t + \sum_{i\in T} \frac{1}{2} k \| u_i - P(U_i) \|^2 \\ subject\; to & v_i = Q_i \; for \; i \in B \end{array} \tag{3.19}$$

where W_t is the strain energy of a tetraherdon related to a Saint Venant-Kirchhoff material and which depends on the position of the vertices. The expression of W_t is detailed in equation (3.12).

3.4.6 Resolution

Equation (3.19) is a classical constrained minimization problem. We choose to solve this equation by formulating a linear complementary problem (LCP) that will be solved with a Gauss-Seidel algorithm using the approach reported in Guébert et al. (2008). Finding the minimum of energy is conducted by deriving and setting to zero equation (3.19). This leads to an equality between internal elastic forces and stretching forces and this is equivalent to finding the equilibrium state of the material due to external forces. Indeed kinetic energy is not considered since we are not interested in capturing transient motions because first, the materials used are very soft and second, the acquisition rate is high enough; therefore the deformation exhibits no significant transient motion. Even if our approach is static (without dynamic due to kinetic energy of the material), it can easily be adapted to dynamic motion with the same method by adding a non-linear differential equation solver such as an implicit Euler with a conjugate gradient. In other words, this amounts to solve the linear system $\mathbf{A} \cdot \mathbf{x} = \mathbf{b}$ given by integrating in time the equation of dynamic $\mathbf{Ma} = \mathbf{f}$, where $\mathbf{f}$ includes the external forces f_s derived form the stretching energy E_s. Since the model used here is homogeneous, once can rely on a conjugate gradient iterative solver where pre-conditioning is possible to solve the linear system Courtecuisse et al. (2012).

3.5 Experimental Results

In this section we present the results obtained using our method and the comparison conducted with existing techniques. We report results obtained on three types of data: Silicone-made data, computer-generated data and liver data during *in-vivo* surgical procedure. To test the ability of our approach to capture 3D elastic deformations, we capture several video sequences of a silicone-like object undergoing different types of stretching deformation. We quantify three-dimensional shape recovery error with respect to a ground truth while visual assessment is reported on surgical data.

3.5.1 Computer-generated Data

We used the framework Sofa Faure et al. (2012) to generate elastic deformations of a silicone-like object with a Young's Modulus of $E = 0.15$ MPa. A force F is applied on the object to produce a 3D deformation (cf Figure 3.2). A video sequence of the deformations is captured with a virtual camera. Figure 3.2 illustrates the results obtained by calculating the distance between the tracked and simulated mesh where we report an average error of 0.83 % for simulation 1 and 0.70 % for simulation 2.

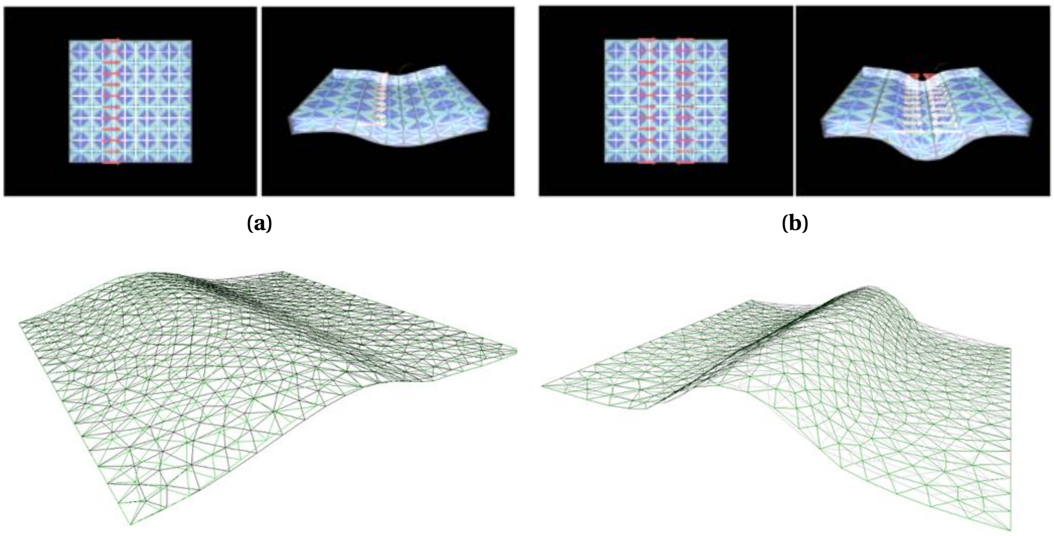

(a) **(b)**

(c) **(d)**

Figure 3.2: 3D registration error on two computer-generated sequences. The applied forces are represented with red arrows and the tetrahedral elements in blue (inverted top/down for a better visualization of forces). (a) simulation 1 where a single force is applied and (b) simulation 2 where two forces in opposite directions are applied. (c) and (d) show the superimposition of the recovered shape (in green) and the ground truth (black) for the first and second shape respectively.

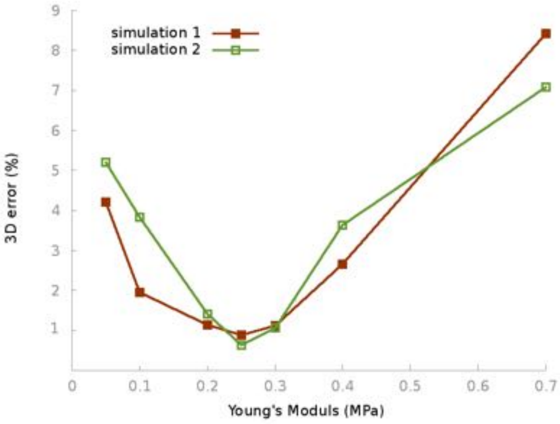

Figure 3.3: 3D registration error with variation of the Young's Modulus for simulation 1 and simulation 2: Small variation of the Young's Modulus value slightly affects the reconstruction while distant values highly increase the error.

Parameters Sensitivity

We also conduct experiments on the same set of data where we vary Young's Modulus value. The plot 3.3 shows that small variation of the Young's Modulus slightly affects the registration error in comparison with the large errors that produced greater or lower values. In the mean time, we notice that a value of k close to the Young's Modulus (at least at the same order of magnitude) gives the best results in terms of accuracy.

Impact of Boundary Conditions

We take advantage of synthetic data to assess the necessary use of boundary conditions to reach an acceptable shape recovery. We plot in the graphic of Figure 3.4 the 3D reconstruction error when varying the number of boundary points from 12 to 48 points. The results show that boundary conditions are necessary to yield good shape recovery and to resolve ambiguities.

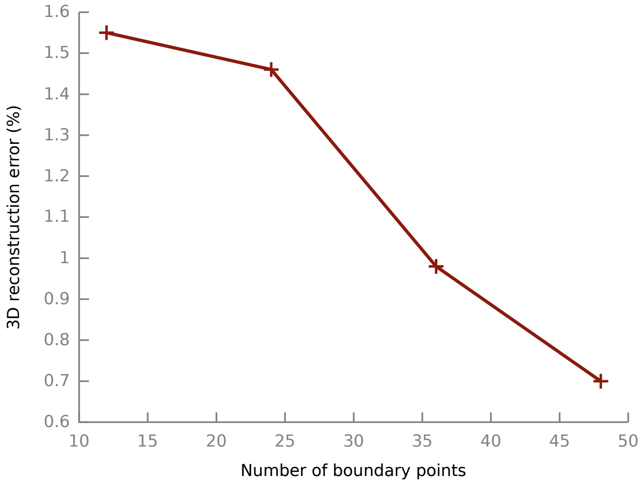

Figure 3.4: Impact of the boundary conditions on the 3D reconstruction.

3.5.2 Real Data

We tested our method on a silicone-like object of a size of $100 \times 100 \times 10$ mm^3 composed of linear P1 tetrahedral elements characterized by a Young's Modulus $E = 0.25$ MPa. Images were acquired using a monocular camera at 30 fps with an image resolution of 640×480. The implementation was done in C++ on a PC with an Intel i7 M620 2.76GHz processor.

2D Surface Registration and Retexturing

The aim of conducting tests on 2D surface is to be able to measure the registration error w.r.t the deformation of the object. Since the object boundaries can be easily extracted from images, a way to quantify this error is to compute the distance between the silhouette computed from the recovered 3D object and the actual boundaries extracted from images. The results reported in the plot 3.5 give the small 2D error even when the elongation increases (more than 120%).

The relation between the accuracy of the augmentation and the number of tetrahedron elements is also reported in figure 3.5 where we can notice that a finer mesh resolution reduces the registration error.

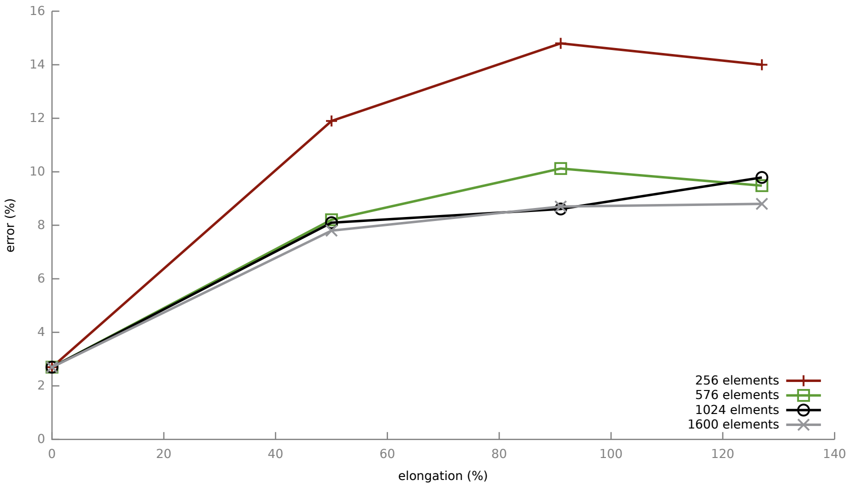

Figure 3.5: Registration error with respect to object elongation with a variation of mesh resolution: With an adequate number of tetrahedral elements, the projection error can be significantly reduced.

In order to ensure real-time achievement, a compromise has to be found between the number of elements and the computation time. While a large number of elements permits to obtain an accurate registration, it also increases the computation time. Table 3.1 shows the average errors and computation time w.r.t mesh resolution.

Number of elements	256	**576**	1024	1600
Average 2D Error (%)	10.84	**7.62**	7.3	6.92
Computation time (fps)	29	**17**	9	5

Table 3.1: Impact of the number of elements on the computation time and the registration error, where a large number of elements gives the lowest errors, it also increases the computation time.

3D Shape Recovery and Augmentation

For the three-dimensional reconstruction we propose to test our approach on 4 types of deformation, with extensibility up to 130% as illustrated in Figure 3.7. We calculate the Euclidean distance between the reconstructed surface and a ground truth. We compare our method with 3 existing approaches: an inextensible method for isometric and conformal surface reconstruction described in Bartoli et al. (2012) of which the code is freely available, a classical mass-spring system and a mechanical-based approach that considers a linear Strain/Stress formulation Cotin et al. (1999). The plots and the resulting shapes are illustrated in Figure 3.11.

Figure 3.6: Selected frames during a 2D elastic surface augmentation of the silicone-like material when being stretched up to 120%, with (top) input images (middle) registered mesh (bottom) surface retexturing.

Ground-truth acquisition The ground truth is obtained using a Structure from Motion technique Snavely et al. (2006). At the end of each manipulation, we reconstruct the 3D scene of all the environment where we place fiducials around the silicone object. These fiducials are necessary to align the 3D mesh on the input image (last frame of the sequence) in order to scale the mesh and apply the necessary rotation and translation. After the alignment is done, we keep only the 3D mesh of the silicone object. Some errors may occur from these transformations, but it is worth mentioning that the same ground truth is used for the comparison.

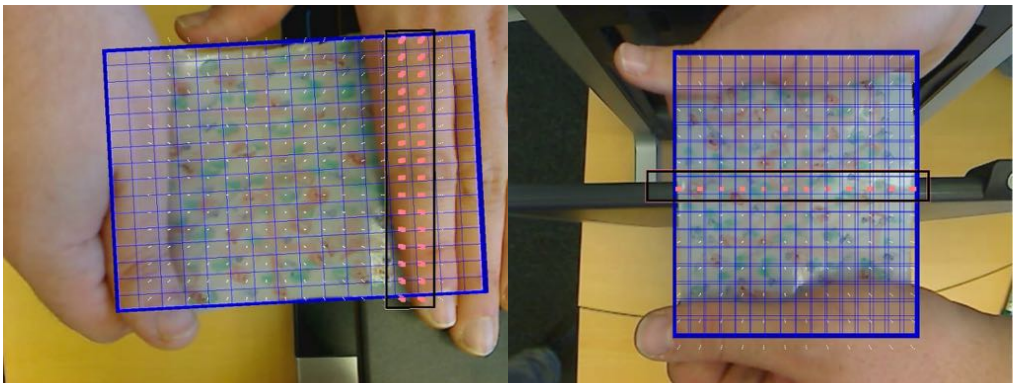

(a) Deformation 1 **(b)** Deformation 2

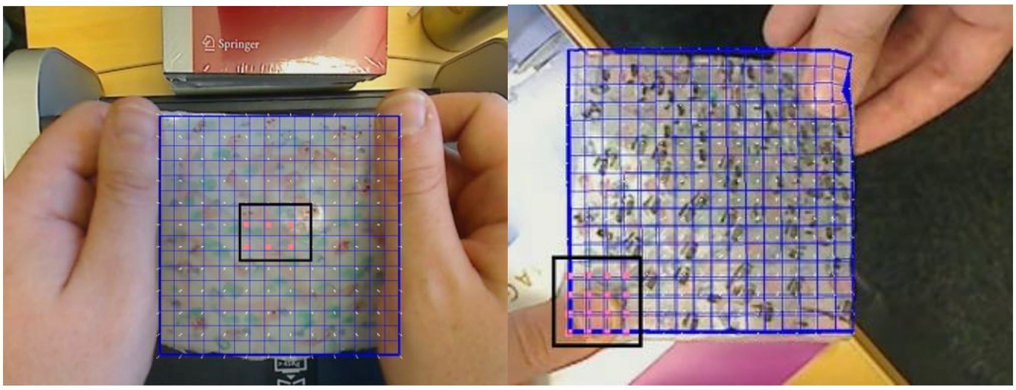

(c) Deformation 3 **(d)** Deformation 4

Figure 3.7: Silicone Dataset. The mesh is represented in blue and the boundary conditions in red surrounded by a black square.

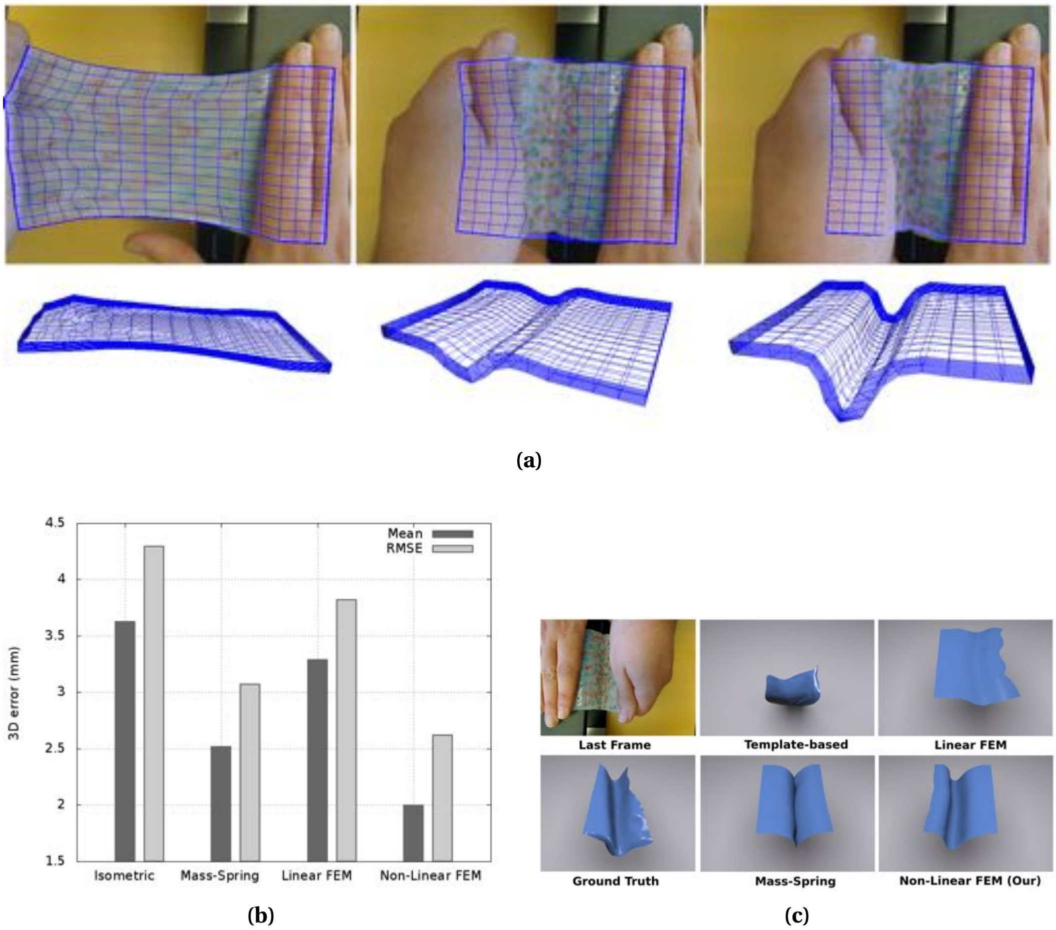

(a)

(b)

(c)

Figure 3.8: 3D shape recovery of a silicone-like material deformation: Our method produces the lowest error in comparison with other methods. (a) the sequence of deformation 1 with the recovered mesh superimposed on the image (b) comparison with current techniques (c) ground truth and shape recovery for each technique

Deformation 1: By stretching the object with an elongation of 30%, we force the surface to fold. The template-based and linear FEM approaches fail to recover the 3D shape. A non-linear method gives the lowest error with 2.62 mm. A template-based method needs more features than other techniques with respectively 168 features and 26 features.

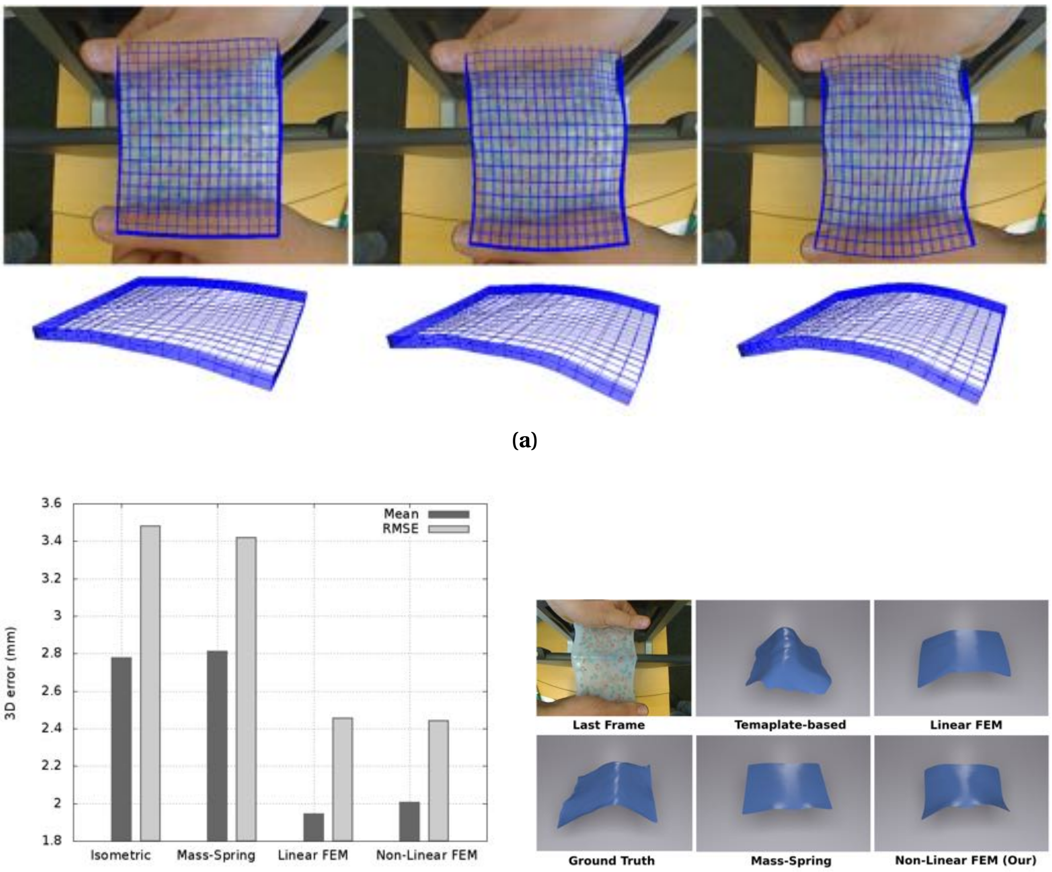

(a)

(b)

(c)

Figure 3.9: 3D shape recovery of a silicone-like material deformation: Our method produces the lowest error in comparison with other methods. (a) the sequence of deformation 2 with the recovered mesh superimposed on the image (b) comparison with current techniques (c) ground truth and shape recovery for each technique

Deformation 2: The surface is constrained with a rigid beam and stretched to produce a triangle-like shape. Only the mass-spring models was not able to recover the deformation. The template-based approach yields good results. However, mechanical methods report the most accurate registration with very close error: 2.52 mm for the Linear FEM and 2.44 mm for our method. The number of features extracted is 28 for all the methods except the template-based method, where 237 features are necessary to yield good results.

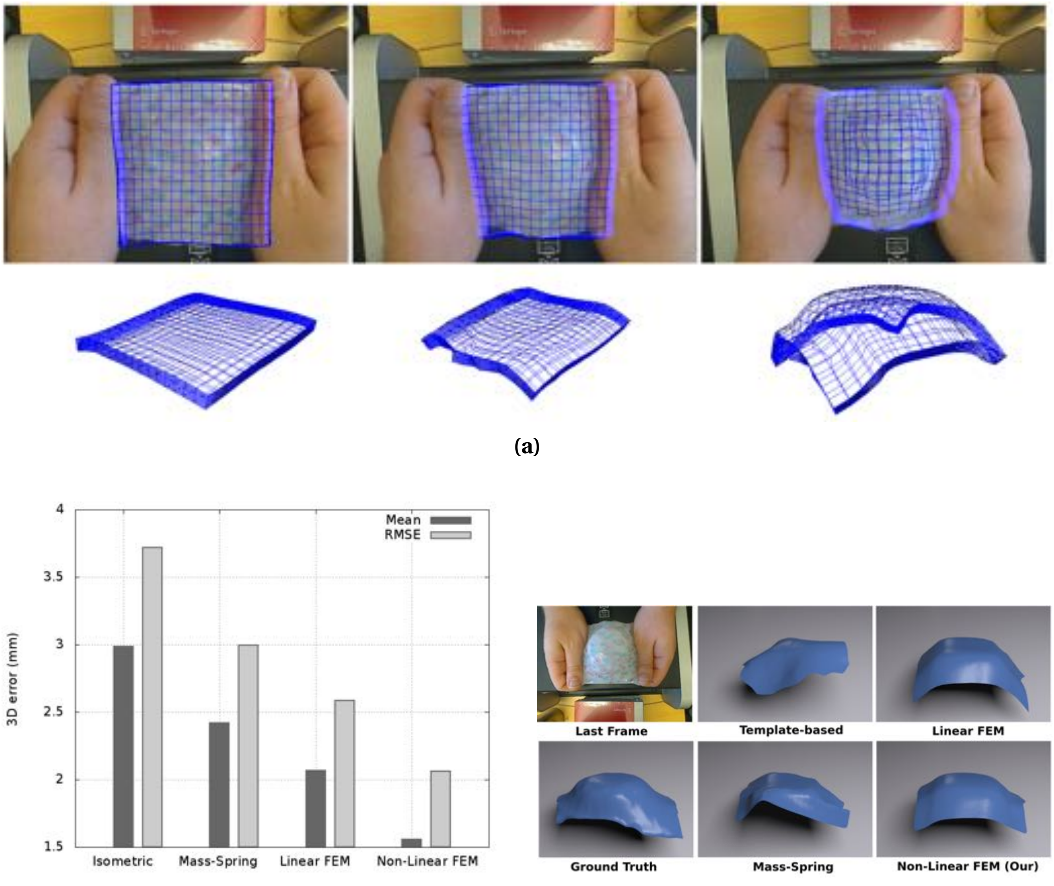

(a)

(b)

(c)

Figure 3.10: 3D shape recovery of a silicone-like material deformation: Our method produces the lowest error in comparison with other methods. (a) the sequence of deformation 3 with the recovered mesh superimposed on the image (b) comparison with current techniques (c) ground truth and shape recovery for each technique

Deformation 3: The object is elongated down and constrained at the center of the object. The four methods succeed to recover the shape deformation with 174 extracted features. Our method outperforms the others with an error of 2.06 mm.

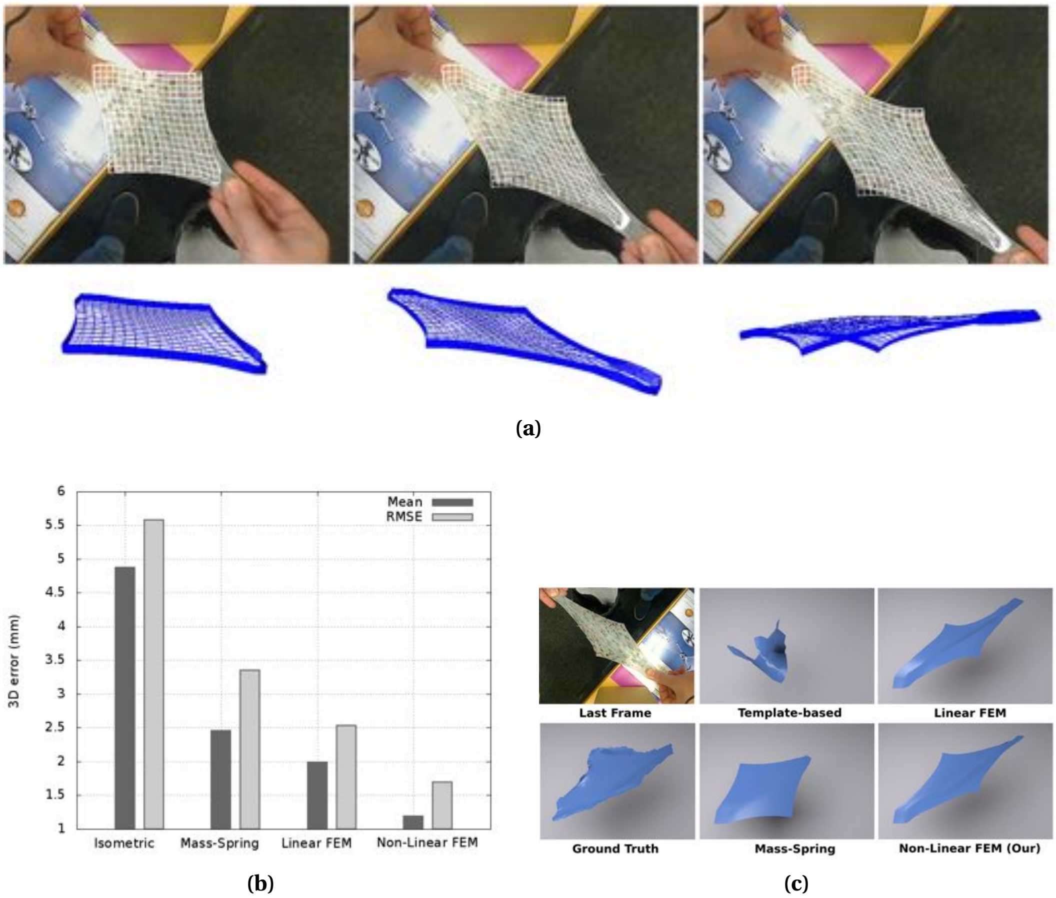

(a)

(b)

(c)

Figure 3.11: 3D shape recovery of a silicone-like material deformation: Our method produces the lowest error in comparison with other methods. (a) the sequence of deformation 4 with the recovered mesh superimposed on the image (b) comparison with current techniques (c) ground truth and shape recovery for each technique

Deformation 4: Our approach gives a small error of 1.69 mm where the extensibility is about 120%. The object highly elongated during the deformation and produced a 3D shape by partially folding. The template-based method fails to recover the stretched shape while the mass-spring and linear FEM models give relatively good shape representations.

3.6 Geometric Constraints Correction

Solving equation (3.19) yields to recover the 3D shape that satisfies the physical constraint of the object. However, in order to obtain the correct 3D reconstruction, both physical and geometrical constraints have to be satisfied. The geometrical constraint can be formulated as a minimization of the reprojection error given by:

$$m = \begin{pmatrix} x \\ y \end{pmatrix} = PM = \begin{pmatrix} \frac{P_{11}X+P_{12}Y+P_{13}Z+P_{14}}{P_{31}X+P_{32}Y+P_{33}Z+P_{34}} \\ \frac{P_{21}X+P_{22}Y+P_{23}Z+P_{24}}{P_{31}X+P_{32}Y+P_{33}Z+P_{34}} \end{pmatrix} = \begin{pmatrix} \frac{P_1 M}{P_3 M} \\ \frac{P_2 M}{P_3 M} \end{pmatrix} \tag{3.20}$$

where P_k is the k^{th} row of the projection matrix P assuming a projective model, and the point $\hat{m}_i = (\hat{x}_i, \hat{y}_i)$ correspond to the projection of the point $M_i = (X_i, Y_i, Z_i)$ in the image.

3.6.1 Formulation

Adding the constraint 3.20 in the resolution of Equation (3.19) implies to solve a non-linear problem since M_i is unknown at t and therefore significantly increases the computational burden of our framework. In order to reduce the complexity of such an approach, we use the assumption that the point M_i does not significantly change between two successive steps (due to the acquisition frequency and the relative low speed of the tracked features). Therefore, it means that $M_i^t \approx M_i^{t-1}$ and when solving the equation of constrained motion we use the previously computed estimation of M_i and after the motion is solved, we update the estimation of M_i. This allows to keep a linear system where we take into account constraints (geometric or mechanical) in a generic way: adding constraints in the equation of dynamic ($\mathbf{Ma} = \mathbf{f}$) is usually performed by adding a term $\mathbf{H}^T\lambda$ where $\mathbf{H}$ is a matrix containing the constraint directions (how the vertices are constrained) and λ is a vector of Lagrange multipliers containing the constraint force intensities which is an unknown. In our case, the matrix $\mathbf{H}$ is a sparse diagonal matrix where only fixed vertices have non-null coefficients (such as boundary conditions). This will therby be expressed as:

$$(\mathbf{M} - h\mathbf{B} - h^2\mathbf{K}) \cdot \mathbf{dv} = h\mathbf{f}(\mathbf{x}_t, \mathbf{v}_t) + h^2\mathbf{K} \cdot \mathbf{v}_t + h\mathbf{H}(\mathbf{x}_t)^T\lambda \tag{3.21}$$

The resolution of this equation can be efficiently achieved by, first computing the motion without constraint (called *free-motion*) that will solve the linear system $\mathbf{A} \cdot \mathbf{x} = \mathbf{b}$ and give a first estimation of M_i and then use an iterative algorithm like Gauss-Seidel to find the λ and correct the *free-motion* to have the final constrained motion (detailed in Guébert et al. (2008)) and thereby, update the estimated point M_i which will now satisfy both mechanical and geometrical constraints.

3.6.2 Evaluation

We conduct experiments by computing the mean reprojection error using first computer-generated data (see Figure 3.12). The unification of physical and projective constraints permits to reduce considerably the reprojection error where we obtain error less than 0.8 pixel in contrast to purely physical formulation where the error is around 1.8 pixel.

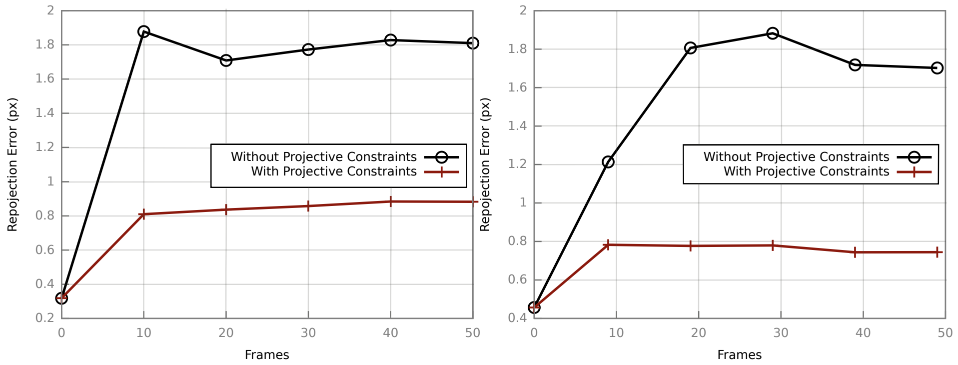

(a) **(b)**

Figure 3.12: Experiments with synthetic data with in (a) and (c) the reprojection error with and without accounting for projective constraints for the first and second shape perspectively, and in (b) and (d) the superimposition of the recovered shape (in green) on the ground truth (black) for the first and second shape perspectively.

We further test the projective constraint correction with the previous dataset. We compute the 3D reconstruction error between the recovered mesh and the ground-truth as well as the reprojection error. The results are illustrated in Figure 3.13.

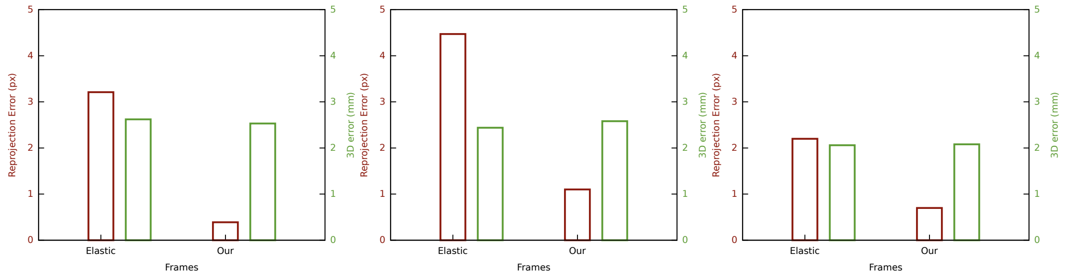

(a) Deformation 1 **(b)** Deformation 2 **(c)** Deformation 3

Figure 3.13: Evaluation of the silicone dataset of the geometric constraints correction.

In deformation 1, the reconstruction error is reduced to 2.53 mm as well as the reprojection error with 0.39 pixel and 3.21 pixels previously. In deformation 2, the re-projection error is dramatically reduced with an error of 0.92 pixel in contrast with an error of 4.47 pixels while deformation 3 shows that both methods produce very close reconstruction error with respectively 2.06 mm and 2.08 mm. The reprojection error is however considerably reduced when using the geometrical constraint with an error of 0.70 pixel while purely mechanical methods exhibit an error of 2.20 pixels.

Overall, in all the deformations, the re-projection error are below *one pixel* when using geometric constraint correction, way below the purely physical method. 3D reconstruction errors are however very close to each other for both techniques and remain for all the experiments below *3 mm*.

3.7 Dealing with Self-occluded Regions

Solving the system of equations 3.21 yields to recover the 3D shape that will satisfy both physical and geometrical constraints, and thus by finding the equilibrium between internal and external forces. However, when dealing with occluded regions, extra care has to be taken in the expression of external loads. Indeed, the physical model can be over-constrained by erroneous external forces and can be forced to fit occluded features that are subject to erroneous positions. This can highly damage the recovered shape as illustrated in Figure 3.14.

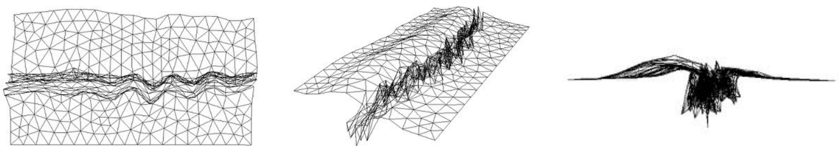

Top view Perspective view Front view

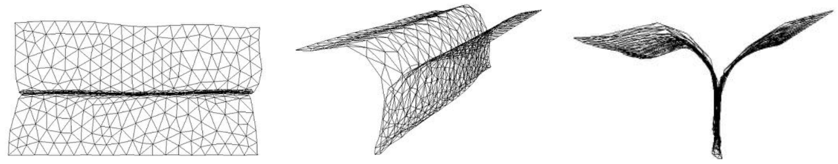

Top view Perspective view Front view

Figure 3.14: The inputs to the self-occlusion problem are the unreliable feature points that damage the mesh. (a), (b) and (c) The recovered mesh under different views without handling self-occlusions. (d), (e) and (f) The mesh under different views with our generic constraint based on equal force distribution to handle self-occlusions.

3.7.1 Formulation

In order to resolve occlusions, several strategies have been considered. Some rely on a preliminary stage that aims to reject outliers directly from the input image, leading to detect the occluded map on the mesh Pizarro and Bartoli (2012). Other methods detect self-occlusions as warp shrinkage areas where the warp is constrained to shrink rather than to fold Gay-Bellile et al. (2010), whereas visual consistency can also be considered in multiframe reconstruction Shaji et al. (2011).

These approaches assume strong prior on the type of deformation, which can hardly be considered for elastic object where the number of degrees of freedom is high, or relies on a two-stage processing to detect occluded areas. We introduce here a weak, computationally cheap and generic constraint that easily fits into our framework. By taking advantage of the ability of the physical model to estimate 3D shape where no external loads are present. We reduce the number of features according to the resolution of the underlying mesh, instead of simply evict outliers. Whereas in previous approaches the number of features might not be large enough to recover self-occluded regions, it permits in our case to equally distribute the stretching forces to ensure a global physical consistency. We thus select among the set of features $U = \{U_i \in \mathbb{R}^3\}$ a subset of features with high detection scores at the corresponding u_i and impose a minimal relative distance between them:

$$\|\mathbf{U}_i - \mathbf{U}_j\| \geq \tau \tag{3.22}$$

where $\mathbf{U_j}$ is the closest neighbour of $\mathbf{U_i}$ and τ is the initial length of the edge corresponding to the largest tetrahedral element of the model. Locally selecting the features according to their detection scores make the tracking and the detection of possible tracking failure easier, thus limiting the introduction of outliers in the visual features. Contrary to existing approaches which require many features for correctly handling occlusions, we take advantage of the ability of the mechanical model to predict the shape in areas with unobserved data, especially in occluded areas, and select a set of reliable and roughly equally distributed features to guide the mechanical model. This constraint has only to be considered at initialisation, where the mesh is at its rest configuration, thereby, the extensibility property of the material remains valid and self-occlusions are efficiently handled.

3.7.2 Evaluation

We confront our method to two video sequences with self-occluded surfaces. We performed a comparison between the inextensible method and our method without self-occlusions handling. We compared the 3D reconstruction error with respect to the ground truth by computing the mean and RMS error.

Deformation 5 involves a surface with an extensibility of 10% and an occluded region of 25% whereas deformation 6 is done on a surface with an ex-

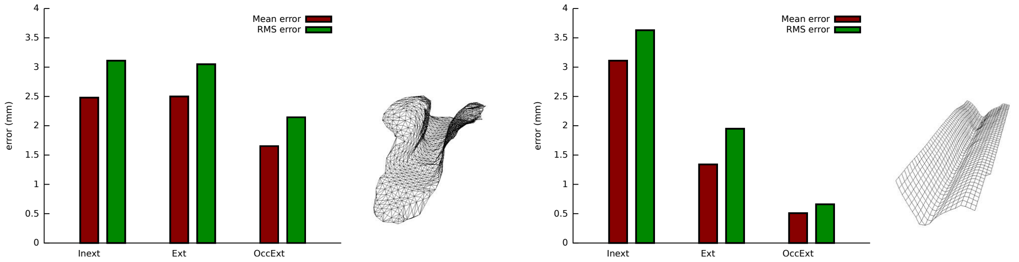

(a) Experiment 5: Comparison **(b)** Ground truth **(c)** Experiment 6: Comparison **(d)** Ground truth

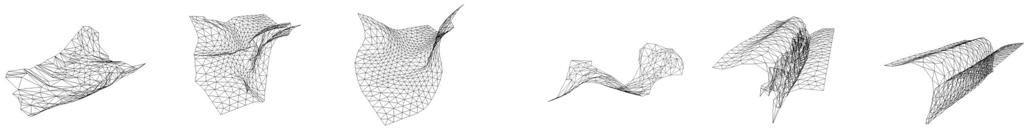

(e) Inext **(f)** Ext **(g)** OccExt **(h)** Inext **(i)** Ext **(j)** OccExt

Figure 3.15: Experiments conducted on the silicone dataset with self-occluded regions. The graphics in (a) and (c) show the 3D error computed between the recovered mesh and the ground truth using the inextensible method (Inext), our method without self-occlusion handling (Ext) and our method with self-occlusion (OccExt) on experiment 5 and 6 respectively. (b) and (d) show the ground truth. (e), (f), (g), (h), (i) and (j) show the 3D recovered mesh using each technique.

tensibility of 30% and an occluded region of 60% (see Figure 3.16). Salient landmarks are tracked over frames using a classical optical flow algorithm which is known to be prone to drifting. Thereby, we applied a very strict threshold on the detector to reduce the possible cases of drifting. Once the initial set of features is extracted we apply the condition of Eq. 3.22 with a value $\tau = 10$ mm. The features lying on the occluded region will nevertheless remain subject to positioning error. However, the equal distribution of the stretching forces permits to minimize their impact on the recovery of the global shape.

The results illustrated in Figure 3.15 show that in both experiments our method produces a visually correct 3D shape with the lowest 3D error in comparison with other approaches, that fail in recovering the 3D surface. We report a mean error of 0.51 mm and a RMS error of 0.66 mm for deformation 5 and a mean error of 1.72 mm and RMS error of 2.25 mm for deformation 6.

3.8 Surgical data

Our aim is to assess the robustness of our approach in a real environment (specular lights, beating heart, respiratory motion, instrument occlusions) and the ability of our non-rigid registration in recovering 3D shapes from a single view. We tested our approach on a video of *in-vivo* porcine liver showing one of the

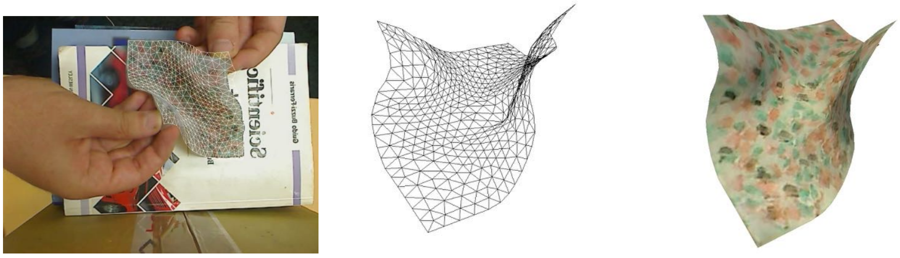

(a) Deformation 5 **(b)** 3D mesh **(c)** Re-texturing

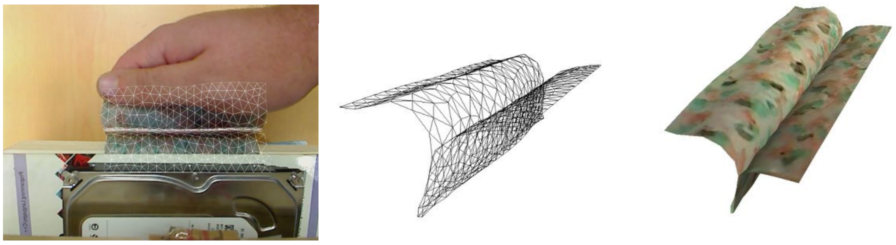

(d) Deformation 6 **(e)** 3D mesh **(f)** Re-texturing

Figure 3.16: Monocular 3D reconstruction of self-occluded elastic surfaces. (a) and (d) the camera view of the registered mesh. (b) and (e) the recovered 3D shape. (c), (f) the recovered 3D shape with re-texturing.

liver lobe undergoing elastic deformation and partially folding during a minimally invasive surgery. We used a monocular laparoscopic camera from Karl Storz Endoscopy acquiring video stream at a rate of 25 FPS with image resolution of 720 × 576 pixels and data computed from pre-operative scans. These data permit to generate the necessary mesh for a correct modeling of the liver in three steps: segmentation, volume generation and parametrisation. These 3 steps are detailed in chapter 5, we give here a short explanation of the processing of pre-operative data.

The volume issued from CT-scanner is used to generate the liver surface. This segmentation is done semi-manually using active contour techniques (Snakes). A volumetric mesh is necessary for a finite element modeling. The number of elements is to be chosen carefully in order to ensure real-time performance as well as sufficient accuracy. Our model is composed of 1024 linear P1 tetrahedral elements. The elastic parameter is extracted from a textbook and does not suit exactly the considered liver and is set according to Peterlík et al. (2012); Umale et al. (2011) to E=3.5 KPa. The results illustrated in Figure 3.17 report a visually correct 3D elastic augmentation of the liver model on the laparoscopic image with a good 3D shape recovery.

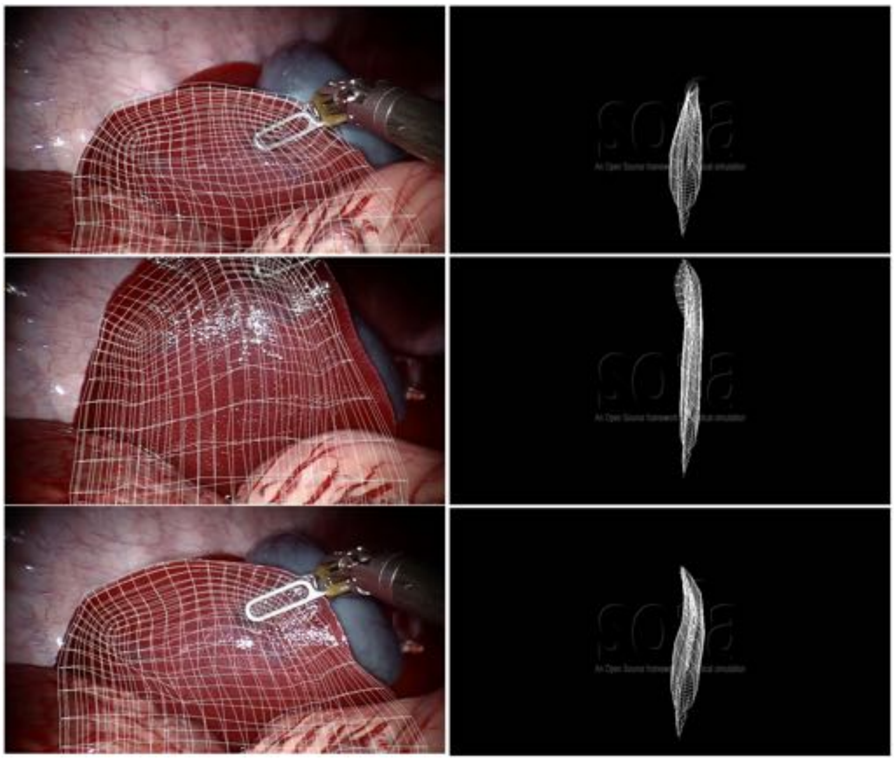

Figure 3.17: 3D elastic augmentation of the mechanical model on laparoscopic images acquired form a monocular camera. The augmentation is effective (left) even when the deformation generated by the instrument forces the lobe of the liver to fold (right).

3.9 Conclusion

In this chapter, we have proposed a real time and efficient method to capture and augment highly elastic objects from a single view. This method makes use of a mechanical model of the deformable object in the context of non linear elasticity. With respect to many existing approaches, this method makes it possible to avoid the definition of adhoc constraints to solve the ambiguities of reconstruction. The conducted experiments proved that the method is flexible in the sense that a classical model - the St Venant-Kirchhoff model- has proven to be sufficient to handle various applications with a good accuracy. In addition, we have shown that the method does not require an accurate knowledge of the material stiffness. Moreover, we show that partial and self-occlusions can also be efficiently handled since a few number of image points are sufficient to yield good results.

The major limitation of this method is that it is applicable only on a certain range of deformations, and cannot guarantee to capture large deformations that occur in 3D space. In addition, the homogenous elastic model proposed here is suitable for surface deformations but is not applicable for the localisation of tumors. In the next chapter, we propose to use a stereo-endoscope that will permit to estimate more efficiently 3D motion of the liver. This motion field will drive an heterogenous mechanical model that takes into account vascular network to faithfully compute internal deformations.

CHAPTER 4

IMAGE-GUIDED SIMULATION OF HETEROGENEOUS LIVER TISSUE

Contents

4.1 Introduction

In order to establish a full AR system for MIS, a number of difficult problems have to be solved Nicolau et al. (2011). The abdominal cavity undergoing laparoscopic surgery remains a very challenging environment for computer vision tasks. Surgical instruments interacting with the liver may cause large occlusions, illumination variations caused by the endoscopic light and the liver bleeding or smokes due to electrocautery may disturb organ motion tracking and 3D structures recovery. Among the most difficult and still unsolved issues is the capacity to tackle, in real time, elastic deformations of the liver. The liver can undergo large deformations due to surgical tools interaction or due to respiratory motion and heart beating. Currently, most of the existing AR systems handle rigid motions of organs and only a very limited number of papers address the problem of elastic organ deformation.

This chapter highlight our contributions on AR for Hepatic surgery accounting for large liver deformations. We present an approach that relies on the estimation of liver motion to drive a heterogeneous mechanical model capable of translating the liver behaviour (see Figure 4.1). First, our approach for three-dimensional liver surface reconstruction is described, in addition to the temporal tracking of liver deformations. We then present a clusters-based filter that aims to add robustness to visual tracking. Finally, the biomchanical liver that account for vessels heterogeneity is detailed and our non-rigid approach expressed as an energy minimization is described.

4.2 Three-dimensional Liver Surface Reconstruction

The first step towards an Augmented Reality system is the understanding of the environment to be augmented. This step is based on the analysis images captured from endoscopic cameras. In this section we present our method to reconstruct the surface of the liver using well-established computer vision algorithm. This approach involve two stage: Sparse reconstruction based on stereoscopy and a surface shape estimation using Moving Least Square approximation.

4.2.1 Sparse 3D Reconstruction using Stereoscopy

Our 3D shape estimation approach is a feature-based method using a stereo-endoscopic camera. Prominent features are detected and matched in the image pair to recover a sparse 3D point cloud representing the liver and the surrounding tissues. In the following, we describe the camera model and the reconstruction method based on linear triangulation.

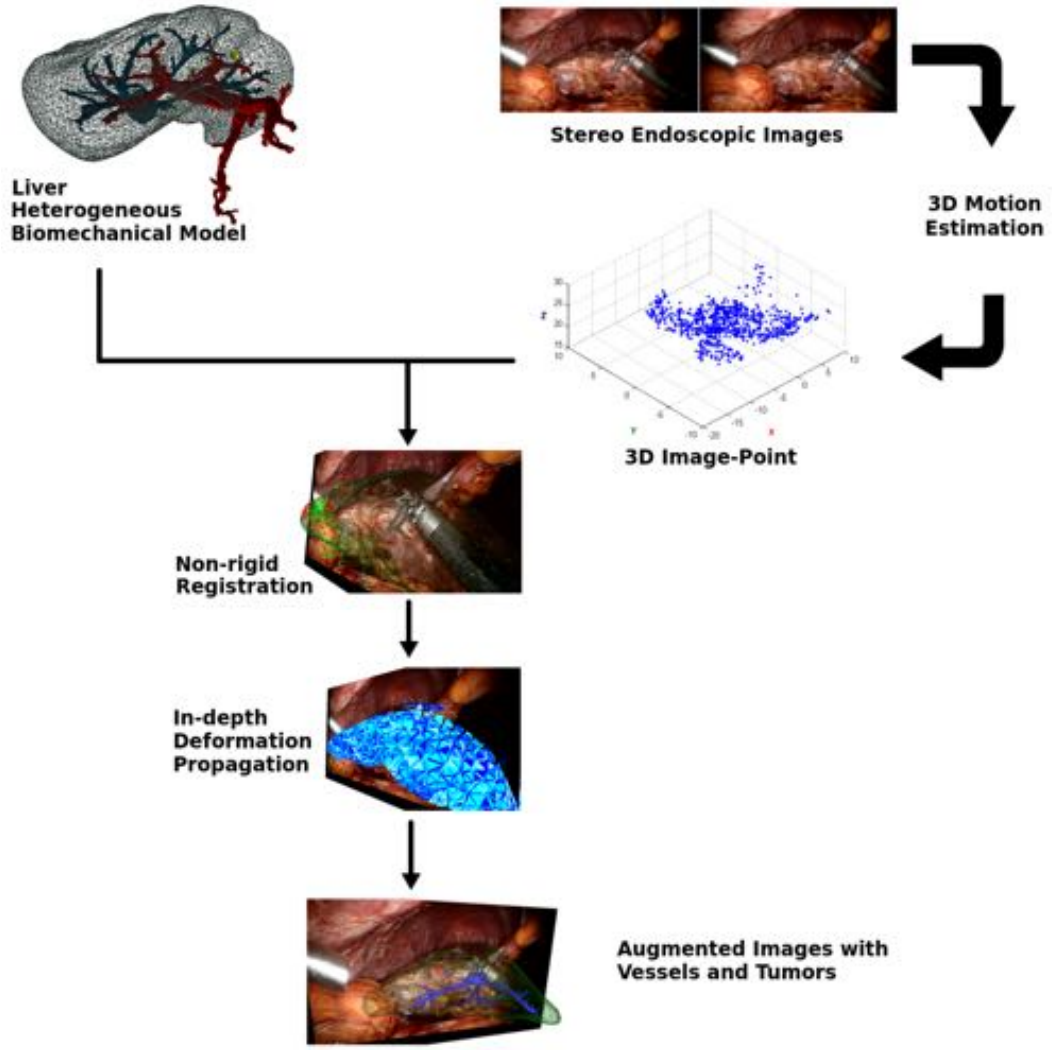

Figure 4.1: Computational flow of the method: The biomechanical model guided by the 3D image-points recovered from intra-abdominal image pair permits to propagate partial tissue deformations to vessels and tumors.

Camera Model and Calibration

As described in chapter 2, the endoscopic camera is inserted through a trocar via small incision or natural orifice such as navel. In order to correctly retrieve data from the camera, an appropriate model has to be chosen. The endoscopic camera can be model as a pinhole camera defined by its intrinsic and extrinsic parameters. The intrinsic parameters represent the optical features of the device, usually the lens focal and its position regarding the center of projection, where the extrinsic parameters describe the localisation (rotation and translation) of the camera in a reference coordinate system. The lens of the endoscopic camera are very sensitive to distortion, that generate aberration while acquiring informations. These distortions can be effectively modelled using radial and tangential distortion coefficients.

The camera is also equipped by a light source that illuminates the abdominal cavity. For Structure-from-Shading techniques, modelling the light source is needed, however, since our method only exploit the optical device, no light model is required.

The pinhole camera model establishes the relation between a point in the surgical environment and the image plane, in other words it describes the mapping of the 3D point $M = [XYZ1]^T$ with the 2D image point $m = [xy1]^T$ following:

$$\mathbf{m} = \mathbf{A}\begin{bmatrix} R & t \\ 0 & 1 \end{bmatrix}\mathbf{M} = \mathbf{PM} \tag{4.1}$$

where **A** is a matrix of the intrinsic camera parameters and **R** and **t** the rotation and translation matrices that describe the extrinsic position and orientation of the device in the world coordinate system. The matrix **P** is called camera matrix or projection matrix.

The camera parameters are determined through a calibration step. Camera calibration is a well-studied process in computer vision Zhang (2000) with a large number of techniques and toolkits. It is often the primary step when dealing with cameras as it allows systems to relate what appears on an image and where it is located in the world. It has been successfully translated to surgical vision where the calibration of endoscopic camera is done offline, pre-operatively. However, some studies report the ineffectiveness of pre-calibration for surgical context. Indeed, during surgery the model of the optical sensors may undergo changes due to zooming and focusing, or due to moving scope. For that purpose online camera calibration has been investigated Stoyanov and Yang (2005); Barreto et al. (2009), but with limited results for MIS.

Despite calibration is a well-established technique, it can be quite complex when dealing with laparoscopic camera and remains an important issue to be addressed. Current calibration method may produce significant error (our experiments report an average reprojection error of more than 1 pixel), which can highly affect the reconstruction. This can be explained by the relative small baseline.

Stereo Correspondence

Once the camera is calibrated, the exploitation of endoscopic images is possible. We choose to rely on passive technique based on stereoscopy in order to estimate the three-dimensional shape of the liver since it does not need additional hardware modification. Stereoscopy is also currently the most reliable and reproducible technique for 3D reconstruction in surgical vision, when comparing with non-rigid SfM and non-rigid SLAM.

Thus, using stereoscopy, we have as input two pairs of images $\mathscr{I}_l$ and $\mathscr{I}_r$. On this stereo pairs $(\mathscr{I}_l, \mathscr{I}_r)$ we need to extract point of interest (or features) that are sufficiently reliable for reconstruction and tracking. Where several detectors have been developed in the literature Gauglitz et al. (2011); Mikolajczyk and Schmid (2005), we use Speeded-up Robust Features (SURF) detector. Our choice for SURF over other detector is motivated by its particular well-suitability for robotic-guided endoscopy applications Elhawary and Popovic (2010b). Moreover, our tests have shown that it performs well with liver surface texture.

SURF is both a feature detector and descriptor. The detector is robust to affine transformation, rotation and illumination changes, and is computationally fast, it is based on the determinant of the Hessian blob detector to extract distinct keypoints. Given a point $\mathbf{x} = (x, y)$ in an image $\mathscr{I}$, the Hessian matrix $H(\mathbf{x}, \sigma)$ in $\mathbf{x}$ at scale σ is defined as follows

$$H(\mathbf{x}, \sigma) = \begin{bmatrix} L_{xx}(\mathbf{x}, \sigma) & L_{xy}(\mathbf{x}, \sigma) \\ L_{xy}(\mathbf{x}, \sigma) & L_{yy}(\mathbf{x}, \sigma) \end{bmatrix} \tag{4.2}$$

where $L_{xx}(\mathbf{x}, \sigma)$ is the convolution of the Gaussian second order derivative with the image I in point $\mathbf{x}$, and similarly for $L_{xy}(\mathbf{x}, \sigma)$ and $L_{yy}(\mathbf{x}, \sigma)$. This second order Gaussian derivatives can be evaluated at a very low computational cost thanks to the use of integral images.

The features are then selected if the determinant of the Hessian matrix $det(H)$ in above a certain threshold τ:

$$det(H) > \tau \tag{4.3}$$

The determinant of the Hessian in often called the *Hessian Response* and gives a measure of reliability of the detected feature.

When using SURF detector on the stereo pairs $(\mathscr{I}_l, \mathscr{I}_r)$ with an appropriate threshold we extract two sets of features $\mathbf{E_l} = (x_{1_l}, \cdots, x_{n_l})$ and $\mathbf{E_r} = (x_{1_r}, \cdots, x_{m_r})$ where we need to estimate for each feature $x_i = (u_i, v_i)$ the 3D point $X_i = (U_i, V_i, W_i)$. This is done by establishing a correspondence between image points $x_l \longleftrightarrow x_r$, with a descriptor-based matching method.

Descriptors are used to find correspondences between features in pairs of images. A descriptor is a distinct fingerprint assigned to each keypoint detected w.r.t its pixel properties and its response to the detector. We rely on SURF since it also provides a descriptor robust to noise. It uses the Haar wavelet response of the keypoint region to build a binary descriptor represented as a vector of 128 dimension. The matching is done by computing a nearest neighbor search on

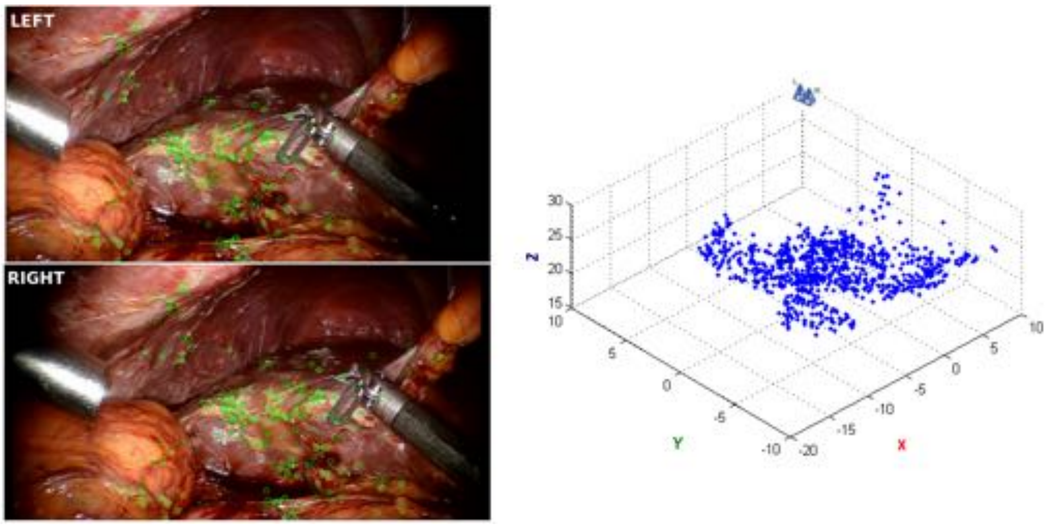

Figure 4.2: 3D Estimation from a laparoscopic image pair of the abdominal cavity showing a part of the liver. (a): SURF features detection on image pair acquired from the Da Vinci Robot. (b): the resulting sparse 3D point set $\mathbf{y}$ plotted.

descriptors vectors based on an euclidean distance while ensuring to satisfy the epipolar constraints Puerto and Mariottini (2012). A sparse set of m 3D points, denoted by $3 \times m$ coordinate vector $\mathbf{z}$, is by then reconstructed using a triangulation algorithm described below. Examples of 2D matched features and reconstructed 3D points from laparoscopic images are shown in Figure 4.2.

Triangulation

The triangulation Hartley and Sturm (1995) is the process of estimating the position of a 3D point X from its image points x and x' in two views knowing the camera matrices of those views P and P' respectively, issued from the calibration (see Figure 4.3). This amount to find the point X that exactly satisfies:

$$\mathbf{x} \approx \mathbf{P}\mathbf{X} \quad \mathbf{x}' \approx \mathbf{P}'\mathbf{X} \tag{4.4}$$

In theory, a naive back-projection of the rays from the measured image points will determine the 3D point X, however, in practice the measured image point x and x' contains *error*, thus, the rays will not intersect in general. It is then necessary to estimate a best point of intersection by the definition and minimization of a suitable cost function. The two rays corresponding to a matching pair of points $\mathbf{x} \longleftrightarrow \mathbf{x}'$ will meet in space if and only if the points satisfy relationship:

$${}^{\top}\mathbf{x}' F \mathbf{x} = 0 \tag{4.5}$$

where F denotes the fundamental matrix defined for a pair of cameras. In reality, the correct values of the corresponding image points should be points $\hat{x} \longleftrightarrow \hat{x}'$ lying close to the measured points $x \longleftrightarrow x'$ and satisfying the equation $^{\top}\hat{x}' F\hat{x} = 0$ exactly. Under the assumption that the imaged points are perturbed by Gaussian noise, the optimal, maximum likelihood solution minimizes the *l2* reprojection error

$$d(\mathbf{x}, \hat{\mathbf{x}})^2 + d(\mathbf{x}', \hat{\mathbf{x}}')^2 \tag{4.6}$$

where $d(*,*)$ represents Euclidean distance, subject to the epipolar constraint

$$^{\top}\hat{\mathbf{x}}' F\hat{\mathbf{x}} = 0 \tag{4.7}$$

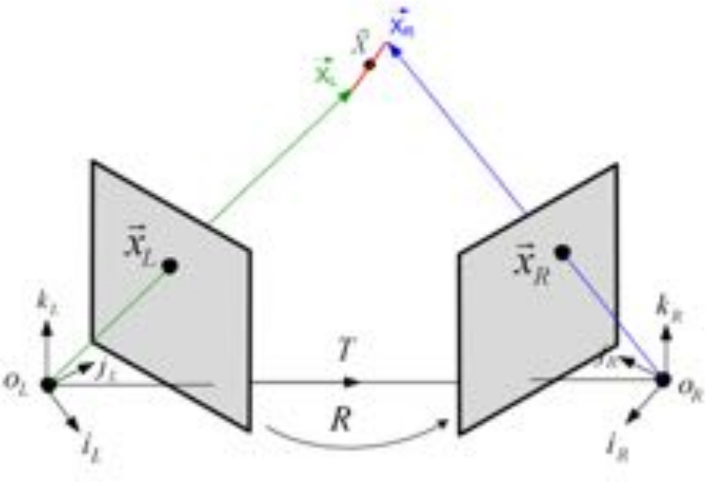

Figure 4.3: Triangulation.

Once $\hat{\mathbf{x}}$ and $\hat{\mathbf{x}}'$ are found, the point X may be found by any triangulation method.

We used the Iterative Linear Least Square Triangulation method (*Iterative-LS*) Hartley and Zisserman (2004) to find the 3D point X that satisfies 4.4. In this method the measurement $\mathbf{x} = \mathbf{P}\mathbf{X}$, $\mathbf{x}' = \mathbf{P}'\mathbf{X}$ can be combined into a form $\mathbf{A}\mathbf{X} = \mathbf{0}$ which is an equation linear in $\mathbf{X}$.

First the homogeneous scale factor is eliminated by a cross product to give three equations for each image point, of which two are linearly independent. For example for the first image $x \times (PX) = 0$ and writing this out gives:

$$\begin{aligned} x(p^{3T}X) - (p^{1T}X) &= 0 \\ x(p^{3T}X) - (p^{1T}X) &= 0 \\ x(p^{3T}X) - (p^{1T}X) &= 0 \end{aligned} \tag{4.8}$$

where p^{iT} are the rows of P. These equations are linear in the components of X.

An equation of the form $AX = 0$ can then be composed, with

$$A = \begin{bmatrix} xp^{3T} - p^{1T} \\ yp^{3T} - p^{2T} \\ x'p'^{3T} - p'^{1T} \\ y'p'^{3T} - p'^{2T} \end{bmatrix} \tag{4.9}$$

where two equations have been included from each image, giving a total of 4 equations in 4 homogeneous unknowns. These equations define X only up to an indeterminant scale factor. By setting $X = (U, V, W, 1)^T$ the set of homogeneous equations, $AX = 0$, is reduced to a set of 4 inhomogeneous equations in 3 unknowns. One can find a least-squares solution to this problem by using the Singular Value Decomposition.

This process is repeated several times to reduce the reprojection error, by adaptively change the weights of the linear equations so that the weighted equations correspond to the errors in the image coordinate measurements.

Several triangulation methods exist such *optimal triangulation* Hartley and Sturm (1995) which amounts to finding all roots of a degree-six polynomial. Nevertheless, they are relatively non-trivial and difficult to implement and their computational cost can be considerable Lindstrom (2010).

4.2.2 3D Surface Reconstruction using Moving Least-Squares

Our non-rigid registration method is based on a point-to-point approach, thus a sparse surface reconstruction is sufficient. Nevertheless, the sparse set $\mathbf{z}$ of recovered 3D points may contain erroneous points which can damage the registration. We propose to approximate a surface on the set of points $\mathbf{z}$ using Moving Least-Squares surface (MLS) approach in order to reduce the erroneous points.

In the literature, several approaches has been proposed to make the 3D reconstruction more accurate, through direct outliers rejection stage or using smoothing techniques. In order to recover the 3D heart surface, a growing scheme approach was proposed in Stoyanov (2012) that rejects outliers by ensuring their uniqueness during a propagation step from sparse to dense reconstruction. Using spatio-temporal constraints, Richa et al. (2010b) proposed to exploit the quasi-periodicity of the heart beating motion to reduce the reconstruction disturbances by using a time-varying dual Fourier series as a prediction model that also permit to handle occluded surface. Another way to regularize noisy image information is to use an underlying geometrical model such as in Richa et al. (2010c) where a Thin Plate Spline (TPS) is used to approximate the heart surface deformation.

MLS are non-dependent on image texture since it purely relies on geometric properties and no temporal constraints nor prior shape knowledge are needed to yield good results. Thereby, it makes it a generic technique for the computation of 3D shapes, even in the presence of noisy image data.

Moving Least-Squares surface Moving Least-Squares surface (MLS) is a mesh-free, non-parametric method to approximate a surface from a set of unstructured scattered point introduced by Levin (2004). It has been widely used in computer graphics for surface reconstruction resulting in the emergence of various scanning method. The attractivity of MLS resides in the fact that the reconstruction in done by local computations which permit to generate a surface that is smooth everywhere. In addition it permits to compute a very good approximation of the intrinsic properties of the surface such as normal and curvature directly from a noisy point-cloud.

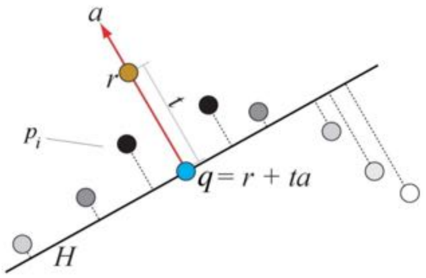

Figure 4.4: Processing steps for the Moving Least Squares approximation. From Amenta and Kil (2004). MLS energy function of Step 1, sums up the weighted distances from the fixed input points in P to the plane with normal a through the point $q = r + ta$. The weight on an input point $p_i \in P$, denoted here by its shade of grey, is a function of the distance from pi to q.

To determine MLS surface given a point set $P = \{p_i \in \mathbb{R}^3\}$, a projection procedure which projects any point near the point set onto the surface using a local approximation is conducted (see Figure 4.4).

Given a point $r \in \mathbb{R}^3$, the process follows two steps. First the computation of a local patch, then the projection of the query point r onto the surface using a polynomial function :

- **S**tep 1 Compute a local reference plane in the neighborhood of r : Find a plane H with normal vector $a \in \mathbb{R}^3$ passing through some point $q = r + ta$ (for some $t \in \mathbb{R}$) such that $\|a\| = 1$ and H minimizes the least-squares error:

$$\sum_{p_i \in P} < a, p_i - q >^2 \theta(\|p_i - q\|) \tag{4.10}$$

Here, $< a, p_i - q >^2$ is the squared distance from each point $\{p_i\}$ to the plane H, and $\theta(\|p_i - q\|)$ is the weighting monotonic function (Gaussian).

- **S**tep 2 Project r on the surface : We consider the points x_i to be the orthogonal projections of the points p_i on the plane H with projected distance $f_i = < a, p_i - q >$ oriented with normal a and origin q. Thus, we apply the MLS function approximation which consists of construction of a bivariate polynomial $\tilde{g} \in \mathbb{R}^3$ of degree m (here we take $m = 3$) which locally minimizes the least-squares error around q:

  $$\sum_{p_i}(g(x_i) - f_i)^2 \theta(||p_i - q||) \tag{4.11}$$

  That amounts to project r along the normal with distance $\tilde{g}(0)$ (local approximation of the surface at q).

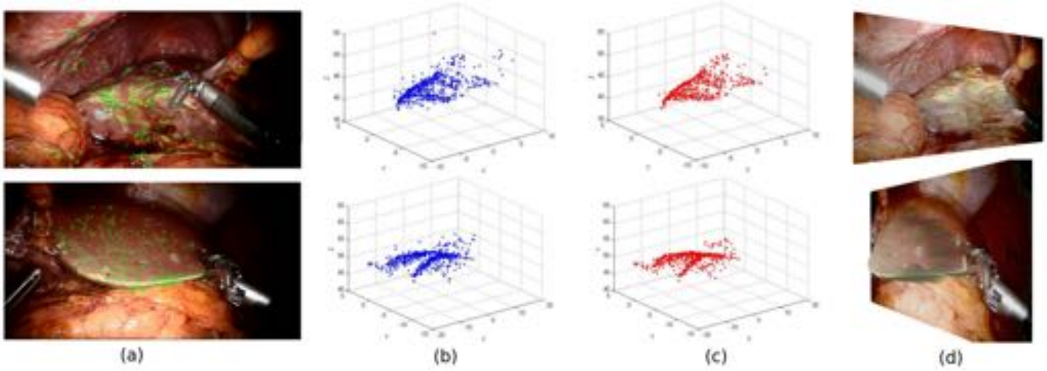

Figure 4.5: Stereoscopic flow estimation on laparoscopic images of the abdominal cavity showing a part of the liver in two different cases with (top) high textured liver and (bottom) low textured liver: (a) Original input images, (b) the resulting sparse 3D point set **z** from stereo matching, (c) the resulting sparse 3D point set **y** from MLS outliers filtering, (d) the projected image on the reconstructed surface.

MLS surface approximation performs well when the targeted point set is representing a concave or convex surface. This assumption can easily been considered with the liver knowing the shape of the lobes. However, since noisy data is always prone to ambiguity between a noisy smooth region and a sharp feature, some false-positive statement may still occur. Figure 4.5 illustrate MLS surface approximation performed on point cloud resulting from a 3D sparse reconstruction of liver surface.

4.3 Tracking the liver tissue using Clusters-based Filter

Tracking organ tissue is a key component in an AR framework. We have presented in the previous chapter several methods that aim to perform a robust tissue motion estimation. However, even these techniques have been extensively tested on the heart and kidney, very limited works attempted to conduct experimentation on the liver. This can be explained by the fact that the heart undergoes cyclic deformation that can be predicted, and the kidney undergoes more rigid transform than elastic deformation, while the liver may be subjected to high elastic deformation that distorts the tissue and may cause the loss of features. In addition, the liver tissue is known to contain several repeated patterns, which make it difficult to perform descriptor matching.

4.3.1 Feature-based Direct Tracking

Our visual tracking follows the work by Elhawary and Popovic (2010b) who evaluated the combination of the Lucas-Kanade (LK) optical flow Bouguet (2002) and SURF detector for robotic-guided endoscopy. This study showed the robustness and accuracy of this combination and its usability for conventional laparoscopic surgery.

Lucas-Kanade Lucas and Kanade (1981b) algorithm is an iterative optical flow that allows the tracking of features in successive pairs of images under the assumptions that the local displacement of a pixel neighborhood is small and its brightness is constant over frames.

Let us denote $I(x, y, t)$ the intensity of a pixel $p = (x, y)$ at a time t. LK algorithm aims to find the position of the pixel p at $t + 1$ based on the brightness consistency equation:

$$I(x, y, t) = I(x+u, y+v, t+1) \tag{4.12}$$

Using Taylor Expansion, we can linearise $I(x+u, y+v, t+1)$ at (x, y, t) which gives:

$$I(x+u, y+v, t+1) \approx I(x, y, t) + I_x \cdot u + I_y \cdot v + I_t \tag{4.13}$$

$$I(x+u, y+v, t+1) - I(x, y, t) = I_x \cdot u + I_y \cdot v + I_t \tag{4.14}$$

From the assumption of constant brightness we deduce $I_x \cdot u + I_y \cdot v + I_t \approx 0$, the equation of motion at each pixel is given by:

$$\nabla I.[uv]^T + I_t = 0 \tag{4.15}$$

In order to recover the motion (u, v), equation 4.15 has to be solved. However, only the flow normal to the image gradient can be deduced form Eq 4.15. To overcome this issue, LK optical flow uses a spatial coherence constraint assuming that $j \times j$ neighbourhood around the pixel p has the same motion. This leads to a set of j linear equations that can be written in the form of $\mathbf{Ad} = \mathbf{b}$:

$$\begin{bmatrix} I_x(p_1) & I_y(p_1) \\ I_x(p_2) & I_y(p_2) \\ \vdots & \vdots \\ I_x(p_k) & I_y(p_k) \end{bmatrix} \begin{bmatrix} u \\ v \end{bmatrix} = - \begin{bmatrix} I_t(p_1) \\ I_t(p_2) \\ \vdots \\ I_t(p_k) \end{bmatrix} \tag{4.16}$$

This system is over-constrained since it has more equations than unknowns, therefore the solution is approximated by the least squares principle by solving the system $(\mathbf{A}^T\mathbf{A})\mathbf{d} = \mathbf{A}^T\mathbf{b}$ following:

$$\underbrace{\begin{bmatrix} \sum_i^k I_x I_x & \sum_i^k I_x I_y \\ \sum_i^k I_x I_y & \sum_i^k I_y I_y \end{bmatrix}}_{(\mathbf{A}^T\mathbf{A})} \underbrace{\begin{bmatrix} u \\ v \end{bmatrix}}_{\mathbf{d}} = - \underbrace{\begin{bmatrix} \sum_i^k I_x I_t \\ \sum_i^k I_y I_t \end{bmatrix}}_{\mathbf{A}^T\mathbf{b}} \tag{4.17}$$

Solving this system yields to obtain the optimal (u, v) that satisfies the motion equation Eq 4.15, only if $(\mathbf{A}^T\mathbf{A})$ is invertible which is the case when tracking high textured regions.

A stop criteria is also considered when the spatial coherence assumption is violated; despite this criteria, LK algorithm can produce errors. Therefore, iterative refinement is usually considered when dealing with large movements Bouguet (2002).

This combination permits to track liver deformations, in presence of visual disturbances. However, the features loss is a major drawback in optical flow techniques, and does not permit to perform a long-term tracking.

In order to ensure a long term stability for the non-rigid registration, we propose an additional layer to the direct tracking. This layer called Cluster-based Filter (CbF) permits to create a set of n 3D control points, denoted by $3 \times n$ coordinate vector $\mathbf{y}$ that guides the biomechanical model. Instead of constraining the model directly with the extracted features, the clustering calculates a displacement field for each control point based on the adjacent features. Its benefits are twofold: *i)* It guaranties the minimization to remain stable since the number of control points (and the amount of external forces) is less subject to lost features. Moreover, it permits to avoid to over-constrain the corresponding tetrahedral element which can often tend towards instability. *ii)* This permits to keep only the needed features. Indeed, we can here exploit the capability of the mechanical model to estimate deformations with a reduced number of external loads. Figure 4.8 illustrates the clustering phase.

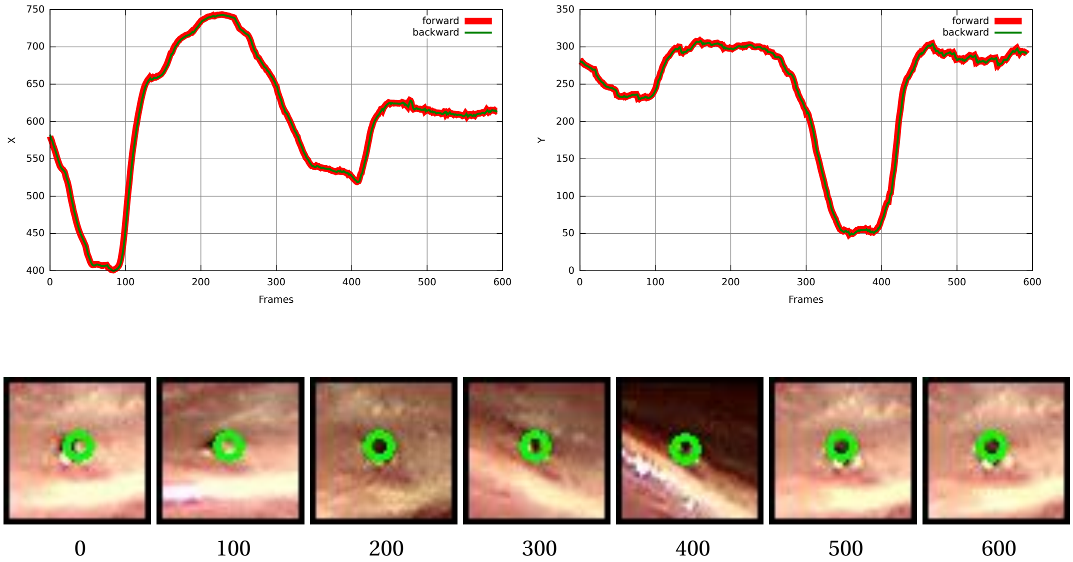

Figure 4.6: A SURF feature being tracked over time (600 frames) using LK optical flow. (top) tracking performed in both a forward and a backward time direction. Graph shows X and Y coordinates as a function of time. (bottom) 50 × 50 pixel window centred around the feature location at every 100 frames.

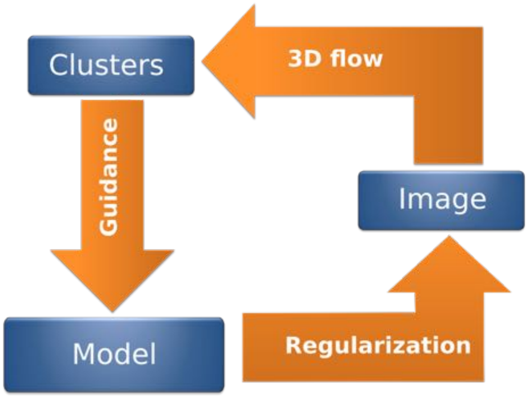

Figure 4.7: Clusters-based Filtering

4.3.2 Clusters Building

Let us denote $C = \{c_i \in \mathbb{R}^3\}$ the set of control points built form downsampling the set $\mathbf{y}$ of 3D points resulting from MLS approximation stage. Each control point defines a region of interest to group the surrounded features. The nearest features to the control point are assigned to the cluster by combining the Hessian responses of SURF detector and the Shepard's Inverse Distance Weighting (IDW). Shepard's IDW allows the nearby feature to the control point to have the largest weight while the Hessian response allows to prevent poor SURF detection. Furthermore, it can be expressed as follows:

$$\mathbf{D}(p) = q_p \sum_{i=1}^{k} \mathbf{w_i} d_i \tag{4.18}$$

where **D** is the weighted displacement of the control point p, k the total number of neighbors and d_i the displacement of the feature i. Assuming the quality is isotropic at each feature, we define a normalized measure of quality q_p for each control point as the average of SURF Hessian responses of its neighbors. $\mathbf{w_i}$ is the weight assigned to each control point given by:

$$\mathbf{w_i} = \frac{(\frac{r_c - h_i}{r_c h_i})^2}{\sum_{j=1}^{m} (\frac{r_c - h_j}{r_c h_j})^2} \tag{4.19}$$

where r_c is the radius of the cluster, h_i the distance of the feature from the control point and m the total number of neighbors.

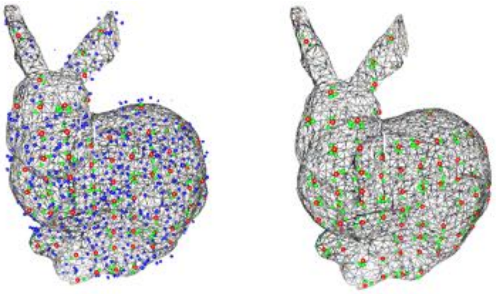

Figure 4.8: Clustering phase : (left) The two views of 3D point cloud estimated from stereo matching. The Blue sphere represents the rejected features. (right) Image is a representation of the clusters. Red sphere represents the Control Points and the Green sphere the essential features (neighbors).

4.3.3 Evaluation of the Cluster-based Filter

In order to provide quantitative evaluation of our approach, we first conduct experiments based on computer-generated data in order to easily and quantitatively compare the reference deformed mesh and the one obtained with our approach.

We evaluate the accuracy of the registration by calculating the Hausdorff Distance as a metric between the reference 3D mesh (that underwent a synthetic deformation) and the target 3D mesh (that underwent the deformation controlled by the tracked control points). This metric Nicolas Aspert (2002) is the reference metric for comparing two meshes in the Computer Graphics and the

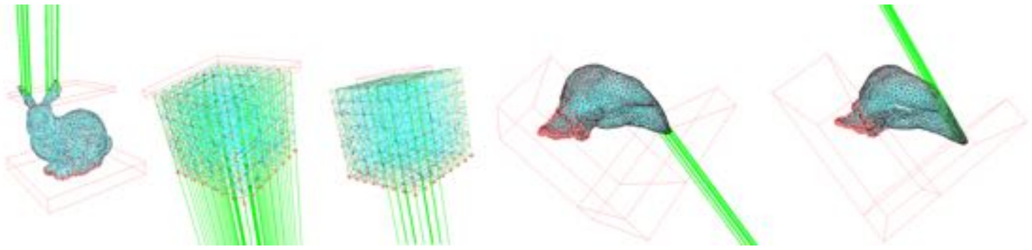

Figure 4.9: Trained synthetic data : From left to right : Ears deformations of the Stanford Bunny, large, small and local Cube deformation, local Human Liver deformation in opposite direction. The volumetric mesh composed of tetrahedra is displayed in blue. The fixed constraints are represented by red markers and the direction of the force field applied is illustrated by the green lines.

Reconstruction scientific community. In the following experiments, we use the Rounded Mean Square Error (RMSE) of the Hausdorff Distance as the metric.

For this evaluation we use three models: A Stanford Bunny, a Human Liver and a Cube, and three types of deformations, Large, Local and Small. Figure 4.9 illustrates the trained synthetic data.

In order to deform the 3D mesh, the displacement field of the control point has to be computed. Each control point is represented by a set of features. The influence of each feature on the displacement field of the control point is weighted by the feature quality (Hessian Response to SURF detector) and the distance of the feature from the control point. The table below shows the results of a comparative study of the weighted techniques:

Mesh	**Type of Deformation**	**Hessian**	**IDW**	**Combination**
Cube	Small Surface Pressure	0.030	0.033	0.032
	Local Surface Pressure	0.084	0.088	0.076
	Large Surface Pressure	0.083	0.092	0.087
Liver	1st Lobe elongation	0.193	0.165	0.165
	2nd Lobe Elongation	0.200	0.211	0.195
Bunny	Ears Tearing	0.084	0.053	0.052

Weighted means based on the combination of the Hessian responses and the Shepards's IDW gives the best result in terms of accuracy. The Shepards's IDW gives results almost similar to this combination in some cases.

We further test the Cbf on real data. Figure 4.10 illustrates results from our non-rigid tracking on a deformed cube (initial situation, intermediate configuration and final configuration). From a qualitative standpoint, the results of the final configuration exhibit a good correlation between the reference mesh and the tracked one.

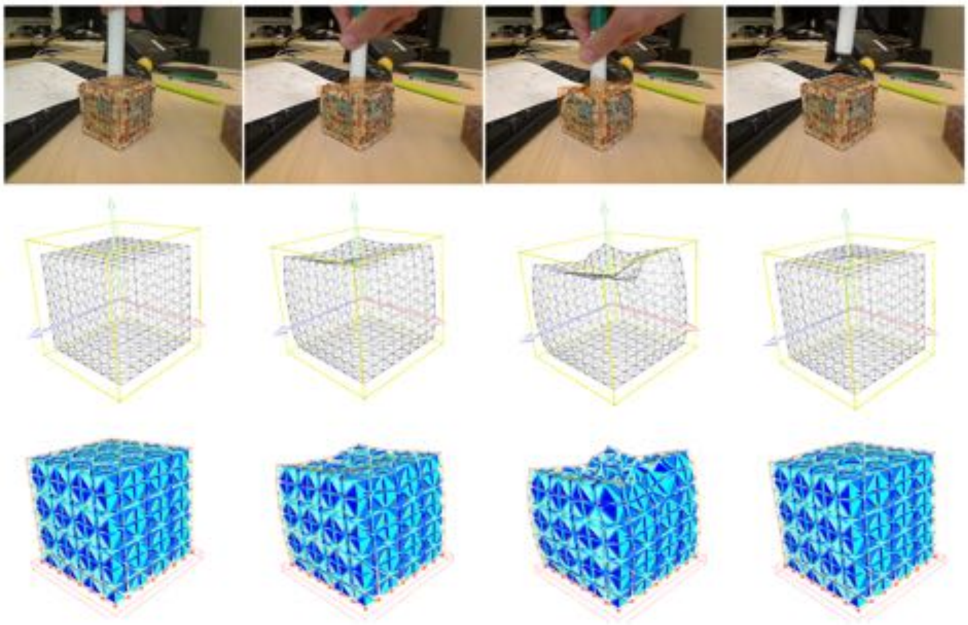

Figure 4.10: A sequence of images showing a cube being deformed. (Top) augmented reality images where the mesh in wireframe is superimposed on the video stream, (Middle) the deformed mesh, (Bottom) the volumetric mesh composed of tetrahedra.

4.4 Liver Biomechanical Model

In this section we provide a description of the biomechanical model used to compute the deformations of the liver. Before giving details of the tetrahedral model employed for parenchyma, we give and overview of the existing models for the real-time simulation of liver soft-tissue, we then focus on the model of vascularization and mechanical coupling between those two. Since the final composite model is heterogeneous and anisotropic due to the vascular structures, we finally describe the solution process based on a direct solver, still allowing real-time performance.

4.4.1 Parenchyma Model

In order to correctly translate the parenchyma tissue behaviour, two properties must be taken into account: non-linearity of the organ tissue and its viscoelasticity. These two features are reported in most biomechanical studies concerning the constitutive models of the liver parenchyma (see Kerdok et al. (2006) or Gao et al. (2009) for instance) and have been numerically modelled by the computer graphics community. From a usability point of view, an additional characteristic must be considered : the real-time achievement. This property is decisive in the choice of an appropriate biomechanical model.

Even though linear models yield fast and stable simulations, they are not suitable for large deformations. On the other hand, by using Green's non-linear strain tensor, more realistic deformations can be performed, but with more costly simulation and complex numerical problems.

In this study, we aim at modeling large deformations correctly in real-time, since during surgical interventions, important displacements of tissue (e.g. the liver lobes) occur due to the action of surgical tools. On the other hand, we do not focus on the transient part of the deformation but rather the static equilibrium under some specific loading conditions, we do not take into account the viscous properties of the tissue.

For this reason we have opted for a finite element method based on a *co-rotational* formulation which allows large displacements while relying on a linear expression of the stress-strain relationship.

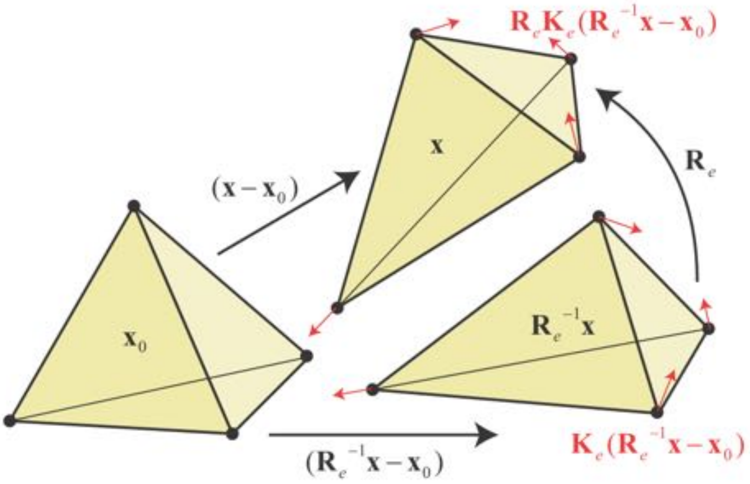

Figure 4.11: To compute the elastic forces acting at the vertices of a tetrahedron, its deformed coordinates x are rotated back to an unrotated frame $\mathbf{R}_e^{-1}\mathbf{x}$. There, the displacements $\mathbf{R}_e^{-1}\mathbf{x}-\mathbf{x}^0$ are multiplied by the stiffness matrix yielding the forces $\mathbf{K}_e(\mathbf{R}_e^{-1}\mathbf{x}-\mathbf{x}^0)$ that are finally rotated back to the frame of the deformed tetrahedron by multiplying them by $\mathbf{R}_e$. From Müller and Gross (2004).

Corotational Model The co-rotational model is a very popular method in computer graphics and medical simulation introduced by Felippa in Felippa and Haugen (2005). This method is based on the decomposition of the actual element configuration into rotational and deformational components, both being quantified w. r. t. the initial position. More precisely, the actual position of the element nodes determines the base of the element (given by three chosen adjacent edges), which are both rotated and deformed w. r. t. the initial base of the same element (see Figure 4.11). This can be achieved in different ways, such as polar decomposition (Müller and Gross (2004)) or through geometrical analysis (Nesme et al. (2005)).

The linear equation $\mathbf{f}_e = \mathbf{K}_e\mathbf{u}_e$ that relates the force/displacement relationship for an element e connecting n_e nodes is then replaced by

$$\mathbf{f_e} = \mathbf{R_e K_e R_e^T}(\mathbf{x} - \mathbf{x_0}) \tag{4.20}$$

$\mathbf{R_e}$ is a matrix that contains n 3×3 identical rotation matrices along its diagonal (n is the number of nodes in the element). The vector $\mathbf{x}$ contains the actual positions of the nodes of the element while $\mathbf{x_0}$ contains their rest positions.

In our method we employ the technique described in Nesme et al. (2005) in order to extract the rotational component (denoted as $\mathbf{R}_e$). The matrix $\mathbf{R_e}$ is used to update the local stiffness matrix $\mathbf{K_e}$ of the element. Therefore, via these element-wise rotations, the actual global stiffness matrix $\mathbf{K}$ depends in each step on the actual deformation $\mathbf{u}$ and the equation relating the external forces to the displacements can be written as:

$$\mathbf{f} = \mathbf{K}(\mathbf{u})\mathbf{u} \text{ with } \mathbf{u} = \mathbf{x} - \mathbf{x}^0 \tag{4.21}$$

where $\mathbf{x}_0$ and $\mathbf{x}$ represent nodal positions in rest and actual positions, respectively, and $\mathbf{f}$ are the external forces.

Assuming that linear tetrahedral P1 elements are employed in the finite element formulation of the parenchyma model and the mesh is composed of $N_{\mathbb{P}}$ nodes, the resulting system has $3N_{\mathbb{P}}$ degrees of freedom, i. e. $\mathbf{u}_{\mathbb{P}}$, $\mathbf{f}_{\mathbb{P}}$ are vectors of the size $3N_{\mathbb{P}}$ whereas $\mathbf{K}_{\mathbb{P}}$ is a $3N_{\mathbb{P}} \times 3N_{\mathbb{P}}$ matrix, where the subscript $\mathbb{P}$ denotes the parenchyma.

Such a technique overcomes some of the limitations of linearly elastic models, without compromising too much the computational efficiency and has been successfully used for real-time simulation of liver tissue Saupin et al. (2008); Courtecuisse et al. (2012).

4.4.2 Vessel model

The vascular system is considered as the main source of heterogeneity which has a global influence on the mechanical response of the vascularized tissue due to important stiffness of the vessel wall. The model employed here is based on work presented in Peterlík et al. (2012). Besides describing the model in the actual scenario, additional details concerning the assembling of the composite system are given in the following text. Is should be emphasized that a potential viscoelastic response due to fluids (i. e. blood) circulating in the vessels is not taken into account.

From the mechanical point of view, the vascular system is modeled with serially linked beam elements in a similar way as proposed by Duriez et al. (2006)

for simulating catheters and guide wires (validated experimentally in Dequidt et al. (2008) by studying the coil rest shape under deformation). This method, based on three-dimensional beam theory Przemieniecki (1985) permits to handle geometric non-linearities while maintaining real-time computation thanks to using a substructures-based optimization (each substructure can be constituted of one or several beam elements, and is analyzed independently).

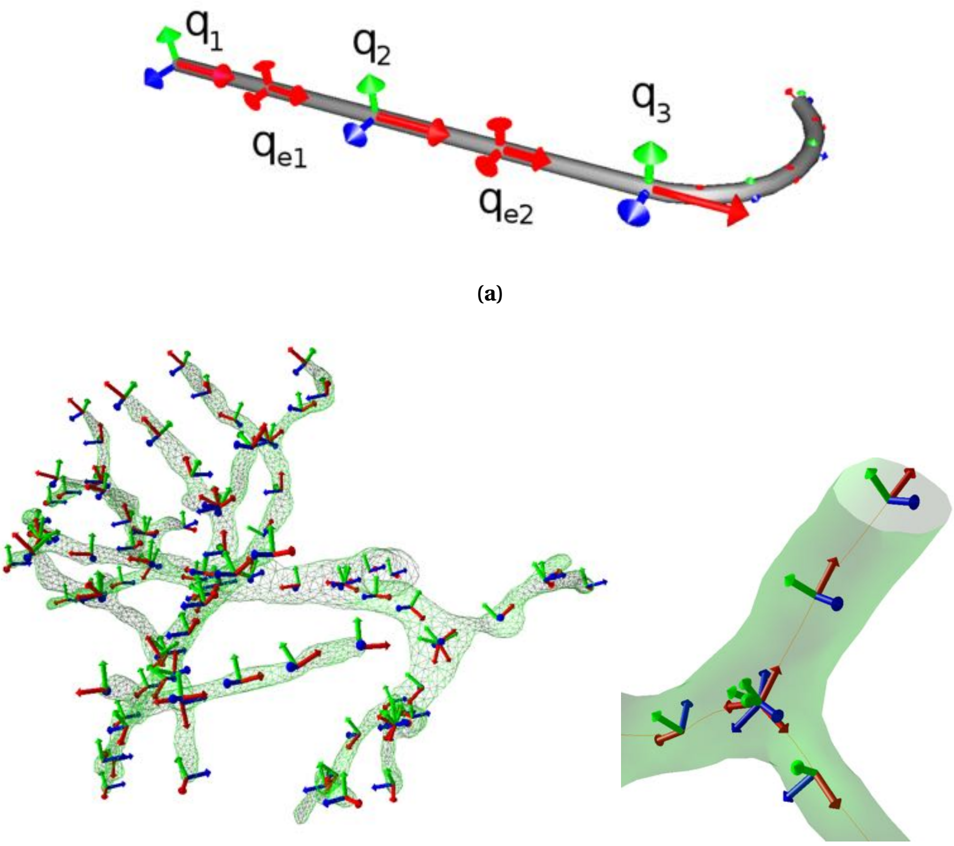

(a)

(b) **(c)**

Figure 4.12: Vascular Network model. (a) Catheter with the beam model in its curved rest shape: with the tricolor nodal frames; and the red frames matching the middle of each beam. (b) Beams generated along the vessels mesh. (c) a zoom into (b) showing a bifurcation where beams are superimposed.

Each beam element is delimited by two nodes that have 6 degrees of freedom (DOF): 3 angular $\mathbf{q_r}$ and 3 spatial positions $\mathbf{q_t}$. The beam element includes a 12×12 symmetric stiffness matrix $\mathbf{K_e}$ that relates the nodal degrees of freedom of a beam element to the forces and torques applied to them. The final internal forces $\mathbf{f_i}$ generated by the deformation of the structure at one node i are:

$$\mathbf{f_i} = \sum_{\mathbf{e=i-1}}^{\mathbf{i}} \mathbf{R_e}(\mathbf{q})\mathbf{K_e}(\mathbf{R_e}(\mathbf{q})^{\mathrm{T}}(\mathbf{q}-\mathbf{q_e}) - \mathbf{p_{rest}}) \tag{4.22}$$

where e is the index of the two beams connected to this i^{th} node. $\mathbf{q_{i-1}}$, $\mathbf{q_i}$ and $\mathbf{q_{i+1}}$ are the vectors of the 6 DOF positions of the three nodes (respectively $i-1$, i, $i+1$) and belong to the two beams in the global frame (quaternions are used for rotations). The tricolor frames in Figure 5.1, illustrate these nodal frames. $\mathbf{q_{ej}}$ denotes the middle frame of the j^{th} beam (red frames) that is computed as an intermediate 6 DOF positions between the two nodes of the beam where $\mathbf{p_{rest}}$ corresponds to the 6 DOF rest positions of these nodes in the local frame.

This model shares some similarities with the co-rotational model described above, and in particular geometrically non-linear deformations. At the same time it accounts for rotational degrees of freedom, i. e. besides linear positions and forces, orientation and torques are included in the mechanical formulation. However, we introduce some modifications to the model to take into account the particular nature of vessels, in particular through specific cross section profiles and moments of inertia Przemieniecki (1985).

The static formulation for the deformation of a beam is described by a system similar to Eq. 4.21 with constituents $\mathbf{u}_{\mathbb{V}}$, $\mathbf{f}_{\mathbb{V}}$ and $\mathbf{K}_{\mathbb{V}}$. However, as each node is equipped with 6 degrees of freedom due to the rotational components, the size of vectors $\mathbf{u}_{\mathbb{V}}$ and $\mathbf{f}_{\mathbb{V}}$ is $6N_{\mathbb{V}}$ and $\mathbf{K}_{\mathbb{V}}$ is a $6N_{\mathbb{V}} \times 6N_{\mathbb{V}}$ matrix where $N_{\mathbb{V}}$ is the size of the beam mesh representing the geometry of vessels.

It is worth mentioning that other techniques exist in the literature for modeling wire-like structures such as Super-Helix model Bertails et al. (2006) or angular springs model Wang et al. (2007). These models are however more complex or do not faithfully reproduce the physical vessels behaviour.

4.4.3 Mapping of tumors and parenchyma

The size of tumors being relatively small comparing with the whole parenchyma, we assume that its influence on the overall mechanical behaviour is negligeable and therefore the coupling with parenchyma can be only geometric. However, a purely geometric mapping may deform the shape of the tumor which may cause erroneous measurements. For this reason the tumor is modelled as a real mechanical object with a very stiff Young's Modulus. This modellng does not affect the performance of the simulation and permits a conservation of the shape of the tumor while allowing correct in-depth propagation of the deformation. With the same formulation as the parenchyma (co-rotational model), coupling between tumors and parenchyma is done following Faure et al. (2012).

Let γ be the function used to map the positions $\mathbf{x}_p$ of the parenchyma model to the positions $\mathbf{x}_t$ of the tumor model. The positions are mapped following:

$$\mathbf{x}_t = \gamma(\mathbf{x}_p) \tag{4.23}$$

where the velocities are mapped such as:

$$\mathbf{v}_t = \mathbf{J}\mathbf{v}_p \tag{4.24}$$

where $\mathbf{J} = \frac{\partial \mathbf{x}_t}{\partial \mathbf{x}_p}$ is the Jacobian matrix that encodes the linear relation between the parenchyma and the tumors velocities. Accelerations can be mapped using:

$$\mathbf{a}_t = \mathbf{J}\mathbf{a}_p + \frac{\partial \mathbf{J}}{\partial \mathbf{x}_p}\mathbf{v}_p \tag{4.25}$$

In our case, the operators γ and $\mathbf{J}$ are the same, since we consider that γ is linear with respect to $\mathbf{x}_p$. The matrix $\mathbf{J}$ contains barycentric coordinates of the degrees of freedom of the tumors w. r. t.to the corresponding parenchyma element (in our case linear P1 tetrahedral element).

The stress/strain relation related to the material law of the elastic model implies that each displacement generated forces. The propagation of the positions and velocities are from the parenchyma to the tumors. The forces are propagated conversely, from the tumors to the parenchymas' degrees of freedom where Newton's law is applied. Given forces $\mathbf{f}_t$ applied to tumors model, the mapping computes and accumulates the equivalent forces $\mathbf{f}_p$ applied to its master. Since equivalent forces must have the same power, the following relation holds:

$$\mathbf{v}_p^{\mathsf{T}}\mathbf{f}_p = \mathbf{v}_t^{\mathsf{T}}\mathbf{f}_t \tag{4.26}$$

Given the relation of Equation 4.24 and using the virtual work principle, the previous relation can finally be expressed as:

$$\mathbf{f}_p = \mathbf{J}^{\mathsf{T}}\mathbf{f}_t \tag{4.27}$$

It is important to recall that only the liver surface deformation is estimated using our visual tracking method, thereby, the deformation of the parachyma is driven by loads acting solely on its surface. The mapping relations permit to propagate this deformation to the tumors where we can estimate their positions over time. Several tumors can be mapped where each tumor accumulates its contribution to the forces on the parenchyma using its mapping.

4.4.4 Coupling between vessel and parenchyma

In order to build the composite model of vascularized tissue, we adopt the method proposed in Peterlík et al. (2012). At the beginning of the time step, the forces applied in the beam points are propagated to the vertices of tetrahedra. Then, stiffness matrices for both beams and tetrahedral models are assembled and combined together as described below. The composite system is solved resulting in displacements of the tetrahedral vertices (see Figure 4.13). Finally, the

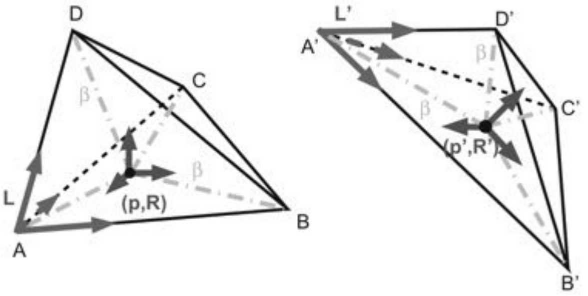

Figure 4.13: Mapping between 6DoF beam node and tetrahedron in initial and rotated positions. The positions of beam and tetrahedron nodes do not coincide.

positions of beam nodes are updated based on actual positions of tetrahedra. For the sake of simplicity, we first describe the positional mapping between the nodes, then the propagation of forces and finally, we show how the stiffness matrices combined together to get the global stiffness matrix of the composite system.

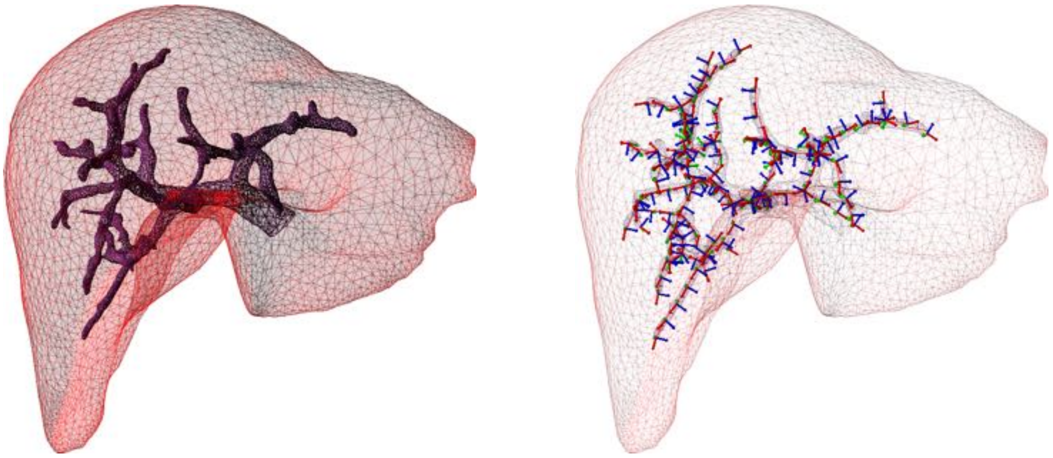

(a) **(b)**

Figure 4.14: 3D heterogeneous biomechanical model of the liver with : (a) heterogenous liver including the vascular network in wireframe, in (b) beams generated along the vessels.

Let us first focus on positional mapping of an arbitrary beam point of the vessel network. We recall that the point is defined by its position $\mathbf{p}$ and orientation $\mathbf{O}$ in space. Before the simulation starts, the point is associated with a tetrahedron T so that it is located inside T. Two quantities are precomputed for the point: the barycentric coordinates of $\mathbf{p}$ w. r. t. the tetrahedron T (denoted as $\boldsymbol{\beta}_T$) and orientation $\mathbf{O}_T$ of the point formulated relatively with respect to the tetrahedron T, computed as

$$\mathbf{O}_T = \mathbf{B}_T^{-1}\mathbf{O} \tag{4.28}$$

where $\mathbf{B}_T$ is an orthogonal base given by the edges connecting the nodes of the tetrahedron T in the rest position. It should be noted that the same matrix is required by the co-rotational model. Since it is supposed that no relative motion between the parenchyma and vessels occurs, both $\boldsymbol{\beta}_T$ and $\mathbf{O}_T$ remain constant during the simulation and in each step they are used to calculate the updated position $\mathbf{p}$ and orientation $\mathbf{O}$ of the beam point in space. As for the position, the calculation using barycentric coordinates is straightforward. The updated orientation $\mathbf{O}'$ is computed as

$$\mathbf{O}' = \mathbf{B}'_T \mathbf{O}_T \tag{4.29}$$

where $\mathbf{B}'_T$ is the base given by updated positions of the tetrahedron T. The calculation of the updated base $\mathbf{B}'_T$ requires the orthogonalization process. However, this computation is already needed by the co-rotation model, so the mapping does not introduce an additional significant computational cost.

In the same time step, the response forces applied in the beam node are mapped onto the vertices of the associated tetrahedron T. For the beam point, there are linear forces $\mathbf{f}$ as well as torques $\boldsymbol{\tau}$, whereas for the tetrahedron, only linear forces $\mathbf{F}$ are modelled in the element vertices. The linear response force $\mathbf{f}$ is mapped from the beam point to its corresponding tetrahedron T using barycentric coordinates $\boldsymbol{\beta}_T$ introduced above. The torques $\boldsymbol{\tau}$ are transformed to linear forces acting in the tetrahedron nodes using the equation $\tau = \mathbf{r} \times \mathbf{F}$ where $\mathbf{r}$ is the vector connecting the beam and tetrahedron nodes. Putting it together, the force contribution of the beam point is added to the forces applied in the vertices of associated tetrahedron T as

$$\mathbf{F}_i = \mathbf{F}_i + \beta_i \mathbf{f} - (\mathbf{r}_i \times \boldsymbol{\tau}) \tag{4.30}$$

where i runs over the vertices of T.

As introduced above, the vascularized tissue is a composite deformable object, where the total stiffness matrix $\mathbf{K}$ is composed of contributions provided by stiffness of parenchyma $\mathbf{K}_{\mathbb{P}}$ and stiffness of vessel walls $\mathbf{K}_{\mathbb{V}}$. Let us suppose that the mapping between the beam and tetrahedra nodes can be expressed in a matrix form as $\mathbf{f}_{\mathbb{P}} = \mathbf{J}^T \mathbf{f}_{\mathbb{V}}$ where $\mathbf{J}$ is a $3N_{\mathbb{P}} \times 6N_{\mathbb{V}}$ Jacobian matrix of the mapping between the nodes of parenchyma and the vessels Faure et al. (2012). The global stiffness $\mathbf{K}$ matrix is then computed as

$$\mathbf{K} = \mathbf{K}_{\mathbb{P}} + \mathbf{J}^{\top} \mathbf{K}_{\mathbb{V}} \mathbf{J} \tag{4.31}$$

4.5 Non-rigid Registration

Non-rigid registration consists of a 3D point-to-point registration that links the image-based 3D features representing the liver motion to the degrees of freedom of the liver physical model. Registration is done at each frame captured by the endoscopic camera in order to correctly pilot the mechanical model, and thus to estimate the correct position of the underlying tumors.

4.5.1 Initial State

Initialization is the alignment of the 3D mesh (with the underlying physical model) on the laparoscopic image at $t = 0$. This step is critical and special care must be taken during this phase since it can significantly impact the estimated position of the tumor given the deformations that organs undergo during surgery. In addition, since gas is insufflated (pneumoperitoneum) to increase the working space Bano et al. (2012), the preoperative data may no longer correspond to the intraoperative image.

The initial alignment is an ill-posed problem where we aim at registering two sets of 3D points without knowing the matching between these two sets. Due to this complexity and despite the numerous AR techniques in surgery, very few works have investigated the initial alignment between laparoscopic images and the three-dimensional model. Clements and et al. (2008) introduced an ICP-based approach to aid in the initial pose estimation. Using salient anatomical features, identifiable in both preoperative images and intraoperative liver surface data, this method is able to reach a reasonable solution, but is restrained to rigid transformations. Another intraoperative registration method is presented in Dagon et al. (2008). The authors used an intraoperative ultrasound probe to register the vessel tree on a 3D liver model. However, since our aim is to register laparoscopic data recorded by a camera, such information is not available. Recently, Oktay et al. (2013) proposed a method that combines pneumoperitmoneum simulation and CT-scan imaging. By considering the intraoperative data acquired from CT-scans (after gas insufflation) as an additional constraint to drive the simulation, this method provides accurate registration. Nevertheless, it relies on intraoperative scans which are not considered in the operating room.

Currently, no technique is mature enough to permit an automatic initial alignment, and this issue remains a challenge to be solved by the scientific community. This is why, we rely on a manual initial alignment to reduce errors that may emanate from a bad initialization. As in related works Su et al. (2009)Puerto-Souza and Mariottini (2013) the initialization is done manually through a Graphical User Interface (GUI). Nevertheless, preliminary tests on non-rigid alignment using anatomical landmarks and atlas-based model show the potential of these approaches for initial alignment Plantefeve et al. (2014).

Alignment of virtual and real camera

Assuming a calibrated endoscopic camera, the matrix **A** of the intrinsic parameters is defined as follows:

$$\mathbf{A} = \begin{bmatrix} f_x & 0 & c_x \\ 0 & f_y & c_y \\ 0 & 0 & 1 \end{bmatrix} \tag{4.32}$$

where f_x and f_y are the focal lengths, c_x and c_y the principal point. The first step to ensure visual consistency, is to load these intrinsic parameters on the GUI virtual camera.

Model alignment

3D surface reconstruction is built on the first pair of laparoscopic images (the first pair is chosen so that a large part of the liver is visible) using the MLS surface approximation. The liver mesh is then aligned manually to the reconstructed surface, based on salient geometrical landmarks such as liver contours or surrounded ligaments. This alignment consists of finding the matrix $[\mathbf{R}|\mathbf{t}]$ of rotation and translation that permits a correct visual alignment of the mesh and the surface (cf. Fig. 4.15).

This rigid transformation is insufficient to correctly initialise the registration. Indeed, due to gas insufflation, pre-operative data (liver mesh computed for CT-scans) geometrically differs form intra-operative data (reconstructed patch) Sanchez-Margallo et al. (2011). To solve this issue, we constrain the biomechanical model (including the vessels and the tumour) with external forces so that it better fits the visible liver surface recovered.

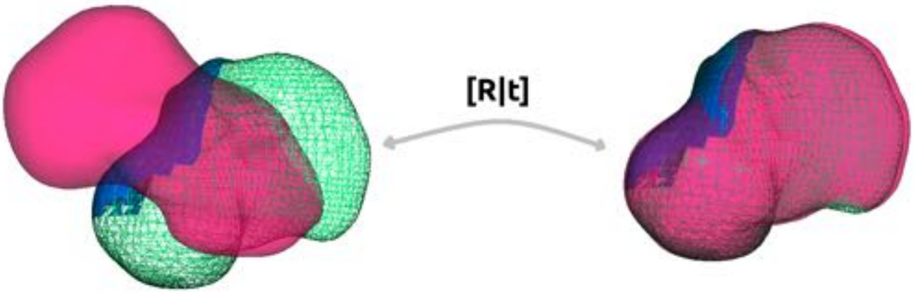

Figure 4.15: Initial model alignment (simulated data): The mesh in purple represent the 3D model computed from CT scans in a different reference, the mesh in blue represents the MLS surface reconstructed from laparoscopic image pair. It represents around 30% of the whole liver that is represented in green.

Point correspondence

The temporal non-rigid registration is a point-to-point registration (cf. Fig. 4.16), therefore, the set of three-dimensional points $\mathbf{y}$ are projected onto the liver model surface using a ray casting method Roth (1982).

Ray-casting is a well-established technique widely used in computer graphics for visual rendering. The algorithm is based on ray-surface intersection test by projecting a set of points from a defined origin (for instance the camera location) to a targeted mesh surface (for instance the liver mesh). Its advantage in our case is twofold: it permits to directly correspond the set of points $\mathbf{y}$ to the degrees of freedom of the mechanical model, in addition, it allows to avoid the features that do not belong to the liver but to the surrounding tissues since only the 3D points that intersect the liver surface after ray-casting are kept, the features that do not belong to the liver are filtered out from laparoscopic images.

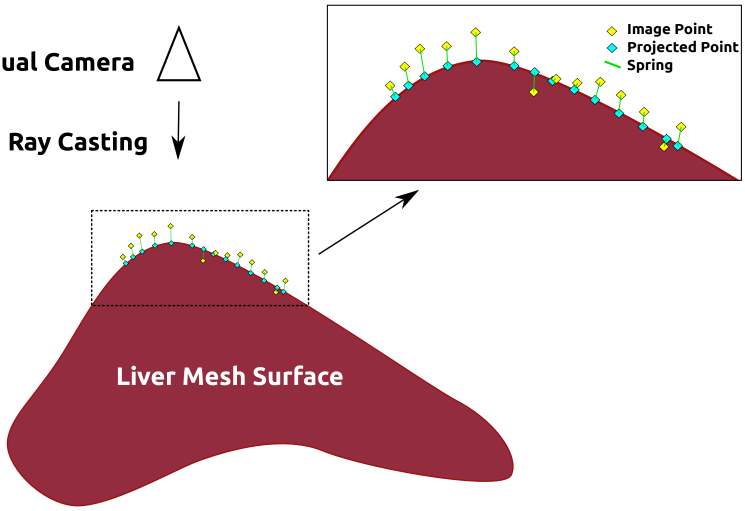

Figure 4.16: Point-to-point registration: The initial set of control points $mathbfy$ is projected on the surface using ray-casting to pair the set $mathbfy$ with the degrees of freedom of the mechanical model $mathbfx$ at $t = 0$.

Boundary conditions

Boundary conditions are defined by fixing a set of degrees of freedom of the biomechanical model that represents the falciform ligament and the underlying fat (see Figure 4.17). Recent studies focused on the importance of modeling the ligament Bosman et al. (2014). Indeed, boundary conditions can be modelled as springs, linear FEM model or considered as fixed vertices of the volumetric mesh. The latter method is used in our work. This amounts to substitute in the stiffness matrix $\mathbf{K}$ the couple row/column of the index of the fixed point by zero.

This point will not influence and will not be influenced by other points in the mesh.

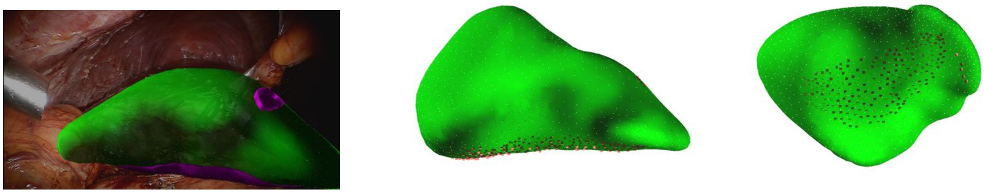

Figure 4.17: Boundary conditions: The liver model (in green) is constrained by fixed vertices (in purple) that represent the falciform ligament and the underlying fat.

4.5.2 Stretching Energy Minimization

Non-rigid registration can be seen as a stretching energy minimization between the three dimensional features recovered from laparoscopic images that represent the tracking energy W_{ext} and the biomechanical model derived from preoperative CT data. We consider an energy that accounts for the internal energy of the biomechanical model W_{int} and the tracking energy W_{ext}.

We aim at simulating the liver elasticity at each frame under certain loads without dealing with the dynamic part of the deformation but rather the static equilibrium of the mechanical core. In addition, the blood flow is not considered in the vascular network model. Thus, we consider a quasi-static scenario, i. e. the actual shape of a deformable object under applied forces is computed using finite element formulation without dealing with tissue transient properties.

The core mechanical equations based on Newton's second law is given by a non-linear ordinary differential equations system that can be written as follows:

$$\mathbf{Ma} = \mathbf{F}_{\text{ext}} - \mathbf{F}_{\text{int}} \tag{4.33}$$

where $\mathbf{a}$ is the acceleration and $\mathbf{M}$ the mass matrix. The forces $\mathbf{F}_{\text{ext}}$ are the external forces acting on the model and $\mathbf{F}_{\text{int}}$ the internal forces of the material. The quasi-static case implies that the acceleration $\mathbf{a}$ is zero, thus we obtain:

$$\mathbf{F}_{\text{int}} = \mathbf{F}_{\text{ext}} \tag{4.34}$$

This system of equations consists of deriving the external and internal energies, W_{ext} and W_{int} respectively. The aim is to reach an extremum (minimum) where the internal forces equal the tracking forces $W_{\text{int}} = W_{\text{ext}}$.

Internal Forces

Using the co-rotational formulation described above the internal forces are expressed as:

$$\mathbf{f_i}(\mathbf{x}) = \mathbf{R_e}\mathbf{K}(\mathbf{R_e}^\top\mathbf{x} - \mathbf{x^0}) \tag{4.35}$$

where **K** represents the stiffness matrix, $\mathbf{R_e}$ the co-rotational matrix and $\mathbf{x}, \mathbf{x^0}$ are vectors of size $3n$ representing the position of the n degrees of freedom of the mechanical model, respectively at any time t and time $t = 0$.

External Forces

External forces are defined by pairing the m 3D points **y** to the n degrees of freedom **x** of the bio-mechanical model. The tracked control points $\mathbf{y^0}$ at initialization $(t = 0)$ are expressed in barycentric coordinates of the adjacent degrees of freedom leading to the linear relation:

$$\mathbf{y^0} = \mathbf{L}\mathbf{x^0} \tag{4.36}$$

where **L** is a rectangular matrix $(3m, 3n)$. We assume this linear relation remains valid during the deformation.

At any later time t, the stretching forces induced by the tracking of control points are defined as

$$\mathbf{f_t}(\mathbf{y}) = k(\mathbf{y} - \mathbf{y^0}) \tag{4.37}$$

where k can be seen as stiffness. Finally, the stretching forces can be expressed with respect to the degrees of freedom as

$$\mathbf{f_t}(\mathbf{x}) = \mathbf{L}^\top\mathbf{f_t}(\mathbf{y}) \tag{4.38}$$

$$\mathbf{f_t}(\mathbf{x}) = \mathbf{L}^\top k\mathbf{L}(\mathbf{x} - \mathbf{x^0}) \tag{4.39}$$

Parameter k is set to be at the same order of magnitude as the Young's modulus to insure that the simulation remains stable even at large integration steps.

4.5.3 Resolution

Considering a quasi-static scenario, we aim at solving the linear system given by Eq. 4.21 at each step of the simulation. A wide range of direct and iterative solvers have been proposed in the past to solve such a system of equations emerging in physics-based modeling of deformable bodies. In case of homogeneous systems in which the finite element formulation results in well-conditioned matrices, iterative solvers have proven to be efficient techniques converging rapidly to the optimal solution. However, in our case, the final matrix **K** gathers mechanical contributions of both parenchyma and vessel walls. As the experiments report a significant difference in stiffness of these two components (e. g. see Umale et al.

(2011)), the composite system results in a poorly conditioned matrix. In this case the convergence of iterative solvers becomes an important issue. Thus, we rely here on direct methods.

Direct methods aim to calculate with an exact way the inverse of the system matrix (or a factorization) that permits to obtain the solution in a finite number of operations. These methods are considered robust as they are relatively insensitive to numerical problems such as ill-conditioned systems or imprecisions. One can explicitly calculate the exact inverse matrix $\mathbf{A}^{-1}$ in order to directly solve the system such as $\mathbf{x} = \mathbf{A}^{-1}\mathbf{b}$. In some cases, for example where the matrix **A** is diagonal, this computation can be very effective and trivial and real-time can be considered. However, in general cases, the computation of $\mathbf{A}^{-1}$ can be very costly and complex. In addition, the storage of $\mathbf{A}^{-1}$ can be a limitation since it becomes a dense matrix. For this purpose, condensation techniques have been proposed Bro-nielsen and Cotin (1996) considering static and quasi-static cases. These techniques aim at reducing the number of degrees of freedom so that the computation of the inverse can be achieved in real-time.

In order to exploit the sparse matrix that produces the mechanical system, a factorization method can be considered. The factorization expresses the matrix **A** as a product of simple matrices. For example, any invertible matrix can be expressed as the product of a lower triangular matrix and an upper triangular matrix $\mathbf{A} = \mathbf{LU}$. This is called **LU** decomposition where **LU** stands for Lower Upper. This decomposition results in a system with two linear equations composed with triangular matrices, which can be efficiently solved. However, the factorization may fail to materialize without a correct ordering or permutations in the matrix. Thereby, a permutation matrix P is usually used resulting in the factorization of $P\mathbf{A}P^{-1}$ instead of **A**. This permutation is sufficient for the **LU** factorization, but is however time consuming without considering optimized computation algorithms [Toledo (2003)].

For efficient numerical solutions, other factorization methods can be considered. For example Cholesky factorization, of the form $\mathbf{LL}^{\intercal}$, is based on the decomposition into the product of a lower triangular matrix and its conjugate transpose, and can be applied only on positive-definite symmetric matrix. It is more efficient than **LU** decomposition Trefethen and Bau (1997), but is nevertheless sensitive to numerical instabilities since it is based on the extraction of square roots. To avoid this issue, a closely related variant of the classical Cholesky decomposition can be used: **LDL** decomposition. Of the form $\mathbf{LDL}^{\intercal}$, it calculates separately the inverse of the diagonal matrix **D** with avoiding the extraction of square roots. For this reason, we rely on direct $\mathbf{LDL}^{\intercal}$ solver for the resolution of our system. Although the solver imposes stricter limitations on the size of the system being resolved, it still provides a stable real-time solution applicable to the problems considered in our work.

4.6 Conclusion

The method presented here addresses several important limitations that currently hinder the use of augmented reality in clinical routine of minimally invasive procedures. We particularly focused on the three-dimensional localization and visualization of internal structures, such as blood vessels and tumors. To this end, we have developed an image-guided biomechanical model that is able to capture complex deformations underwent by the liver during surgery. The deformation model is guided by both internal forces (associated to a biomechanically validated model of the liver) and external forces related to three-dimensional points (reconstructed from stereo images). Such characteristics make our model able to capture both the organ surface and inner structures motion while being parameterized with textbook Young's modulus and Poisson's ratio values.

In the next chapter, we present the results obtained through *in vivo* qualitative assessment on a human liver and quantitative validation on a phantom liver where errors well below the current surgical margins are measured. In addition, we present further strategies to reduce these errors.

CHAPTER 5

EXPERIMENTATION

Contents

5.1 Introduction

In laparoscopic surgery, validation remains very challenging. In our case, this problem is more complex since neither qualitative results nor visual assessment can validate the deformation of internal structures that are not visible in laparoscopic images. In order to assess the performance of our approach, we confront in this chapter our framework against three experimental scenarios. First, we demonstrate with computer-generated data whether and where an heterogeneous model differs from an homogeneous one for the prediction of tumor location. Second, our approach is tested on an actual laparoscopic procedure performed on a human liver, allowing us to qualitatively estimate how our approach could perform in a real surgical environment. Third, we rely on a realistic phantom liver to quantitatively measure the error between simulation and ground truth.

We further propose several strategies to add robustness to visual tracking, and we discuss the importance of the material stiffness in the modeling of liver paranchyma.

5.2 Pre-operative Data Acquisition

The used pre-operative data consist of a set of CT-scans pre-operatively performed on patients. We exploit these data to build anatomical model of the liver which consists of the parenchyma, the tumors and the vascular network. The liver model is built following three steps: segmentation and mesh generation, volumetric model generation (capable of computing FEM) and tissue parametrization.

5.2.1 Segmentation:

Although this thesis does not address the challenging task of surface reconstruction, a good surface representation is very important for physical simulation operations. We use segmentation technique to generate liver surface together with tumors surface from the volumetric CT images. Segmentation is done semi-manually using active contour technique (Snakes) Kass et al. (1988b) available in the software *itksnap* Yushkevich et al. (2006). Usually, a mesh-smoothing step is required after segmentation to reduce the number of triangles and obtain a suitable mesh for volumetric mesh generation.

Vessels are more difficult to segment than the parenchyma, considering their small diameter and their proximity to each others. For this reason, a contrast enhancement is needed before segmentation to easily detect salient edges.

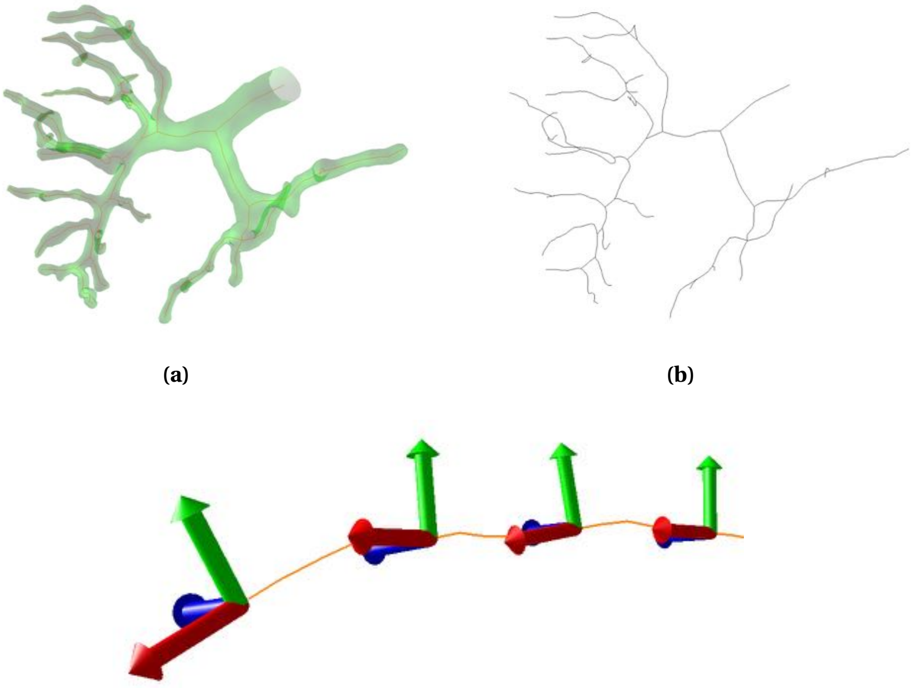

(a) (b)

(c)

Figure 5.1: Vessel model with (a) and (b) the central lines extracted using Dijkstra algorithm and (c) the beams generated along the central lines.

5.2.2 Volumetric mesh generation:

Volumetric meshes are necessary for a finite element modeling. Thus, from the previously generated surface we build a volume representation of the liver composed of linear P1 tetrahedral elements, using 3D Delaunay triangulation algorithm which is available in *CGal* library [CGA]. The number and type of elements are to be chosen carefully in order to ensure real-time performance as well as sufficient accuracy (see Figure 5.2).

This technique is well suited for representing liver and tumors volume, however, it is not appropriate for vascular network. Indeed, the shape and thickness of the vessels make it difficult to create a correct volumetric representation. Moreover, since the vessels model used in our composite model is a wire-like model, central lines of the vessels are needed to build the beam model (see figure 5.2). We used the method described in Verscheure et al. (2013) to extract these central lines. This approach implements an iterative Dijkstra minimum cost spanning tree to extract the vessels skeleton. Having the vessels skeleton, beams are generated along the central lines to obtain the final vascular network model by choosing the thickness of the vessel wall (for instance $t_{\mathbb{V}}=200$) and the spacing between the beams (deduced from the number of beams, for instance 120 beam elements).

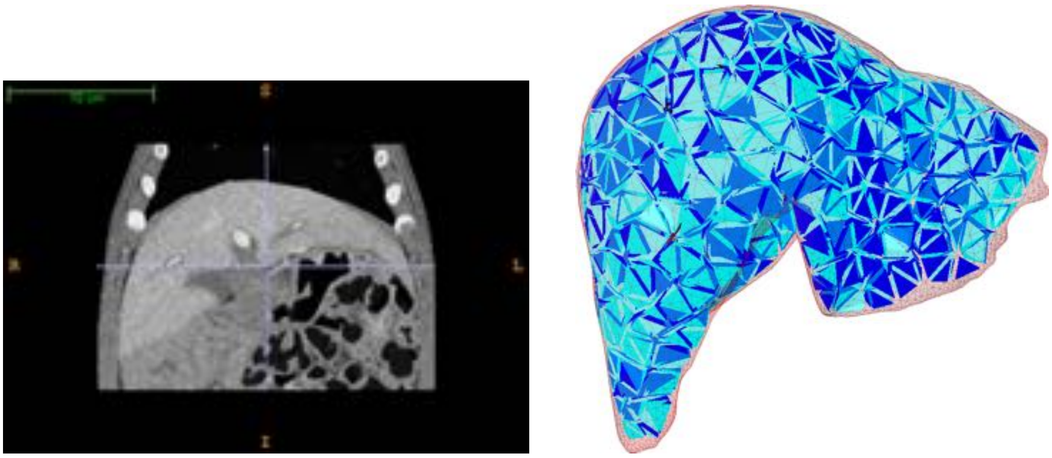
(a) (b)

Figure 5.2: Liver segmentation: (a) one image from CT scanning, (b) volumetric representation of the liver (in blue) computed from its surfacic representation (in wireframe).

5.2.3 Tissue Parametrisation:

Several studies have measured the characteristics of liver soft-tissue Kerdok (2006), using different measurement devices on living and non-living tissues. In this study, the used elastic parameters are summarized in table 5.1 and are set according to Yamada (1970); Umale et al. (2011); Peterlík et al. (2012).

	Parenchyma	**Vascular Network**
Young's Modulus	$E_{\mathbb{P}}$=27 kPa	$E_{\mathbb{V}}$=0.62 MPa
Poisson's Ratio	$\nu_{\mathbb{P}}$=0.45	$\nu_{\mathbb{V}}$=0.45
Resolution	3391 tetrahedral (P1) elements	120 beam elements

Table 5.1: Liver tissue parametrisation and resolution.

5.3 Experiments with computer-generated data

We evaluate the impact on registration, of using a heterogeneous model instead of a homogeneous model (which can be seen as providing similar results as an advanced geometric approach). This is done by calculating the Euclidean distance between the estimated tumor location in the cases of homogeneous and heterogeneous deformations (see 5.2). We also measure this influence depending on the location of the tumor in the liver, at three different locations: 1) close to the point of interaction in order to quantify local deformation, 2) away from the point of interaction to quantify global behaviour, and 3) in the middle of the vascular network to assess its influence. The simulations are generated using SOFA framework Allard et al. (2007).

The results illustrated in figure 5.3 show that taking into account the vascular network impacts the tumor location. We can notice a difference in the distance of about 15 mm in the case where the tumor is located close to the deformation. We also notice that even if the tumor is located far from the point of interaction, it remains influenced by the vascular network with a distance of more than 3 mm. However, when the tumor is very close to the boundary conditions, the impact of the vascular network is considerably reduced, which is an expected result.

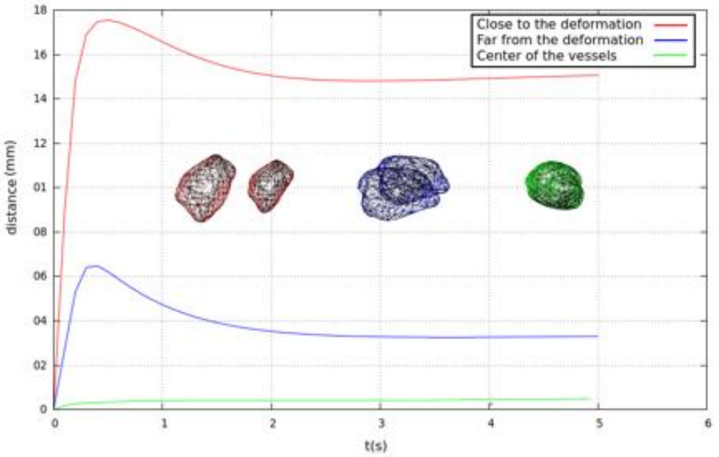

Figure 5.3: The impact of the vascular network on tumor deformation depending on its position in the liver: the distance between the tumor using homogeneous and heterogeneous biomechanical model is important locally (red) and globally (blue) and less important when the tumor is constrained by the vessels. The meshes illustrate the distance between the position of the tumor in a homogeneous and a heterogeneous case for each location in the liver.

5.4 Experiments on *in vivo* Human Liver

When dealing with an actual patient, quantitative validation implies major technical challenges as well as ethical issues. Our approach was conducted on a laparoscopic sequence taken during a real examination. Our aim is to assess the robustness of tracking in a real environment (specular lights, beating heart, respiratory motion, instrument occlusions) and the performance of our non-rigid registration.

5.4.1 Augmentation of Vascular Network and Tumor

The simulation employing this model was running stably in real-time: refresh rate of 25 FPS was achieved on a PC having equipped with an Intel i7 M620 2.76GHz processor, with images of a resolution of 960 × 540 acquired from DaVinci Robot provided by Intuitive Surgical.

In this sequence, the liver is deformed with a surgical tool manipulated by the surgeon. The right lobe is grasped and stretched in different directions reaching elongation up to 60% of the initial liver size. As stated in chapter 4, boundary conditions are necessary to yield satisfying results, especially where the liver undergoes high elongations. The MLS reconstruction permits to obtain a 3D surface that represents approximatively 30% of the liver. On the set of 264 extracted features 26 control points are built when using a radius $R_c = 5$ mm. Visual tracking performs well on a sequence of **812** frames showing long-term robustness of the tracking. The parameters of LK optical flow consist of a window size of 51 × 51 pixels and an interframe motion threshold of 20 pixels. The optical flow is prone to drifting and many features are filtered out during tracking leading to loss of control points. This may unbalance the minimization and disturb the registration where we noticed sudden deformations where the control points are deleted. Indeed, due to the fact that the elastic behaviour of the model aims at restoring its rest shape, deleting the external loads produces instabilities (in the neighbourhood of the corresponding tetrahedral element). However, this is only visible during a short time margin, since the mechanical model aims to interpolate the deformation where no loads are present. Overall, the registration gives coherent visual augmentation despite these visual disturbances. Figures 5.6 and 5.7 illustrate four frames of the augmentation and show a good visual match between laparoscopic images and the liver mesh.

Since no quantitative results can be obtained from *in vivo* data about the surface registration, we propose to compute the projection error (in percentage of the whole liver) of the overlaid mesh on the laparoscopic image. To do so, we measure the distance between the overlaid mesh contour and the liver contour, both extracted manually. Figure 5.4 illustrates these distances and shows that increasing the number of tetrahedral elements reduces significantly superimposition errors.

5.4.2 Performance Vs Accuracy

The computational cost of the simulation is given by several factors. First, due to the heterogeneity and anisotropy introduced by the vascular structures, iterative solvers (such as conjugate gradients) cannot be used due to convergence issues. Therefore, a direct solver (such as LDL-decomposition) is necessary to solve the system in each time step. However, the time needed to compute the

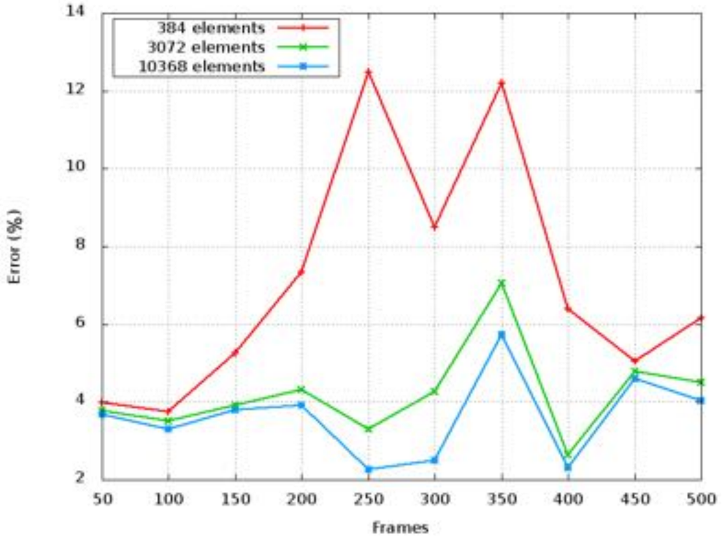

Figure 5.4: Projection error (in percentage of the whole liver) at selected frames, of the overlaid mesh on laparoscopic views with a variation of the number of elements.

LDL decomposition increases rapidly with the number of mechanical degrees of freedom of the model, which is given by the number of tetrahedral elements representing the parenchyma. Furthermore, the number of beam elements representing the vessels affects the performance as well, due to the computation of mapping which is calculated in each step of the simulation. Fig. 5.5 shows the relation between the number of tetrahedral and beam elements and the refresh rate of the simulation.

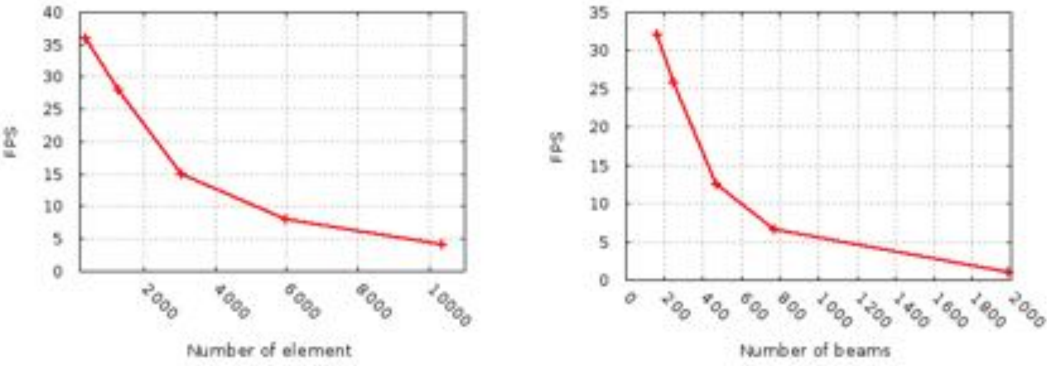

(a)

(b)

Figure 5.5: Performance of the simulation w.r.t. the number of elements: (a): different density of parenchyma meshes (while number of beams equals to 164), (b): different density of beam elements (while the same tetrahedral mesh is used with 3072 elements).

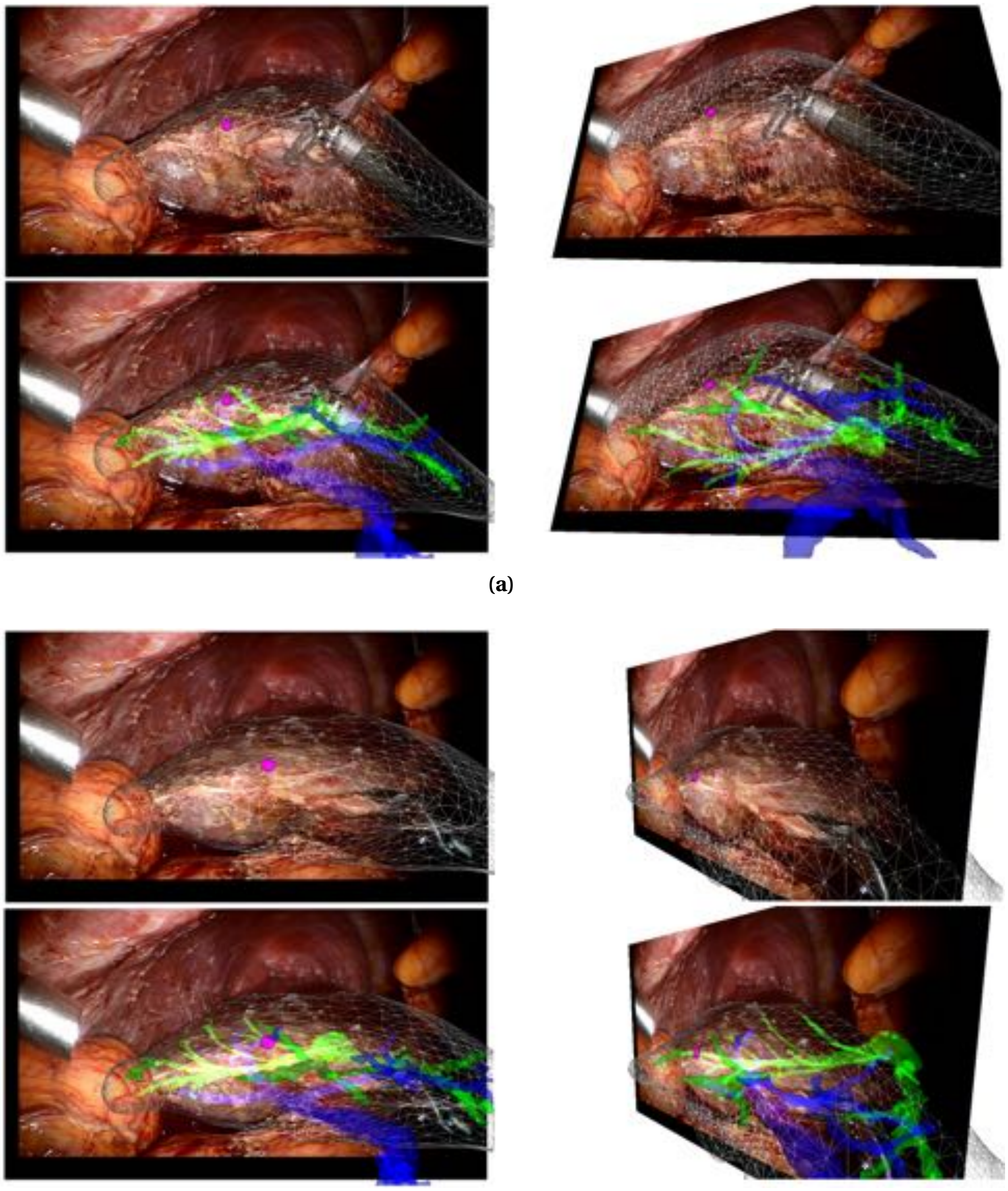

(a)

(b)

Figure 5.6: A sequence of images showing the superimposition of the real-time biomechanical model onto the human liver undergoing deformation due to surgical instrument interaction during MIS. The liver is represented in wireframe, the tumor in purple, the hepatic vein is shown in blue and the portal vein in green. On the left virtual camera with the original laparoscopic angle and right a different angle.

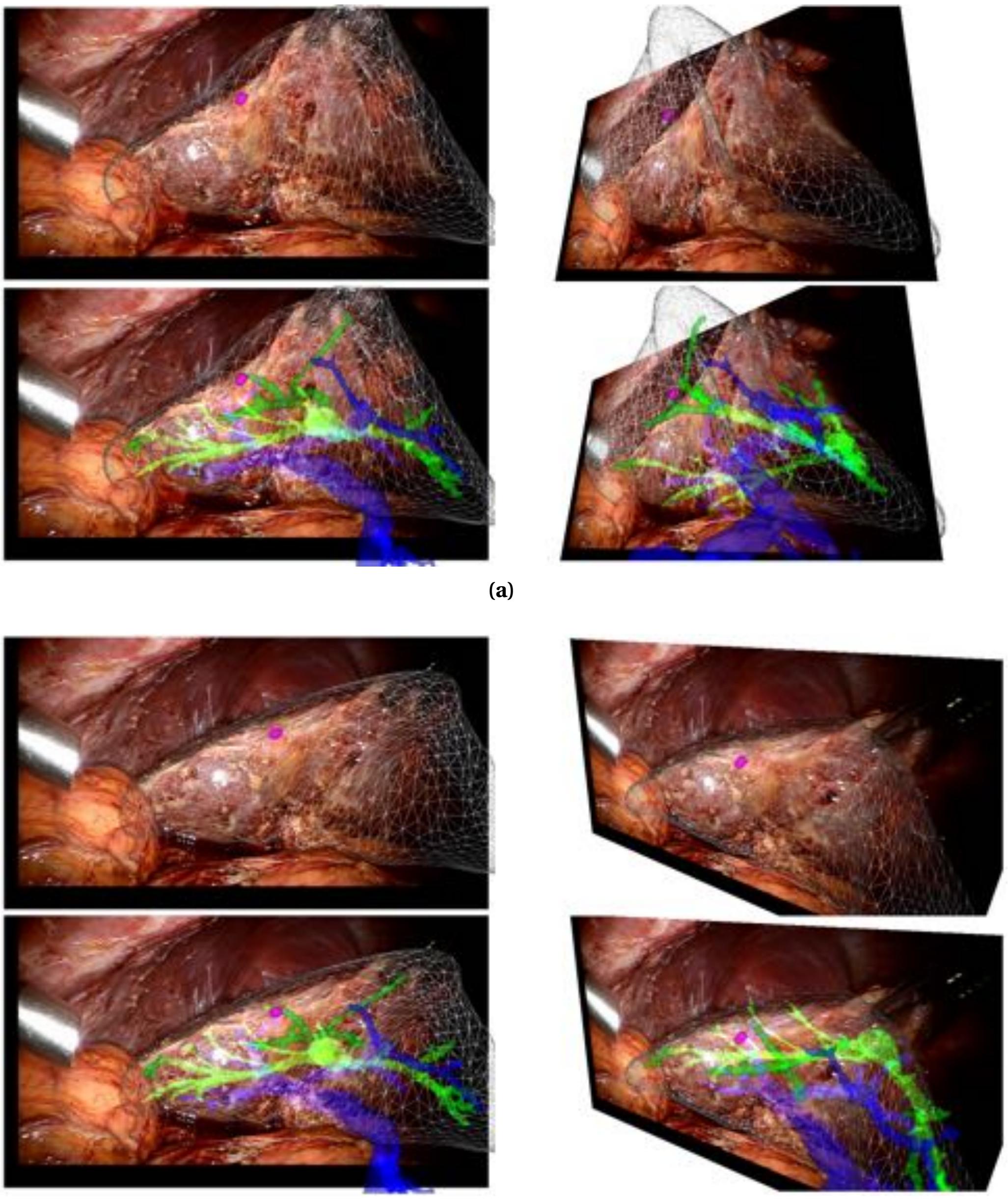

(a)

(b)

Figure 5.7: A sequence of images showing, in different views, the superimposition of the real-time biomechanical model onto the human liver undergoing deformation due to surgical instrument interaction during MIS. The liver is represented in wireframe, the tumor in purple, the hepatic vein is shown in blue and the portal vein in green. On the left virtual camera with the original laparoscopic angle and right a different angle.

5.4.3 Evaluation of the Cluster-based Filter

We further confront the tracking using cluster-based filtering with real clinical data. Figure 5.8 illustrates four selected frames of the augmentation performed on a sequence of **812** frames showing the long-term robustness of the tracking using the CbF.

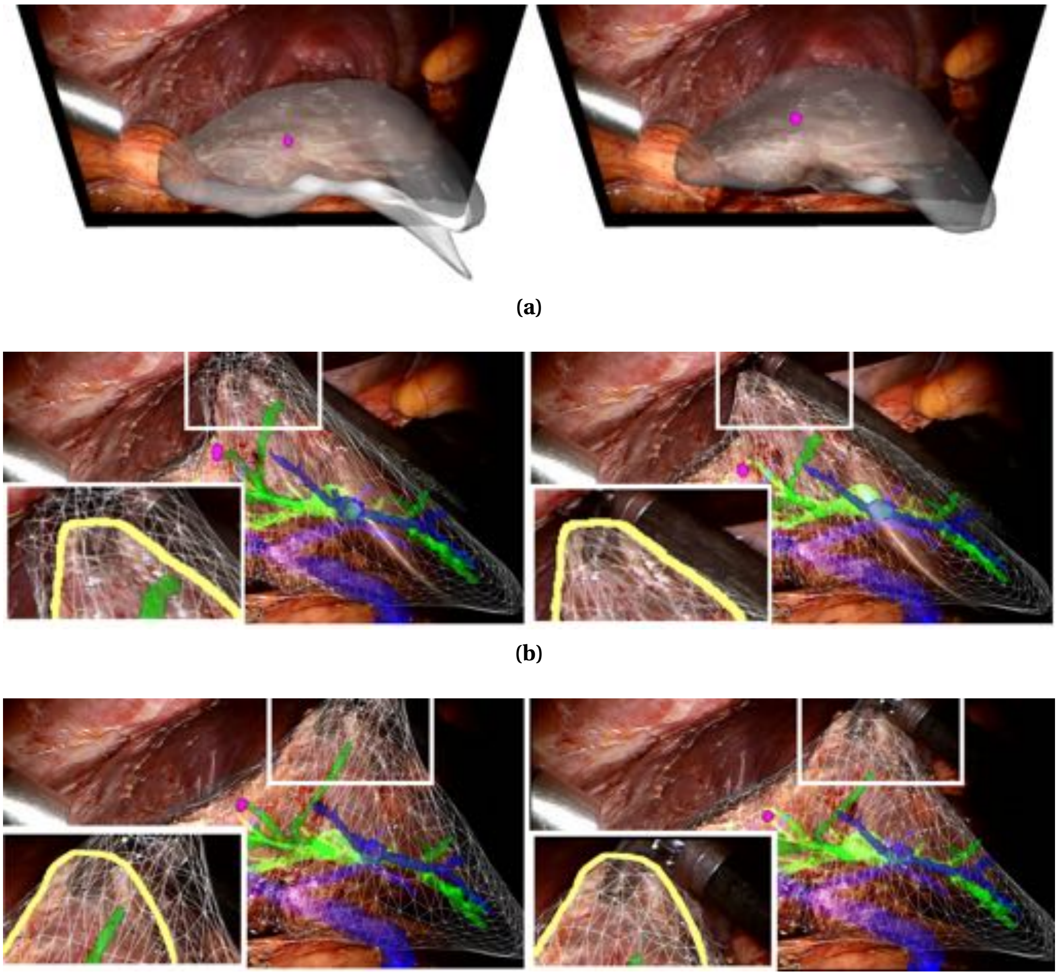

(a)

(b)

(c)

Figure 5.8: Comparison between (left) optical flow tracking and (right) tracking with CbF. (a) a top view showing the registration error that may occur using a direct method. The biomechanical model (in white wireframe) is locally constrained by a 3D feature in the case of a direct tracking while it is constrained by a set of features grouped around a control point. (b) and (c), a front view showing the visual accuracy of our method. The correct shape is well recovered even if the boundary (manually segmented and represented here in yellow) is not correct everywhere.

We can notice in the comparison illustrated in Figure 5.16 that the optical-flow tracking itself fails to accurately register the model onto the image, mainly because noisy 3D features which locally constraint the model are subject to drifts. Table 5.2 summarizes the projection errors of the mesh on the endoscopic images (manually extracted contours) and shows the CbF tracking permits to reduce considerably the error w.r.t the optical-flow approach.

	Projection error (px)			
Frame	**#100**	**#200**	**#300**	**#400**
Clusters-based Tracking	54.72	110.57	145.33	75.55
Optical-flow approach	809.95	659.04	304.78	766.01

Table 5.2: A comparison between the clusters-based approach and optical-flow tracking.

5.5 Experiments with Liver Phantom Data

In laparoscopic surgery, a reproducible validation remains a challenging task. In our case, the problem is more complex since neither qualitative results nor visual assessment can be used for validation easily since the internal structures are not visible in laparoscopic images. We believe that performing a CT scan of a phantom liver during the deformation is an ideal way of defining a ground truth for the location of an internal structure (e.g. a tumor). However, surgical instruments as well as the laparoscopic camera produce significant artifacts during a CT *in vivo* acquisition. Further, the boundary conditions of the liver surface, which influence the motion and deformation of the organ significantly, are difficult to reliably identify. Therefore, we designed a validation protocol in order to quantify the error of the prediction computed by the simulation. In the following, we first describe the bench used to validate our simulation by providing details about the phantom construction and desired properties. Second, we explain how the ground truth is determined and finally, we present a detailed comparison and evaluation of the results.

5.5.1 Bench Description

Required Properties

Quantitative validation strongly depends on the targeted application. The ex-vivo setup was designed to mimic as closely as possible a typical difficulty encountered during liver tumor resection in laparoscopy: the liver is firmly grasped and the tumor location must be predicted despite important deformations. The first two features concern the liver phantom that should be based on a patient-specific data, encompass the vasculature as well as tumors, and display known mechanical properties similar to those of a human liver. Ground truth tumor locations are tracked with successive CT-scans of the liver acquired while a progressive force is applied. The phantom and the global setup should be compatible with CT imaging. The applied force should be controlled to be reproduced in the simulation. Moreover, the reproducibility of the deformation is important also because recording the laparoscopic video and CT acquisition cannot be done simultaneously, thus each must be performed separately, even when using the same deformation. Finally, the grasping device should not occult video images and deformations should be varied, which requires the ability to modulate the force direction and amplitude.

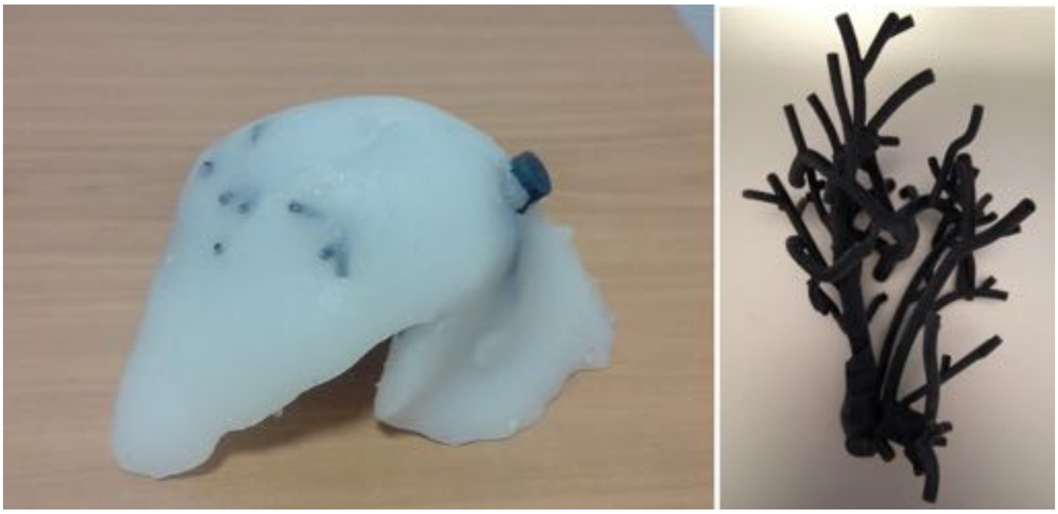

Figure 5.9: Heterogeneous liver phantom: the vascular network (right) is considered as the main source of heterogeneity of the silicon-made phantom (left).

Model Fabrication

To the best of our knowledge, the known polymers and similar materials are not capable of reproducing the behavior of liver tissue with high fidelity. However, extremely soft silicone rubber seems to be a good choice because it is close enough to real liver properties, has similar density and good maximal elongation before a failure occurs. Using a surface representation of real patient data, we employed 3D printing to reproduce the exact geometry of the organ and the vascular network.

Given the stiffness of the vessel wall reported for example in Umale et al. (2011), the network was produced directly by 3D printing using the softest available polymer (DM9895) having the Shore hardness A=90.

The fabrication of the parenchyma was performed using a mold made in a *Siligum* to reproduce the liver shape. The mold was further filled with an extremely soft silicone rubber mix using Ecoflexő 00-20 and additive Slackerő in ratio 1:1/8 by volume. During the filling procedure, the printed vascular networks together with artificial inclusions (representing randomly placed tumors) where inserted inside the mold. The phantom is shown in Fig. 5.9.

The procedure results in a very soft and elastic material representing the parenchyma with a harder vascular network placed inside. Each component is easily detectable on a CT scan in order to perform an automatic segmentation. Table 5.3 shows the values of the most significant parameters for each component. Finally, the phantom is manually textured with salient marks in order to ensure robust tracking.

	Vessels	**Parenchyma**	**Tumor**
Mass (gr)	30	675	0.2
Volume (cc)	32.9	690.2	6.3
Largest dimension (mm)	148	179	3
Young's Modulus (MPa)	9.2	0.05	-
Poisson's ratio	0.45	0.40	-

Table 5.3: Characteristics of the phantom vessels, parenchyma and tumors.

Bench Design and Construction

Considering the specifications and constraints formulated earlier, we apply a deformation so that the errors introduced due the friction between different parts of the setup are minimized. To induce the deformation, we use a servomotor BMS-2514 capable of a torque up to 23.2 kg.cm, attached to a pulley of 71 mm diameter. Three different threads attached to the same region of the liver surface using graspers are used to pull in three different directions aligned to x,y and z axes as seen in the camera view. The effective force up to 64 N can be applied on the liver surface via this mechanism depicted in Fig. 5.10.

Three different configurations induced by the threads are depicted in Fig. 5.10: in Configuration 1, a lateral pulling is applied, in Configuration 2, the surface is being pulled upwards and in Configuration 3, pulling towards the camera is performed.

To ensure the compatibility with X-ray based imaging, every element close to the liver is made of low density substances. More precisely, each grasper as well as the two closest pulleys have been specially designed and 3D-printed in PLA plastic, chosen for its high rigidity compared to other thermoplastics, providing reliability and stability in the output deformation. Polyamide bolts have been used to fix every element to the base platform.

Arduino-based micro-controller is used to control the servomotor which is driven according to the commands received from a wired electromagnetically

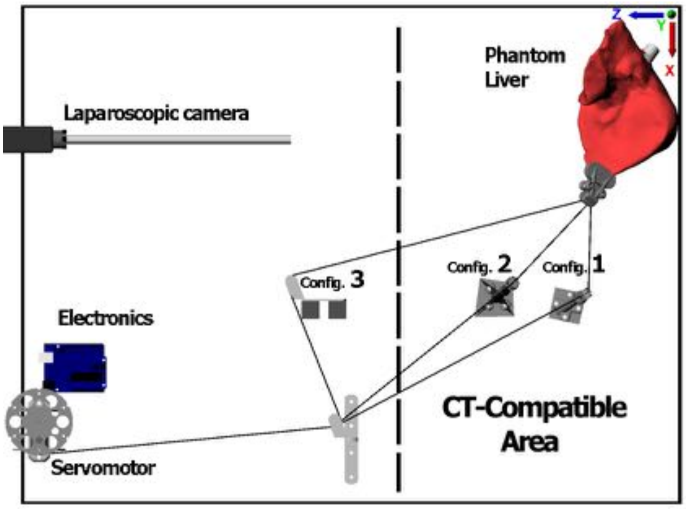

(a)

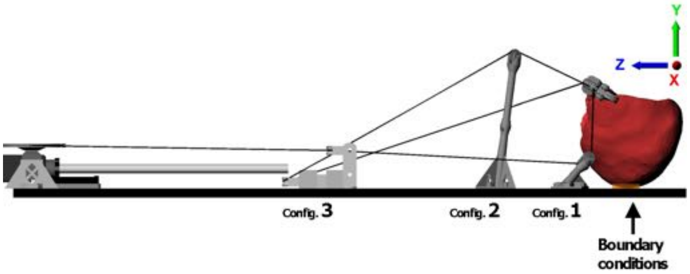

(b)

Figure 5.10: Validation bench with top (a) and side (b) views. The bench is CT-compatible and allows easy reproduction of the experiments. The three configurations permit to quantify the errors depending on the direction and elongation and at the same time, they can be simulated straightforwardly via Dirichlet boundary conditions.

isolated control pad. The control is also visualized using a LED which is used for synchronization.

The liver is fixed to the bench using glue to ensure fixed boundary conditions.

5.5.2 Ground Truth Acquisition

The ground truth acquisition involves two procedures described in Fig. 5.11):

- CT-scanning: we perform a CT scan of the phantom, being first at undeformed configuration, and then at different deformed configurations (cf. Tab. 5.4). The scans are acquired with Siemens Somatom CT Scanner which produces high quality volume images.
- Video streaming: we record the deformation induced by pulling the threads using a stereo endoscopic camera. The video stream is recorded

at 29.97 FPS producing 960 × 540 images acquired from the DaVinci Robot from Intuitive Surgical.

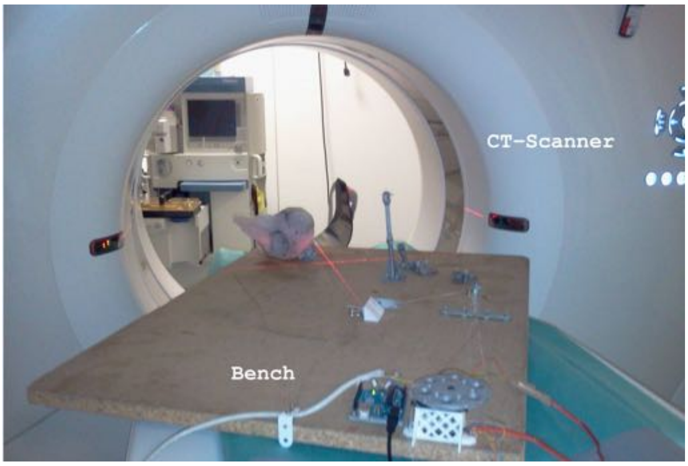

(a)

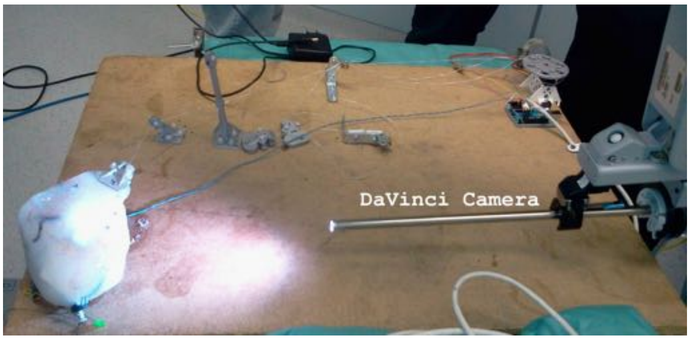

(b)

Figure 5.11: Experimental protocol for the quantitative validation: (a) CT-scanner with the bench. The wire hooked to the lobe is pulled by the servomotor and maintained in position while performing a new CT scan to provide a ground truth deformation. (b) An overview of stereoscopic camera acquiring a video stream of the deformation.

The two procedures are repeated for each configuration, so a sufficiently large data set is obtained giving the exact locations of the tumors and the corresponding stereo endoscopic views. A result of the three-dimensional reconstruction from CT scans is illustrated in Fig. 5.12.

5.5.3 Model Comparison and Quantitative Results

In order to justify the employment of a heterogeneous biomechanical model, a comparison with a homogeneous model is provided for three different tumor locations: near the point of traction (Tumor 1) and surrounded by vessels (Tumor 2 and Tumor 3). Additionally, a comparison with a mass-spring model is pro-

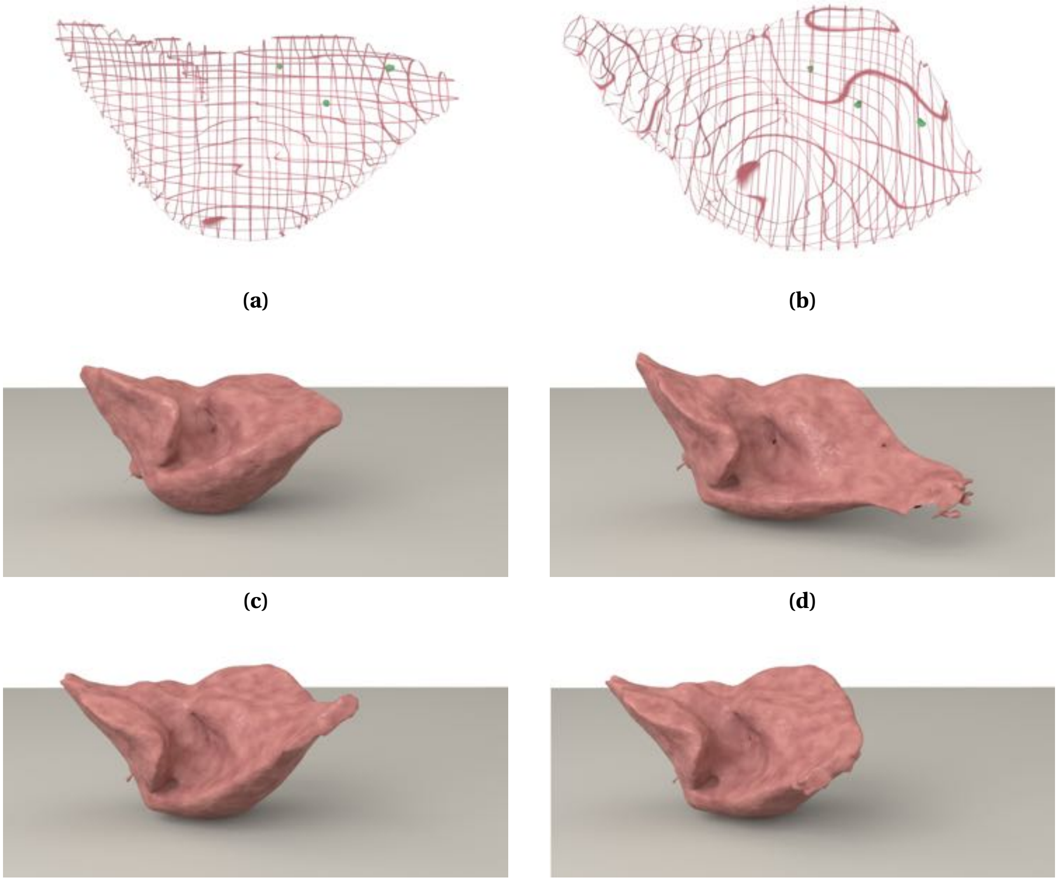

(a) (b) (c) (d) (e) (f)

Figure 5.12: CT-scans: the liver with the initial locations of the tumors in front (a) and top (b) views and 3D reconstructed phantom from CT images at rest (c) and deformed in Configuration 1 (d), Configuration 2 (e) and Configuration 3 (f).

	Config. 1	**Config. 2**	**Config. 3**
Elongation (mm)		**Force (N)**	
18.8	3.13	3.13	0.93
37.7	6.47	6.72	2.06
56.5	8.87	9.27	4.12
75.4	12.65	12.94	-

Table 5.4: Elongation and forces applied for each configuration.

vided. It should be emphasized that the comparison is done with the same data and parameters and using the same initial registration.

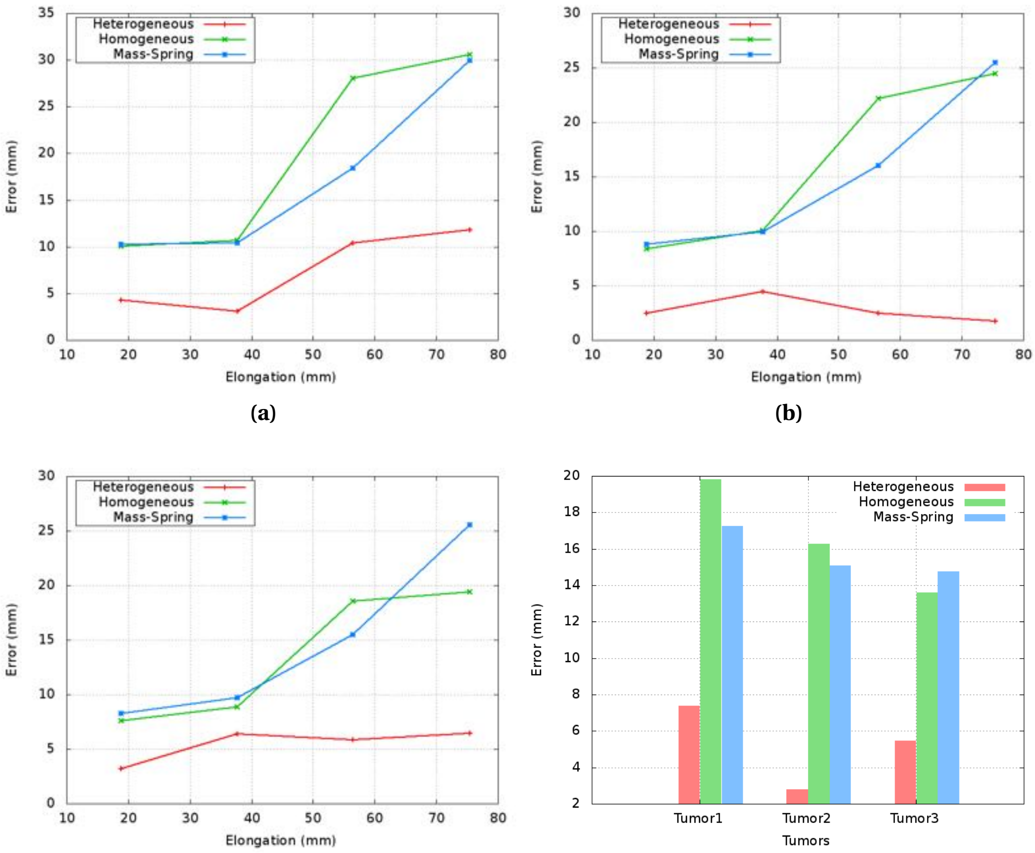

(a) (b)

(c) (d)

Figure 5.13: A comparison of homogeneous FEM model, heterogeneous FEM model and mass-spring model for the Configuration 1 with: Tumor 1 (a), Tumor 2 (b), Tumor 3 (c), and the average error (d).

Configuration 1

In this configuration the lobe is mainly pulled along x and z axes. The heterogeneous model gives the lowest errors when compared to the homogeneous and the mass-spring models. The largest difference between the models can be noticed in the case of Tumor 2 and Tumor 3 that are surrounded by vessels. Also, for those two tumors we can notice that despite the increase of elongation the error remains below 6 mm. The average error for Tumor 1 is 7.40 mm, 2.79 mm for Tumor 2 and 5.46 mm for Tumor 3, which is significantly lower than errors obtained from homogeneous and mass-spring models (cf. Fig. 5.13).

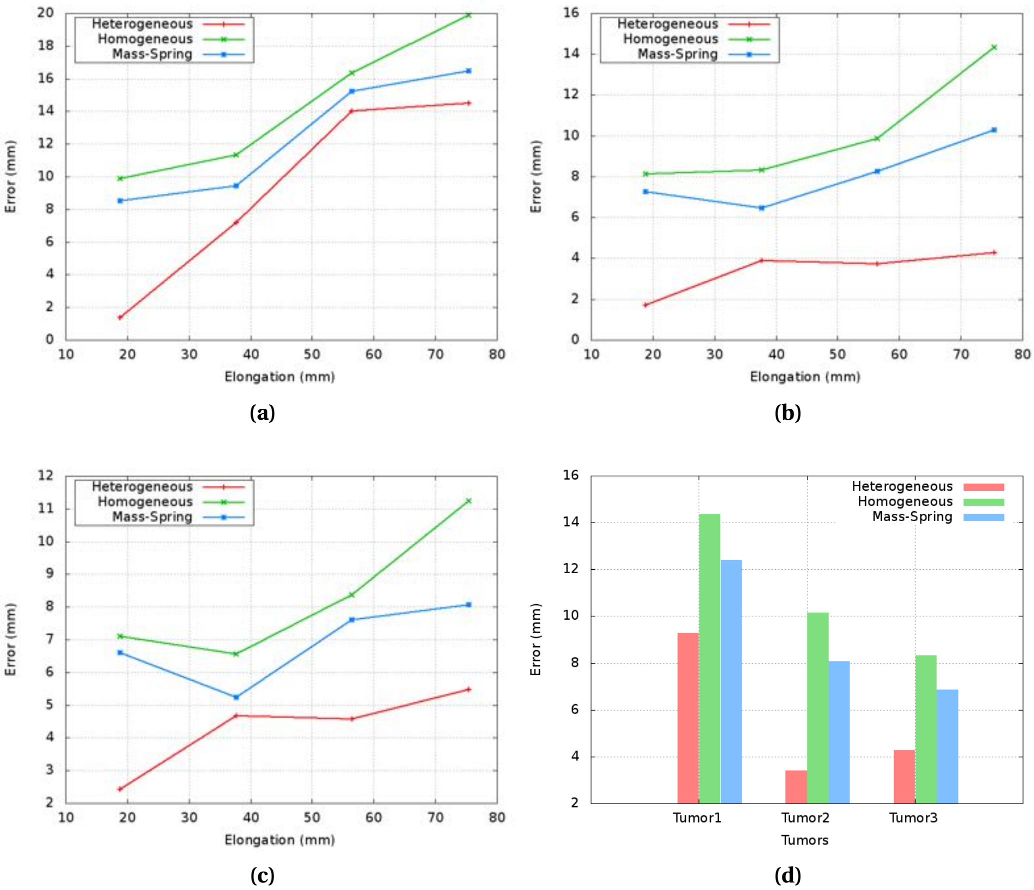

(a) (b)

(c) (d)

Figure 5.14: A comparison of homogeneous FEM model, heterogeneous FEM model and mass-spring model for the Configuration 2 with: Tumor 1 (a), Tumor 2 (b), Tumor 3 (c), and the average error (d).

Configuration 2

In this case the liver lobe is subjected to an elongation along y and z axes. Similarly to Configuration 1, the heterogeneous model gives the lowest errors when compared to the homogeneous and the mass-spring models. However, in Tumor 1, the error in heterogeneous model remains important (9.26 mm) and remains close to the results obtained using the other two models. Moreover, it increases with the elongation. It should be noted that the z axis shows the highest uncertainty in the 3D reconstruction which might partially explain the result, together with the magnitude of the external applied force. The average error for Tumor 2 is 3.39 mm and Tumor 3 4.28 mm.

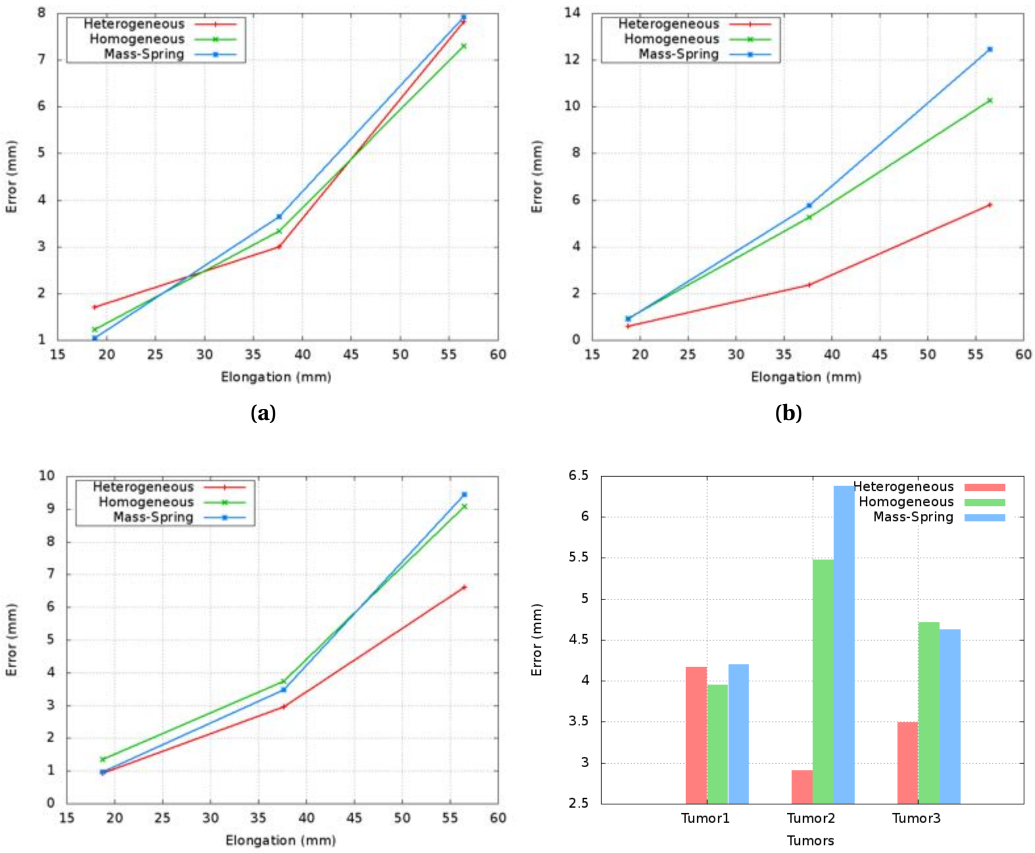

(a) (b)

(c) (d)

Figure 5.15: A comparison of homogeneous FEM model, heterogeneous FEM model and mass-spring model for the Configuration 3 with: Tumor 1 (a), Tumor 2 (b), Tumor 3 (c), and the average error (d).

Configuration 3

The purpose of Configuration 3 is to pull one lobe of the liver in the direction of the camera. Even if the average errors for the three tumors are low, (4.17 mm, 2.91 mm and 3.49 mm), we noticed a similarity between the three models which can be explained by the fact that the deformation underwent by the liver is close to a rigid transformation (mainly rotation). The vascular network effect on the behaviour is therefore reduced.

Overall

The overall results show that the use of a heterogeneous model reduces the distance between the scanned tumor and the simulated one considerably. These errors depend on the location of the tumor and the type of deformation.

5.6 Imposing additional Constraints

Solving the minimization problem $F_{\text{ext}} = F_{\text{int}}$ does not necessarily yields to a right mesh registration. Indeed, the biomechanical model can be forced to fit noisy points generated from the three-dimensional motion recovery. This can be highly damaging without imposing additional constraints in order to regularize the image fitting term.

One way to address this problem is to define additional penalties. These penalties have been widely studied and can be expressed as the form of M-estimators Rousseeuw and Leroy (1987); Zhang and Zhang (1997), widely used in computer vision, or using temporal consistency such as in Richa et al. (2010b) or take advantage of the global smoothness Stoyanov (2012) for tracking the heart surface.

We expose here two different types of penalties, that both offer a way to reduce the damage of noisy points on the registration: An image-based penalty where the reliability of 3D reconstruction is directly introduced in the minimization problem, and a mechanical constraint that defines a cut-off value to confine the external forces and detect aberrant measurements.

5.6.1 Image-based Penalties

Our aim is to take into account the uncertainty of the image data to reduce the registration error, so that non-rigid registration will be less prone to noisy 3D features. The errors of the image data are generated from an incorrect 3D reconstruction. Thus, we define the reprojection error measured from the triangulation step as a measure of reliability. This error is computationally cheap, purely geometric and computed as follows

$$d(\mathbf{x},\hat{\mathbf{x}})^2 + d(\mathbf{x}',\hat{\mathbf{x}}')^2 \tag{5.1}$$

where $d(*,*)$ represents Euclidean distance, x and x' are the matched points on the left and right image respectively, $\hat{x}$ and $\hat{x}'$ are the measured points lying close to x and x' and satisfying the equation $^{\top}\hat{x}\prime F\hat{x} = 0$.

We take advantage of this measure to associate each reconstructed 3D point with a reliability q. Reliability values are normalized so that $q = 1$ for the most reliable 3D point and $q = 0$ for the least reliable 3D point in $\mathbf{y}$ point set. We denote $\mathbf{q}$ the $3 \times n$ vector formed of all q values, assuming the quality is isotropic at each point. Thus, external forces are expressed as follows:

$$\mathbf{f_t}(\mathbf{x}) = \mathbf{L}^{\top} \cdot k \cdot \mathbf{q} \cdot \mathbf{L} \cdot (\mathbf{x} - \mathbf{x^0}) \tag{5.2}$$

Note that our method is built in a way to easily incorporate other measures of uncertainty. Indeed, since the recovery of the points implies different steps, several measures of uncertainty can be considered, such as the determinant of the Hessian matrix from SURF detector, the Euclidean distances of the matched SURF descriptors or the eigenvalues of the covariance matrix on the features.

5.6.2 Mechanical Penalties

The external stretching force being purely virtual, we propose to define a physical magnitude that will limit the external force amplitude. Moreover, since the noise is mainly due to a bad depth estimation, the stiffness of the detected outlier is cancelled instead of simply deleted. In the meantime, this constraint also ensures that the energy minimization remains the same at each time step by preventing the mesh from suddenly loosing features which will locally disturb the model. Furthermore, the physical penalties are expressed for each control point c_i as follows:

$$k \cdot \|\mathbf{y}_i - \mathbf{y^0}_i\| < \lambda \tag{5.3}$$

where $\mathbf{y}_i$ and $\mathbf{y^0}_i$ are vectors representing the position of the control points c_i, respectively at any time t and time $t = 0$, where the subscript i denotes the control points. The value λ is the maximal force amplitude.

This penalty fits within our framework and can be added for each control point without affecting the real-time performance. Combining this penalty with the optical flow temporal constraints and the boundary conditions results in a system that is sufficiently constrained to yield good results.

5.6.3 Evaluation

We estimate the registration error by calculating Euclidean distance $\|m - p\|$ between the degree of freedom m of the mechanical model and the tracked point p in the endoscopic images. RMS error is measured at each frame on two different views of the liver showing respectively the left and right lobe and plotted in Figure 5.16 where we conduct a comparison with tracking without additional constraints.

We can notice that the mechanical penalty reduces considerably the registration. The calculated average RMS error is **2.48 mm** for the left lobe and **4.8 mm** for the right lobe, way below tracking using image-based penalties and without additional constraints.

5.7 On the importance of Young's modulus

The main idea behind the method presented in the chapter 4 is to use features extracted from laparoscopic image as external loads to drive a biomechanical

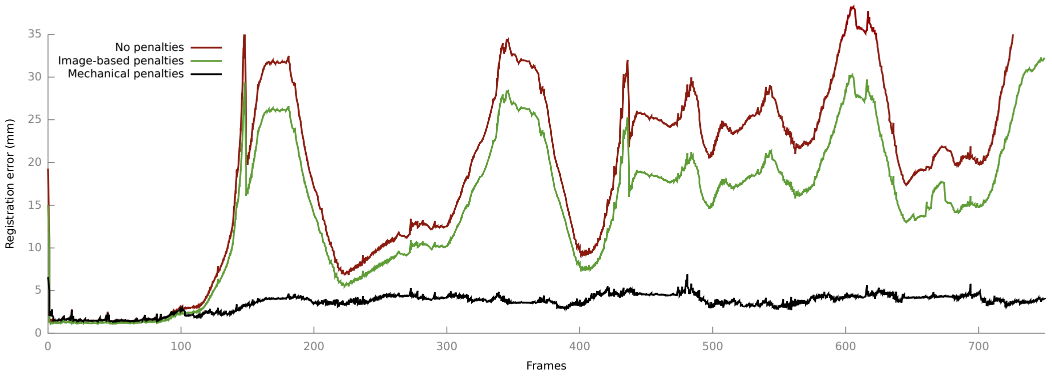

(a)

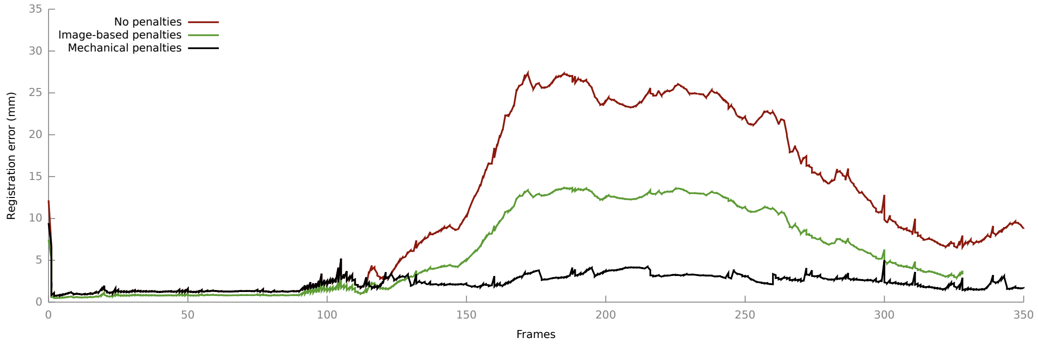

(b)

Figure 5.16: A comparative study between our tracking and related works conducted on *in-vivo* human liver with (a) left lobe and (b) right lobe. The registration error using mechanical penalties is considerably reduced. We can also notice that the errors are very close until the frame 100 where outliers appear and disturb the registration.

model. These features are considered as external constraints and can be expressed as forces, such as in Eq. 5.2 or as displacement. Each expression involves a different modeling of the physical model. If we consider $u \in \mathbb{R}^3$ a tracked point estimated from images and $v \in \mathbb{R}^3$ the corresponding point mapped in the biomechencial model, expressing external constraints as displacement means that we impose to the point v to have the exact position of the point u. Thus, the material stiffness is less important. However, when we express the external loads as forces, the model plays a regularization role where the point v will not exactly lie on the point u when reaching an equilibrium. At this time, the material stiffness plays an important role in the final solution.

We propose in the following to experimentally demonstrate the role of Young's Modulus when considering each expression of external loads, by conducting simulated tests for each scenario.

We performed the study on a laparoscopic scene that represents the right and left lobes separated in the anterior side by the falciform ligament (Fig. 5.17). We

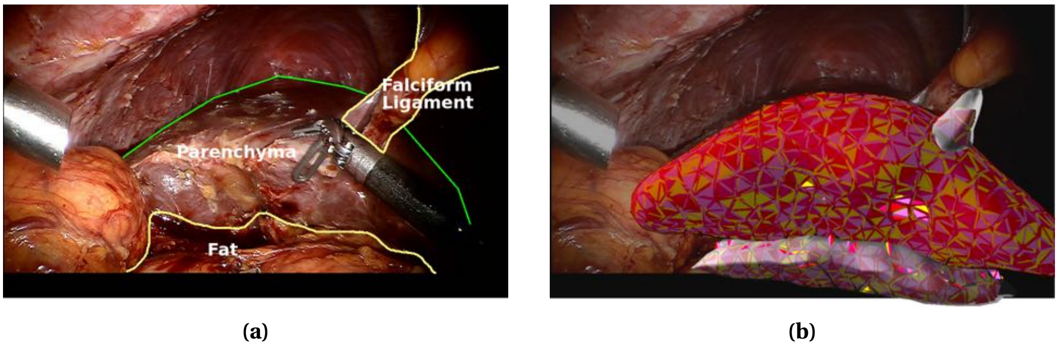

Figure 5.17: Laparoscopic view of the liver showing (a) the contours of lobes, falciform ligament and surrounding fat, (b) superimposed FE meshes generated from pre-operative CT scans.

used the same model described in Chapter 4 for the parenchyma with Young's modulus set to $E_{par} = 27\,\text{kPa}$. The ligaments are simulated with FEM using the corotational formulation with Young's modulus of $E_{lig} = 150\,\text{kPa}$ (fixed nodes can also be considered). The falciform ligament is difficult to extract from the pre-operative images, however, recent work Plantefeve et al. (2014) shows promising results in the transfer of the ligament positions using atlas-based techniques. Thus, we assume that the ligament position can be determined. The underlying fat supporting the liver is also modeled to simulate the surrounding connective tissues.

We consider two scenarios: first, the liver is deformed with a surgical instrument with known positions. Second, a force similar to that imposed by the instrument is applied to the surface of the liver. The important difference between these experiments is in the type of load that creates the deformation: in the first case, a displacement is imposed on a part of the mesh (in the region of the liver that is being grasped), whereas in the second case a force (an effort) is imposed on the surface of the model.

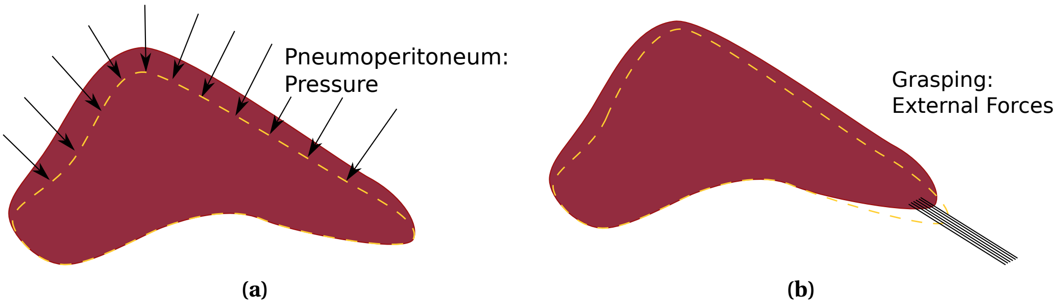

Figure 5.18: Simulation scenarios: (a) simulation of pneumoperitoneum by the application of a pressure on the liver surface, (b) the liver is deformed with a surgical instrument by a prescribed displacement/force.

For each scenario we under- and over-estimate the Young's modulus of the parenchyma E_{par} by the factor of two w.r.t. the reference simulation. In both cases, the goal is to obtain the displacement field of the nodes of the liver model. The error evaluation of the displacement is done after the equilibrium is achieved using RMSE error.

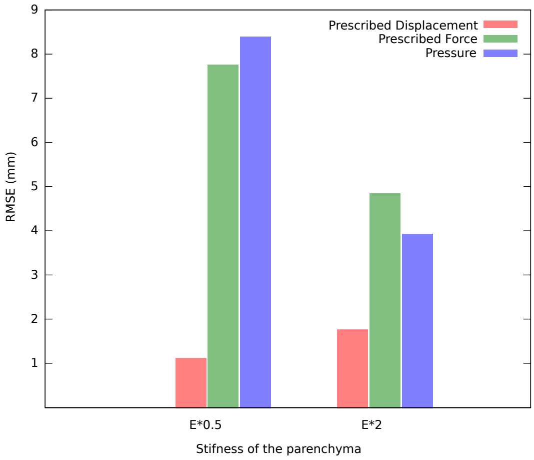

Figure 5.19: Evaluation of the RMS error (in mm) for prescribed displacement and prescribed forces (traction and pressure), compared to our reference simulation.

The grasping is simulated by prescribing a displacement on the lobe of the liver with a maximum displacement of 75 mm. To ensure that both prescribed displacements/efforts tests result in a similar motion. The prescribed force value is computed from the prescribed displacements scenario. We measure the average elastic force of the displaced nodes of the liver after equilibrium. In our experiment, a traction force of 15.42 N has to be applied on the nodes to be equivalent to the prescribed displacements. It should be emphasized that the direction of the force vector is chosen to be the same as the one of the displacement vector and the displacements and efforts are prescribed on the same nodes.

An additional scenario similar to the second one is considered by applying a pressure on the surface of the model to simulate pneumoperitoneum. An average pressure of 12 mmHg, usually chosen by the surgeon during abdominal laparoscopic surgery Bano et al. (2012), is applied.

The results presented in Fig. 5.19 show two specific scenarios: simulations where the deformation is induced by prescribing a displacement and those where applied forces are prescribed, each of them having their own requirements.

Considering prescribed displacements, our results show that a large difference in the elasticity parameter of the liver has a relatively small impact on the error. As for the prescribed forces, the influence of variation in Young's modulus of the parenchyma is much more significant than in the case of prescribed displacements. The results emphasize the importance of using patient-specific data in such scenarios.

5.8 Conclusion

We presented in this chapter several experiments conducted on computer-generated data, human liver data and phantom data. We demonstrate the impact of modeling of the vascular network through simulations. A complete experimental bench capable to reproduce as closely as possible a typical scenario encountered during liver tumor resection was designed, where we calculate tumor position errors below the safety margins actually preserved during interventions. Promising results were also obtained using *in-vivo* human liver data in terms of surface registration and a computation time compatible with the real-time visual feedback.

We then proposed and evaluated the imposition of additional constraints to the minimization, in order to bring the visual tracking more robustness and make the non-rigid registration less prone to outliers. We finally conducted a sensitivty study to evaluate the importance of Young's Modulus, depending on the expression of external loads.

CHAPTER 6

GENERAL CONCLUSION

6.1 Conclusion

Augmented Reality has the potential to offer significant improvements to the medical practice in terms of decision support and navigation. In the domain of minimally invasive hepatic surgery, technical improvements such as visual feedback and localisation of risky areas aim to make the surgical more intuitive for surgeons and the procedure safer for patients.

The work presented in this thesis addressed several important limitations that currently hinder the use of Augmented Reality in clinical routine of minimally invasive procedures. We particularly focus on three-dimensional localization and visualization of internal structures, such as blood vessels and tumors. To this end, we have developed an image-guided biomechanical model that is able to capture complex deformations underwent by the liver during surgery. The deformation model is guided by both internal forces (associated to a biomechanically validated model of the liver) and external forces related to three-dimensional points (reconstructed from stereo images) which incorporate a quality measure of their reliability. Such characteristics make our model able to capture both the organ surface and inner structures motion while being parameterized with textbook Young's modulus and Poisson's ratio values.

Large elastic deformations are efficiently handled, thanks to the use of a heterogeneous model capable of faithfully translating liver behaviour. This model that considers the vascular network as the main source of heterogeneity achieves real-time performance, while ensuring accuracy and stability.

Tracking the liver surface imposes several challenges from a computer vision point of view. A long-term visual recovery method based on surface reconstruction using moving-least squares and temporal tracking based on a cluster-based filter has been proposed for estimating liver motion. By integrating the physical model to visual tracking, tracking robustness facing disturbances and occlusions is significantly improved.

Promising results were obtained through *in-vivo* qualitative assessment on a human liver and quantitative validation on a phantom liver in terms of surface registration and localisation of internal tumors. We reported an estimation of the position below the actual clinical margin and a computation time compatible with the real-time visual feedback.

6.2 Perspectives

In order to design a full Augmented Reality system for a practical use in real surgical scenarios, some issues require a special attention.

From a simulation point of view, we believe that the use of a real-time heterogeneous biomechanical model permits to accurately reproduce the behaviour of the liver undergoing large deformations. However, we are aware that a better definition of the *boundary conditions* is needed to capture its motion with an increased accuracy. We consider addressing this issue already in the initial registration phase. Finally, a correct estimation of the mechanical properties is another key aspect that is to be improved, as these parameters are known to vary significantly. We believe that integrating the elastography data recorded pre-operatively could substantially increase the accuracy of the model. However, a deeper sensitivity study concerning the importance of these parameters has to be conducted, where recent works Miller and Lu (2013); Bosman et al. (2014) exhibit that depending on the simulation scenario, patient specific tissue parameters may not be necessary.

From a computer vision point of view, several disturbances may occur during the tracking stage due to the outliers. Actual clinical conditions where smoke, bleeding, or other surgical events may hinder the tracking. One way to reduce the impact of the outliers, is the *labelling of the intra-abdominal scene* by segmenting the liver, the surrounding tissues and the surgical tools to isolate the liver surface.

Another limitation concerning the practical implementation of the method in the clinical environment is given by the *initial registration*, which is done manually. As stated before, substantial improvement of this part of the work flow is beyond the scope of this work since the solution is quite complex as the underlying problem is ill-posed due to the difficult extraction of salient geometrical and anatomical landmarks from the patient data. Promising preliminary results were obtained using anatomical landmarks and an atlas-based model Plantefeve et al. (2014).

More *validation* is obviously required though it is worth mentioning that validations implying actual organs are seldom reported in previous works. A quantitative evaluation of the impact of the initial registration on the tumor position has to be conducted, and several cases have to be studied in order to better assess the method.

As a longer-term perspective, we would like to explore and answer two essential questions: The first one is "How to define the role of surgeons in the framework?". We strongly believe that it is necessary to fully involve surgeons as essential actors in the framework. In order to answer this question, it is important to first define a protocol to extract the real needs of surgeons. The second question concerns computer vision, "Is computer vision the solution when dealing with surgical data ?" We believe that computer vision at its own can hardly reach the level of robustness required for medical routines. More precisely, images acquired from the laparoscopic camera are still very challenging to process and would deserve to be enriched, either thanks to optical hardware modifications, where in the future more advanced camera capable of direct 3D reconstruction can find their place in laparoscopy, or changes in tissue texture with additional natural landmarks. Moreover, the imaging modalities such as MRI, CT, US can also be considered in the operating room, in order to provide a correct initial 3D model that will simplify the initial alignment. These two points are to be addressed jointly, where surgeons can be a solution to validate and control computer vision algorithms to increase robustness of visual tracking and reconstruction.

APPENDIX A

APPENDIX A

A.1 Time Integration

In order to simulate dynamic deformable solids, we need to know the time dependent world coordinates $\mathbf{x}(\mathbf{m}, t)$ of all points in M. Given $\mathbf{x}(\mathbf{m}, t)$ we can subsequently display the configurations $\mathbf{x}(0), \mathbf{x}(\Delta t)$, .. describing the motion and deformation of the object. Here Δt is a fixed time step of the simulation and $\mathbf{x}(t)$ represents the entire vector field at time t. The unknown vector fields $\mathbf{x}(t)$ are not given directly but implicitly as the solution of a differential equation, namely Newton's second law of motion of the form

$$\ddot{\mathbf{x}} = F(\dot{\mathbf{x}}, \mathbf{x}, t) \tag{A.1}$$

where $\ddot{\mathbf{x}}$ and $\dot{\mathbf{x}}$ are the second and first time derivatives of $\mathbf{x}$, respectively and $F()$ a general function given by the physical model of the deformable object. In order to find the solution $\mathbf{x}(t)$, this second order differential equation is often rewritten as a coupled set of two first order equations

$$\begin{cases} \dot{\mathbf{x}} = \mathbf{v} \\ \dot{\mathbf{v}} = F(\mathbf{v}, \mathbf{x}, t) \end{cases} \tag{A.2}$$

where the new quantity $\mathbf{v}$ represents $\dot{\mathbf{x}}$. A discrete set of values $\mathbf{x}(0)$, $\mathbf{x}(\Delta t)$, $\mathbf{x}(2\Delta t)$, .. of the unknown vector field $\mathbf{x}$ which is needed for the animation can now be obtained by numerically solving (i.e. integrating) this system of equation.

There exist a number of integration schemes, (see (Hauth et al., 2003) for instance). We only describe here the forward euler (explicit)and backward euler (implicit) integration scheme.

Explicit scheme

Explicit scheme or forward Euler, is the simplest integration scheme. The time derivatives are replaced by finite differences

$$\begin{cases} \dot{\mathbf{v}}(t) = [\mathbf{v}(t+\Delta t) - \mathbf{v}(t)]/\Delta t \\ \dot{\mathbf{x}}(t) = [\mathbf{x}(t+\Delta t) - \mathbf{x}(t)]/\Delta t \end{cases} \tag{A.3}$$

Substituting these into the above equations and solving for the quantities at the next time step $t + \Delta t$ yields

$$\begin{cases} \mathbf{x}(t+\Delta t) = \mathbf{x}(t) + \Delta t \mathbf{v}(t) \\ \mathbf{v}(t+\Delta t) = \mathbf{v}(t) + \Delta t F(\mathbf{v}(t), \mathbf{x}(t), t) \end{cases} \tag{A.4}$$

One advantage of explicit methods is that they are easy to implement. however they are stable only only if the time step Δt is smaller than a stability threshold. This threshold can be very small for stiff objects, and if violated can lead the simulation to explode.

Implicit scheme

Implicit scheme (or backward Euler) can counteract the stability issue of the explicit integration by adding quantities at the next time step $t+\Delta t$ on both sides of the equation

$$\begin{cases} \mathbf{x}(t+\Delta t) = \mathbf{x}(t) + \Delta t \mathbf{v}(t+\Delta t) \\ \mathbf{v}(t+\Delta t) = \mathbf{v}(t) + \Delta t F(\mathbf{v}(t+\Delta t), \mathbf{x}(t+\Delta t), t) \end{cases} \tag{A.5}$$

The implicit Euler scheme is stable for arbitrarily large time steps Δt. This gain comes with the price of having to solve an algebraic system of equations at each time step.

A.2 Linear Elasticity

When linearized, the relationship for an element e connecting n_e nodes can simply be expressed as

$$\mathbf{f}_e = \mathbf{K}_e \mathbf{u}_e \tag{A.6}$$

where $\mathbf{f}_e \in \mathbb{R}^{3n_e}$ contains the n_e nodal forces and $\mathbf{u}_e \in \mathbb{R}^{3n_e}$ the n_e nodal displacements of an element. The matrix $\mathbf{K}_e \in \mathbb{R}^{3n_e \times 3n_e}$ is called the stiffness matrix of the element. Because elastic forces coming from adjacent elements add up at a node, a stiffness matrix $\mathbf{K} \in \mathbb{R}^{3n \times 3n}$ for an entire mesh with n nodes can be formed by assembling the element's stiffness matrices

$$\mathbf{K} = \sum_e \mathbf{K}_e \tag{A.7}$$

In the linear case, if we let $\mathbf{u} = \mathbf{x} - \mathbf{x_0}$ where the vectors $\mathbf{x}$ and $\mathbf{x_0}$ contain, respectively, the actual and the rest positions of the nodes. The equation of motion in the dynamic case can be written

$$\mathbf{M}\ddot{\mathbf{u}} + \mathbf{D}\dot{\mathbf{u}} + \mathbf{K}\mathbf{u} = \mathbf{f}_{ext} \tag{A.8}$$

where $\mathbf{M} \in \mathbb{R}^{n \times n}$ the mass matrix, $\mathbf{D} \in \mathbb{R}^{n \times n}$ the damping matrix and $\mathbf{f}_{ext} \in \mathbb{R}^n$ externally applied forces. If we consider that mass and damping effects are concentrated at the nodes (technique called mass lumping) then $\mathbf{M}$ and $\mathbf{D}$ are diagonal matrices. In this case, $\mathbf{M}$ just contains the point masses of the nodes of the mesh on its diagonal. The damping matrix $\mathbf{D}$ is often defined as a linear combination of the stiffness matrix $\mathbf{K}$ and the mass matrix $\mathbf{M}$, and is referred to as Raleigh damping ($\mathbf{D} = \alpha\mathbf{M} + \beta\mathbf{K}$).

A.3 Mass-spring System

Mass-springs System is a very intuitive deformable model Miller (1988). In this model, the deformation is approximated by a set of point masses connected by massless springs. Instead of going through a discretization stage, the model offers directly a discrete model which only require the solution of a system of coupled ordinary differential equations.

Springs are commonly modeled as being linearly elastic; the force acting on mass i, generated by a spring connecting i and j together is

$$\mathbf{f}_i = k_s(|\mathbf{x}_{ij}| - l_{ij})\frac{\mathbf{x}_{ij}}{|\mathbf{x}_{ij}|} \tag{A.9}$$

where $\mathbf{x}_{ij}$ is the difference between the two masses' position vectors $(\mathbf{x}_j - \mathbf{x}_i)$, k_s is the spring's stiffness and l_{ij} is its rest length.

A.4 Sofa: An open source framework for medical simulation

SOFA[1] is an Open Source framework primarily targeted at real-time simulation, with an emphasis on medical simulation. The development of SOFA started 7 years ago, from a common vision of several teams at INRIA and of the CIMIT simulation group Allard et al. (2007). In recent years, SOFA framework has begun to be renown worldwide as an open-source libraries of reference in the field of interactive (bio)mechanical simulation. SOFA facilitates collaborations between specialists from various domains, by decomposing complex simulators into components designed independently, and providing a simple way of building simulation prototypes. Each component encapsulates one of the aspects of a simulation, such as the degrees of freedom, the forces and constraints, the differential equations, the main loop algorithms, the linear solvers, the collision detection algorithms or the interaction devices... The simulated objects can be represented using several models, each of them optimized for a different task such as the computation of internal forces, collision detection, haptics or visual display as described in Faure et al. (2012).

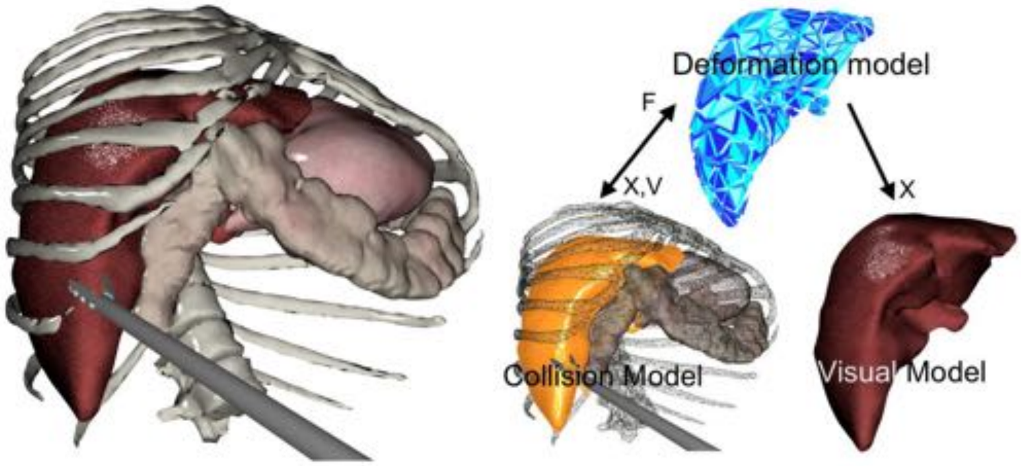

Figure A.1: A simulated Liverin SOFA. Left: The liver displayed in its environment. Right: Three representations are used for the liver: one master model for the internal deformable mechanics, one for the collisions, and one for the visualization. Mappings (black arrows) are used to propagate positions (X) and velocities (V) from master to slaves, while forces (F) are propagated in the opposite direction. From Faure et al. (2012).

---

[1] www.sofa-framework.org

A.5 Additional material

- Single View Augmentation of 3D Elastic Objects `http://youtu.be/dMmpUoFbBDo`
- Accurate Tracking of Hepatic Tumors for Augmented Reality in Robotic Assisted Surgery: `http://youtu.be/dMmpUoFbBDo`

LIST OF FIGURES

LIST OF TABLES

REFERENCES

[CGA] *Cgal, Computational Geometry Algorithms Library*. `http://www.cgal.org`.

[WHO] *World Health Organisation*. `http://www.who.int`.

[Agudo et al., 2012] A. Agudo, B. Calvo and J. M. M. Montiel. *Finite Element based sequential Bayesian Non-Rigid Structure from Motion*. In *CVPR*, pages 1418–1425, 2012.

[Albitar et al., 2007] C. Albitar, P. Graebling and C. Doignon. *Robust Structured Light Coding for 3D Reconstruction*. In *Computer Vision, 2007. ICCV 2007. IEEE 11th International Conference on*, pages 1–6, 2007, ISSN 1550-5499.

[Allan et al., 2013] M. Allan, S. Ourselin, S. Thompson, D. Hawkes, J. Kelly and D. Stoyanov. *Toward Detection and Localization of Instruments in Minimally Invasive Surgery*. Biomedical Engineering, IEEE Transactions on, vol. 60, no. 4, pages 1050–1058, 2013.

[Allard et al., 2007] J. Allard, S. Cotin, F. Faure, P. J. Bensoussan, F. Poyer, C. Duriez, H. Delingette and L. G. B. *SOFA - an Open Source Framework for Medical Simulation*. In *Medicine Meets Virtual Reality (MMVR 15)*, 2007.

[Allard et al., 2011] J. Allard, H. Courtecuisse and F. Faure. *Implicit FEM and Fluid Coupling on GPU for Interactive Multiphysics Simulation*. In *ACM SIGGRAPH 2011 Talks*, SIGGRAPH '11, pages 52:1–52:1, 2011, ISBN 978-1-4503-0974-5.

[Amenta and Kil, 2004] N. Amenta and Y. J. Kil. *Defining Point-set Surfaces*. ACM Trans. Graph., vol. 23, no. 3, pages 264–270, 2004, ISSN 0730-0301.

[Ayache et al., 1998] N. Ayache, S. Cotin and H. Delingette. *Surgery Simulation with visual and haptic feedback*. In *Robotics Research, the Eigth International Symposium*, edited by Y. Shirai and S. Hirose, pages 311–316, Springer, 1998.

[Azuma, 1997] R. T. Azuma. *A survey of augmented reality*. Presence: Teleoperators and Virtual Environments, vol. 6, no. 4, pages 355–385, 1997.

[Bano et al., 2012] J. Bano, A. Hostettler, S. Nicolau, S. Cotin, C. Doignon, H. Wu, M. Huang, L. Soler and J. Marescaux. *Simulation of Pneumoperitoneum for Laparoscopic Surgery Planning*. In *Medical Image Computing and Computer-Assisted Intervention - MICCAI 2012*, vol. 7510, pages 91–98, 2012, ISBN 978-3-642-33414-6.

[Baraff, 1998] W. A. Baraff, D.. *Large steps in cloth simulation.* In *In Proceedings of ACM SIGGRAPH 1998*, pages 43–54, 1998.

[Barbič and James, 2005] J. Barbič and D. L. James. *Real-time subspace integration for St. Venant-Kirchhoff deformable models.* In *ACM Transactions on Graphics (TOG)*, vol. 24(3), pages 982–990, ACM, 2005.

[Barreto et al., 2009] J. P. Barreto, J. Roquette, P. Sturm and F. Fonseca. *Automatic Camera Calibration Applied to Medical Endoscopy.* In *Proceedings of the British Machine Vision Conference*, pages 52.1–52.10, 2009.

[Bartoli, 2008] A. Bartoli. *Maximizing the Predictivity of Smooth Deformable Image Warps Through Cross-Validation.* J. Math. Imaging Vis., vol. 31, no. 2-3, pages 133–145, 2008, ISSN 0924-9907.

[Bartoli and Zisserman, 2004a] A. Bartoli and A. Zisserman. *Direct estimation of non-rigid registration.* In *British Machine Vision Conference*, 2004a.

[Bartoli and Zisserman, 2004b] A. Bartoli and A. Zisserman. *Direct estimation of non-rigid registration.* In *In British Machine Vision Conference*, 2004b.

[Bartoli et al., 2012] A. Bartoli, Y. Gerard, F. Chadebecq and T. Collins. *On template-based reconstruction from a single view: Analytical solutions and proofs of well-posedness for developable, isometric and conformal surfaces.* In *Computer Vision and Pattern Recognition (CVPR), 2012 IEEE Conference on*, pages 2026–2033, 2012, ISSN 1063-6919.

[Baumann et al., 2009] M. Baumann, P. Mozer, V. Daanen and J. Troccaz. *Prostate Biopsy Assistance System with Gland Deformation Estimation for Enhanced Precision.* In *Proceedings of the 12th International Conference on Medical Image Computing and Computer-Assisted Intervention: Part I*, MICCAI '09, pages 67–74, Springer-Verlag, Berlin, Heidelberg, 2009, ISBN 978-3-642-04267-6.

[Bay et al., 2008] H. Bay, A. Ess, T. Tuytelaars and L. Van Gool. *Speeded-Up Robust Features (SURF).* Comput. Vis. Image Underst., vol. 110, no. 3, pages 346–359, 2008, ISSN 1077-3142.

[Bertails et al., 2006] F. Bertails, B. Audoly, M.-P. Cani, B. Querleux, F. Leroy and J.-L. Lévêque. *Super-helices for Predicting the Dynamics of Natural Hair.* In *ACM SIGGRAPH 2006 Papers*, SIGGRAPH '06, pages 1180–1187, 2006, ISBN 1-59593-364-6.

[Bookstein, 1989] F. L. Bookstein. *Principal Warps: Thin-Plate Splines and the Decomposition of Deformations.* IEEE Trans. Pattern Anal. Mach. Intell., vol. 11, no. 6, pages 567–585, 1989, ISSN 0162-8828.

[Bosman et al., 2014] J. Bosman, N. Haouchine, J. Dequidt, I. Peterlik, S. Cotin and C. Duriez. *The Role of Ligaments: Patient-Specific or Scenario-Specific ?* In *International Symposium on Biomedical Simulation 2014*, 2014.

[Bouguet, 2002] J. Y. Bouguet. *Pyramidal Implementation of the Lucas Kanade Feature Tracker: Description of the algorithm.* 2002.

[Bro-nielsen and Cotin, 1996] M. Bro-nielsen and S. Cotin. *Real-time Volumetric Deformable Models for Surgery Simulation using Finite Elements and Condensation.* In *Computer Graphics Forum*, pages 57–66, 1996.

[Bruyns et al., 2002] C. Bruyns, S. Senger, A. Menon, K. Montgomery, S. Wildermuth and R. Boyle. *A survey of interactive mesh-cutting techniques and a new method for implementing generalized interactive mesh cutting using virtual tools.* Journal of Visualization and Computer Animation, vol. 13, no. 1, pages 21–42, 2002.

[Chang et al., 2013] P.-L. Chang, D. Stoyanov, A. Davison and P. E. Edwards. *Real-Time Dense Stereo Reconstruction Using Convex Optimisation with a Cost-Volume for Image-Guided Robotic Surgery.* In *Medical Image Computing and Computer-Assisted Intervention - MICCAI 2013*, vol. 8149, pages 42–49, 2013, ISBN 978-3-642-40810-6.

[Chun and Höllerer, 2013] W. H. Chun and T. Höllerer. *Real-time Hand Interaction for Augmented Reality on Mobile Phones.* In *IUI*, pages 307–314, 2013, ISBN 978-1-4503-1965-2.

[Clements and et al., 2008] L. W. Clements and et al.. *Robust surface registration using salient anatomical features for image-guided liver surgery: Algorithm and validation.* Medical Physics, vol. 35, no. 6, 2008.

[Collins and Bartoli, 2011] B. C. Collins, T. and A. Bartoli. *Deformable Shape-from-Motion in Laparoscopy using a Rigid Sliding Window.* In *Medical Image Understanding and Analysis Conference*, 2011.

[Collins and Bartoli, 2012a] T. Collins and A. Bartoli. *3D Reconstruction in Laparoscopy with Close-Range Photometric Stereo.* In *Medical Image Computing and Computer-Assisted Intervention - MICCAI 2012*, vol. 7511 of *Lecture Notes in Computer Science*, edited by N. Ayache, H. Delingette, P. Golland and K. Mori, pages 634–642, Springer Berlin Heidelberg, 2012a, ISBN 978-3-642-33417-7.

[Collins and Bartoli, 2012b] T. Collins and A. Bartoli. *Towards Live Monocular 3D Laparoscopy Using Shading and Specularity Information.* In *Information Processing in Computer-Assisted Interventions*, vol. 7330, pages 11–21, 2012b, ISBN 978-3-642-30617-4.

[Comas et al., 2008] O. Comas, Z. Taylor, J. Allard, S. Ourselin, S. Cotin and J. Passenger. *Efficient Nonlinear FEM for Soft Tissue Modelling and Its GPU Implementation within the Open Source Framework SOFA*. In *Biomedical Simulation*, vol. 5104 of *Lecture Notes in Computer Science*, pages 28–39, 2008, ISBN 978-3-540-70520-8.

[Cootes et al., 1995] T. F. Cootes, C. J. Taylor, D. H. Cooper and J. Graham. *Active Shape Models&Mdash;Their Training and Application*. Comput. Vis. Image Underst., vol. 61, no. 1, pages 38–59, 1995, ISSN 1077-3142.

[Cotin et al., 1999] S. Cotin, H. Delingette and N. Ayache. *Real-time elastic deformations of soft tissues for surgery simulation*. Visualization and Computer Graphics, IEEE Transactions on, vol. 5, no. 1, pages 62–73, 1999, ISSN 1077-2626.

[Courtecuisse et al., 2012] H. Courtecuisse, P. Kerfriden, C. Duriez, J. Allard, S. P. A. Bordas and S. Cotin. *Real-time simulation of surgical cutting in biological tissues using a semi-implicit time integration scheme*. In *ACME 2012*, 2012.

[Courtecuisse et al., 2014] H. Courtecuisse, J. Allard, P. Kerfriden, S. P. Bordas, S. Cotin and C. Duriez. *Real-time simulation of contact and cutting of heterogeneous soft-tissues*. Medical Image Analysis, vol. 18, no. 2, pages 394 – 410, 2014, ISSN 1361-8415.

[Dagon et al., 2008] B. Dagon, C. Baur and V. Bettschart. *A framework for intraoperative update of 3D deformable models in liver surgery*. In *Engineering in Medicine and Biology Society, 2008. EMBS 2008. 30th Annual International Conference of the IEEE*, pages 3235–3238, IEEE, 2008.

[Dequidt et al., 2008] J. Dequidt, M. Marchal, C. Duriez, E. Kerien and S. Cotin. *Interactive Simulation of Embolization Coils: Modeling and Experimental Validation*. In *Medical Image Computing and Computer-Assisted Intervention - MICCAI 2008*, vol. 5241 of *Lecture Notes in Computer Science*, pages 695–702, Springer Berlin Heidelberg, 2008, ISBN 978-3-540-85987-1.

[Duriez et al., 2006] C. Duriez, S. Cotin, J. Lenoir and P. Neumann. *New approaches to catheter navigation for interventional radiology simulation*. Computer Aided Surgery, 2006.

[Elhawary and Popovic, 2010a] H. Elhawary and A. Popovic. *Robust feature tracking on the beating heart for a robotic-guided endoscope*. Int J Med Robot., pages 459–468, 2010a.

[Elhawary and Popovic, 2010b] H. Elhawary and A. Popovic. *Robust feature tracking on the beating heart for a robotic-guided endoscope*. Int J Med Robot., pages 459–468, 2010b.

[Faure et al., 2012] F. Faure, C. Duriez, H. Delingette, J. Allard, B. Gilles, S. Marchesseau, H. Talbot, H. Courtecuisse, G. Bousquet, I. Peterlik and S. Cotin. *SOFA: A Multi-Model Framework for Interactive Physical Simulation.* In *Soft Tissue Biomechanical Modeling for Computer Assisted Surgery*, edited by Y. Payan, Springer, 2012, ISBN 978-3-642-29013-8.

[Felippa and Haugen, 2005] C. Felippa and B. Haugen. *A unified formulation of small-strain corotational finite elements: I. Theory.* Computer Methods in Applied Mechanics and Engineering, vol. 194, no. 21, pages 2285–2335, 2005.

[Figl et al., 2010] M. Figl, D. Rueckert, D. Hawkes, R. Casula, M. Hu, O. Pedro, D. P. Zhang, G. Penney, F. Bello and P. Edwards. *Image guidance for robotic minimally invasive coronary artery bypass.* Computerized Medical Imaging and Graphics, vol. 34, no. 1, pages 61–68, 2010, ISSN 0895-6111.

[Fischer et al., 2007] J. Fischer, M. Eichlera, D. Bartza and S. W.. *A hybrid tracking method for surgical augmented reality.* Computer and Graphics, vol. 31, no. 1, pages 39–52, 2007.

[Fuchs et al., 1998] H. Fuchs, M. A. Livingston, R. Raskar, D. Colucci, K. Keller, A. State, J. R. Crawford, P. Rademacher, S. H. Drake and A. A. Meyer. *Augmented reality visualization for laparoscopic surgery.* In *Proceedings of the First International Conference on Medical Image Computing and Computer-Assisted Intervention*, pages 934 – 943, 1998.

[Gao et al., 2009] Z. Gao, T. Kim, D. L. James and J. P. Desai. *Semi-automated soft-tissue acquisition and modeling forsurgical simulation.* In *Proceedings of the fifth annual IEEE international conference on Automation science and engineering*, CASE'09, pages 268–273, IEEE Press, Piscataway, NJ, USA, 2009, ISBN 978-1-4244-4578-3.

[Gauglitz et al., 2011] S. Gauglitz, T. HÃ¶llerer and M. Turk. *Evaluation of Interest Point Detectors and Feature Descriptors for Visual Tracking.* International Journal of Computer Vision, vol. 94, no. 3, pages 335–360, 2011, ISSN 0920-5691.

[Gay-Bellile et al., 2010] V. Gay-Bellile, A. Bartoli and P. Sayd. *Direct Estimation of Nonrigid Registrations with Image-Based Self-Occlusion Reasoning.* IEEE Trans. Pattern Anal. Mach. Intell., vol. 32, no. 1, pages 87–104, 2010, ISSN 0162-8828.

[Giannarou et al., 2013] S. Giannarou, M. Visentini-Scarzanella and G.-Z. Yang. *Probabilistic Tracking of Affine-Invariant Anisotropic Regions.* Pattern Analysis and Machine Intelligence, IEEE Transactions on, vol. 35, no. 1, pages 130–143, 2013, ISSN 0162-8828.

[Gibson and Mirtich, 1997] S. F. Gibson and B. Mirtich. *A survey of deformable modeling in computer graphics*. Tech. rep., Mitsubishi Electronic Research Laboratory, 1997.

[Groch et al., 2012] A. Groch, S. Haase, M. Wagner, T. Kilgus, H. Kenngott, H. Schlemmer, J. Hornegger, H. Meinzer and L. Maier-Hein. *A probabilistic approach to fusion of Time-of-Flight and multiple view based 3D surface reconstruction for laparoscopic interventions*. In *International Conference on Computer Assisted Radiology and Surgery (CARS)*, pages 397 – 398, 2012.

[Guébert et al., 2008] C. Guébert, C. Duriez and L. Grisoni. *Unified processing of constraints for interactive simulation*. In *Workshop in Virtual Reality Interactions and Physical Simulation VRIPHYS' 2008*, edited by M. T. François Faure, pages –, Eurographics association, Grenoble, France, 2008.

[Haouchine et al., 2012] N. Haouchine, J. Dequidt, E. Kerrien, M.-O. Berger and S. Cotin. *Physics-based Augmented Reality for 3D Deformable Object*. In *VRIPHYS - Virtual Reality Interaction and Physical Simulation*, pages 31–38, Darmstadt, Germany, 2012.

[Haouchine et al., 2013a] N. Haouchine, J. Dequidt, M.-O. Berger and S. Cotin. *Deformation-based Augmented Reality for Hepatic Surgery*. In *MMVR 20 - Medecine Meets Virtual Reality*, pages 182–188, San Diego, USA, 2013a.

[Haouchine et al., 2013b] N. Haouchine, J. Dequidt, I. Peterlik, E. Kerrien, M.-O. Berger and S. Cotin. *Image-guided simulation of heterogeneous tissue deformation for augmented reality during hepatic surgery*. In *Mixed and Augmented Reality (ISMAR), 2013 IEEE International Symposium on*, pages 199–208, 2013b.

[Haouchine et al., 2014a] N. Haouchine, S. Cotin, J. Dequidt, E. Kerrien and M.-O. Berger. *Réalité augmentée pour la chirurgie minimalement invasive du foie utilisant un modèle biomécanique guidé par l'image*. In *Reconnaissance de Formes et Intelligence Artificielle (RFIA) 2014*, 2014a.

[Haouchine et al., 2014b] N. Haouchine, S. Cotin, I. Peterlik, J. Dequidt, M. Sanz Lopez, E. Kerrien and M.-O. Berger. *Impact of Soft Tissue Heterogeneity on Augmented Reality for Liver Surgery*. Visualization and Computer Graphics, IEEE Transactions on, 2014b.

[Haouchine et al., 2014c] N. Haouchine, J. Dequidt, M.-O. Berger and S. Cotin. *Single View Augmentation of 3D Elastic Objects*. In *Mixed and Augmented Reality (ISMAR), 2014 IEEE International Symposium on*, 2014c.

[Haouchine et al., 2014d] N. Haouchine, J. Dequidt, I. Peterlik, E. Kerrien, M.-O. Berger and S. Cotin. *Towards an Accurate Tracking of Liver Tumors for Robotic*

Assisted Surgery. In *Robotic and Automotion (ICRA), 2014 IEEE International Conference on*, 2014d.

[Haouchine et al., 2015] N. Haouchine, J. Dequidt, A. Bilger, M.-O. Berger and S. Cotin. *Elastic Augmented Reality from a Single View*. Visualization and Computer Graphics, IEEE Transactions on (Submitted), 2015.

[Hartley and Sturm, 1995] R. Hartley and P. Sturm. *Triangulation*. In *Computer Analysis of Images and Patterns*, vol. 970 of *Lecture Notes in Computer Science*, pages 190–197, Springer Berlin Heidelberg, 1995, ISBN 978-3-540-60268-2.

[Hartley and Zisserman, 2004] R. I. Hartley and A. Zisserman. *Multiple View Geometry in Computer Vision*. Cambridge University Press, ISBN: 0521540518, second ed., 2004.

[Hauth et al., 2003] M. Hauth, O. Etzmuss and W. Strasser. *Analysis of numerical methods for the simulation of deformable models*. The Visual Computer, vol. 19, no. 7-8, pages 581–600, 2003, ISSN 0178-2789.

[Herrera et al., 2013] S. Herrera, A. Malti, O. Morel and A. Bartoli. *Shape-from-Polarization in laparoscopy*. In *Biomedical Imaging (ISBI), 2013 IEEE 10th International Symposium on*, pages 1412–1415, 2013, ISSN 1945-7928.

[Hilsmann et al., 2010] A. Hilsmann, D. C. Schneider and P. Eisert. *Realistic cloth augmentation in single view video under occlusions*. Comput. Graph., vol. 34, no. 5, pages 567–574, 2010, ISSN 0097-8493.

[Hu et al., 2007] M. Hu, G. Penney, P. Edwards, M. Figl and D. Hawkes. *3D Reconstruction of Internal Organ Surfaces for Minimal Invasive Surgery*. In *Medical Image Computing and Computer-Assisted Intervention - MICCAI 2007*, vol. 4791 of *Lecture Notes in Computer Science*, edited by N. Ayache, S. Ourselin and A. Maeder, pages 68–77, 2007, ISBN 978-3-540-75756-6.

[Hungr et al., 2012] N. Hungr, M. Baumann, J.-A. Long and J. Troccaz. *A 3-D Ultrasound Robotic Prostate Brachytherapy System With Prostate Motion Tracking*. Robotics, IEEE Transactions on, vol. 28, no. 6, pages 1382–1397, 2012, ISSN 1552-3098.

[Ibai et al., 2014] L. Ibai, A. Hugo, A. Iker and B. Diego. *Real-time Deformation, Registration and Tracking of Solids Based on Physical Simulation*. In *Mixed and Augmented Reality (ISMAR), 2014 IEEE International Symposium on*, 2014.

[James and Pai, 1999] D. L. James and D. K. Pai. *ArtDefo: Accurate Real Time Deformable Objects*. In *Proceedings of the 26th Annual Conference on Computer Graphics and Interactive Techniques*, SIGGRAPH '99, pages 65–72, ACM

Press/Addison-Wesley Publishing Co., New York, NY, USA, 1999, ISBN 0-201-48560-5.

[Janie Fuller et al., 2003] D. Janie Fuller, P. Walter Scott, M. Binita Ashar and M. F. C. Julia Corrado. *Laparoscopic Trocar Injuries.* Tech. rep., A report from a U.S. Food and Drug Administration (FDA) Center for Devices and Radiological Health (CDRH) Systematic Technology Assessment of Medical Products (STAMP), 2003.

[Kass et al., 1988a] M. Kass, A. Witkin and D. Terzopoulos. *Snakes: Active contour models.* International Journal of Computer Vision, vol. 1, no. 4, pages 321–331, 1988a, ISSN 0920-5691.

[Kass et al., 1988b] M. Kass, A. Witkin and D. Terzopoulos. *Snakes: Active contour models.* International Journal of Computer Vision, vol. 1, no. 4, pages 321–331, 1988b, ISSN 0920-5691.

[Kerdok, 2006] A. E. Kerdok. *Characterizing the Nonlinear Mechanical Response of Liver to Surgical Manipulation.* 2006.

[Kerdok et al., 2006] A. E. Kerdok, M. P. Ottensmeyer and R. D. Howe. *Effects of Perfusion on the Viscoelastic Characteristics of Liver.* Journal of Biomechanics, vol. 39, pages 2221–2231, 2006.

[Kikuuwe et al., 2009] R. Kikuuwe, H. Tabuchi and M. Yamamoto. *An edge-based computationally efficient formulation of Saint Venant-Kirchhoff tetrahedral finite elements.* ACM Transactions on Graphics (TOG), vol. 28, no. 1, page 8, 2009.

[Kim et al., 2012a] J.-H. Kim, A. Bartoli, T. Collins and R. Hartley. *Tracking by detection for interactive image augmentation in laparoscopy.* In *Proceedings of the 5th international conference on Biomedical Image Registration*, WBIR'12, pages 246–255, 2012a, ISBN 978-3-642-31339-4.

[Kim et al., 2012b] J.-H. Kim, A. Bartoli, T. Collins and R. Hartley. *Tracking by Detection for Interactive Image Augmentation in Laparoscopy.* In *Biomedical Image Registration*, vol. 7359 of *Lecture Notes in Computer Science*, edited by B. Dawant, G. Christensen, J. Fitzpatrick and D. Rueckert, pages 246–255, Springer Berlin Heidelberg, 2012b, ISBN 978-3-642-31339-4.

[Klein, 2006] G. Klein. *Visual tracking for augmented reality.* 2006.

[L. Soler, 2000] G. M. N. A.-C. K. J.-M. C. O. D. J. M. L. Soler, H. Delingette. *cover An Automatic Virtual Patient Reconstruction from CT-Scans for Hepatic Surgical Planning.* In *Studies in Health Technology and Informatics*, pages 316–322, 2000.

[Levin, 2004] D. Levin. *Mesh-Independent Surface Interpolation.* In *Geometric Modeling for Scientific Visualization*, edited by G. Brunnett, B. Hamann, H. MÃ¼ller and L. Linsen, Mathematics and Visualization, pages 37–49, Springer Berlin Heidelberg, 2004, ISBN 978-3-642-07263-5.

[Lim and Yang, 12005] J. Lim and M. Yang. *A direct method for modeling non-rigid motion with thin plate spline.* In *Proceedings of IEEE Conference on Computer Vision and Pattern Recognition (CVPR'05)*, pages 1196–1202, 12005.

[Lindstrom, 2010] P. Lindstrom. *Triangulation made easy.* In *Computer Vision and Pattern Recognition (CVPR), 2010 IEEE Conference on*, pages 1554–1561, 2010, ISSN 1063-6919.

[Lowe, 2004a] D. Lowe. *Distinctive Image Features from Scale-Invariant Keypoints.* International Journal of Computer Vision, vol. 60, no. 2, pages 91–110, 2004a, ISSN 0920-5691.

[Lowe, 2004b] D. G. Lowe. *Distinctive Image Features from Scale-Invariant Keypoints.* Int. J. Comput. Vision, vol. 60, no. 2, pages 91–110, 2004b, ISSN 0920-5691.

[Lucas and Kanade, 1981a] B. D. Lucas and T. Kanade. *An iterative image registration technique with an application to stereo vision.* In *Proceedings of the 7th international joint conference on Artificial intelligence - Volume 2*, IJCAI'81, pages 674–679, Morgan Kaufmann Publishers Inc., San Francisco, CA, USA, 1981a.

[Lucas and Kanade, 1981b] B. D. Lucas and T. Kanade. *An iterative image registration technique with an application to stereo vision.* In *Proceedings of the 7th international joint conference on Artificial intelligence - Volume 2*, IJCAI'81, pages 674–679, Morgan Kaufmann Publishers Inc., San Francisco, CA, USA, 1981b.

[M. Agrawal and Blas, 2008] K. K. M. Agrawal and M. Blas. *Censure: Center surround extremas for realtime feature detection and matching.* In *Computer Vision ECCV, 2008*, vol. 5305 of *Lecture Notes in Computer Science*, pages 102–115, 2008.

[M. Calonder and Fua, 2010] C. S. M. Calonder, V. Lepetit and P. Fua. *BRIEF: Binary robust independent elementary features.* In *Computer Vision ECCV, 2010*, vol. 6314 of *Lecture Notes in Computer Science*, pages 778–792, 2010.

[Maier-Hein et al., 2013] L. Maier-Hein, P. Mountney, A. Bartoli, H. Elhawary, D. Elson, A. Groch, A. Kolb, M. Rodrigues, J. Sorger, S. Speidel and D. Stoyanov. *Optical techniques for 3D surface reconstruction in computer-assisted laparoscopic surgery.* MEDICAL IMAGE ANALYSIS, vol. 17, pages 974–996, 2013.

[Malti et al., 2012] A. Malti, A. Bartoli and T. Collins. *Template-Based Conformal Shape-from-Motion-and-Shading for Laparoscopy*. In *Information Processing in Computer-Assisted Interventions*, vol. 7330, pages 1–10, 2012, ISBN 978-3-642-30617-4.

[Malti et al., 2013] A. Malti, R. Hartley, A. Bartoli and J.-H. Kim. *Monocular Template-Based 3D Reconstruction of Extensible Surfaces with Local Linear Elasticity*. In *Computer Vision and Pattern Recognition (CVPR), 2013 IEEE Conference on*, pages 1522–1529, 2013, ISSN 1063-6919.

[Marchesseau et al., 2010] S. Marchesseau, T. Heimann, S. Chatelin, R. Willinger and H. Delingette. *Multiplicative Jacobian Energy Decomposition Method for Fast Porous Visco-Hyperelastic Soft Tissue Model*. In *MICCAI 2010*, vol. 6361 of *LNCS*, pages 235–242, 2010, ISBN 978-3-642-15704-2.

[Marescaux, 2004] J. Marescaux. *Augmented reality assisted laparoscopic adrenalectomy*. Journal of American Medical Association, vol. 292, no. 18, pages 2214–2215, 2004.

[Marescaux et al., 1997] J. Marescaux, J. M. Clement, M. Nord, Y. Russier, V. Tassetti, D. Mutter, S. Cotin and N. Ayache. *[A new concept in digestive surgery: the computer assisted surgical procedure, from virtual reality to telemanipulation]*. Bull Acad Natl Med, vol. 181, no. 8, pages 1609–21, 1997.

[Marvik et al., 2005] R. Marvik, T. Lango, G. Tangen, F. Lindseth, Y. Yavuz and T. N. Hernes. *Image-guided laparoscopic surgery, review and current status*. Minerva Chirurgica, vol. 60, pages 305–325, 2005.

[Matas et al., 2004] J. Matas, O. Chum, M. Urban and T. Pajdla. *Robust wide-baseline stereo from maximally stable extremal regions*. Image and Vision Computing, vol. 22, no. 10, pages 761 – 767, 2004, ISSN 0262-8856, british Machine Vision Computing 2002.

[Maton et al., 1994] A. Maton, J. Hopkins, S. Johnson, M. Q. W. David LaHart Charles William McLaughlin and J. D. Wright. *Human Biology and Health*. Prentice Hall, 1994.

[Matthews and Baker, 2004] I. Matthews and S. Baker. *Active Appearance Models Revisited*. Int. J. Comput. Vision, vol. 60, no. 2, pages 135–164, 2004, ISSN 0920-5691.

[Maurice et al., 2011] X. Maurice, P. Graebling and C. Doignon. *Real-time structured light coding for adaptive patterns*. Journal of Real-Time Image Processing, pages 1–10, 2011, ISSN 1861-8200.

[Mikolajczyk and Schmid, 2005] K. Mikolajczyk and C. Schmid. *A performance evaluation of local descriptors*. Pattern Analysis and Machine Intelligence, IEEE Transactions on, vol. 27, no. 10, pages 1615–1630, 2005.

[Mikolajczyk et al., 2005] K. Mikolajczyk, T. Tuytelaars, C. Schmid, A. Zisserman, J. Matas, F. Schaffalitzky, T. Kadir and L. V. Gool. *A Comparison of Affine Region Detectors*. Int. J. Comput. Vision, vol. 65, no. 1-2, pages 43–72, 2005, ISSN 0920-5691.

[Miller, 1988] G. S. P. Miller. *The motion dynamics of snakes and worms*. In *In Proceedings of ACM SIGGRAPH 1988*, pages 169–173, 1988.

[Miller and Lu, 2013] K. Miller and J. Lu. *On the prospect of patient-specific biomechanics without patient-specific properties of tissues*. Journal of the Mechanical Behavior of Biomedical Materials, vol. 27, no. 0, pages 154 – 166, 2013, ISSN 1751-6161.

[Miller et al., 2007] K. Miller, G. Joldes, D. Lance and A. Wittek. *Total Lagrangian explicit dynamics finite element algorithm for computing soft tissue deformation*. Communications in Numerical Methods in Engineering, vol. 23, no. 2, pages 121–134, 2007, ISSN 1099-0887.

[Moreno-Noguer et al., 2009] F. Moreno-Noguer, M. Salzmann, V. Lepetit and P. Fua. *Capturing 3D stretchable surfaces from single images in closed form*. In *Computer Vision and Pattern Recognition, 2009. CVPR 2009. IEEE Conference on*, pages 1842–1849, 2009, ISSN 1063-6919.

[Mountney and Yang, 2010] P. Mountney and G.-Z. Yang. *Motion Compensated SLAM for Image Guided Surgery*. In *Medical Image Computing and Computer-Assisted Intervention - MICCAI 2010*, vol. 6362 of *Lecture Notes in Computer Science*, edited by T. Jiang, N. Navab, J. Pluim and M. Viergever, pages 496–504, 2010, ISBN 978-3-642-15744-8.

[Mountney et al., 2006] P. Mountney, D. Stoyanov, A. Davison and G.-Z. Yang. *Simultaneous Stereoscope Localization and Soft-Tissue Mapping for Minimal Invasive Surgery*. In *Medical Image Computing and Computer-Assisted Intervention - MICCAI 2006*, vol. 4190 of *Lecture Notes in Computer Science*, edited by R. Larsen, M. Nielsen and J. Sporring, pages 347–354, 2006, ISBN 978-3-540-44707-8.

[Mountney et al., 2010] P. Mountney, D. Stoyanov and G.-Z. Yang. *Three-Dimensional Tissue Deformation Recovery and Tracking*. Signal Processing Magazine, IEEE, vol. 27, no. 4, pages 14–24, 2010, ISSN 1053-5888.

[Müller and Gross, 2004] M. Müller and M. Gross. *Interactive Virtual Materials*. In *Proceedings of Graphics Interface 2004*, GI '04, pages 239–246, 2004, ISBN 1-56881-227-2.

[Müller et al., 2013] M. Müller, N. Chentanez and T.-Y. Kim. *Real time dynamic fracture with volumetric approximate convex decompositions*. ACM Transactions on Graphics (TOG), vol. 32, no. 4, page 115, 2013.

[Nealen et al., 2006] A. Nealen, M. Müller, R. Keiser, E. Boxerman and M. Carlson. *Physically based deformable models in computer graphics*. In *Computer Graphics Forum*, vol. 25 (4), pages 809–836, Wiley Online Library, 2006.

[Nesme et al., 2005] M. Nesme, Y. Payan and F. Faure. *Efficient, Physically Plausible Finite Elements*. In *Eurographics 2005, Short papers, August, 2005*, edited by J. Dingliana and F. Ganovelli, Trinity College, Dublin, Irlande, 2005.

[Nicolas Aspert, 2002] T. E. Nicolas Aspert, Diego Santa-Cruz. *MESH : MEASURING ERRORS BETWEEN SURFACES USING THE HAUSDORFF DISTANCE*. In *IEEE International Conference in Multimedia and Expo*, 2002.

[Nicolau et al., 2011] S. Nicolau, L. Soler, D. Mutter and J. Marescaux. *Augmented reality in laparoscopic surgical oncology*. Surgical Oncology, vol. 20, no. 3, pages 189 – 201, 2011, ISSN 0960-7404.

[Oktay et al., 2013] O. Oktay, L. Zhang, T. Mansi, P. Mountney, P. Mewes, S. Nicolau, L. Soler and C. Chefd'hotel. *Biomechanically Driven Registration of Pre- to Intra-Operative 3D Images for Laparoscopic Surgery*. In *MICCAI 2013*, vol. 8150, 2013, ISBN 978-3-642-40762-8.

[Peng et al., 2009] Y. Peng, M. Zheng, Q. Ye, X. Chen, B. Yu and B. Liu. *Heated and humidified CO2 prevents hypothermia, peritoneal injury, and intra-abdominal adhesions during prolonged laparoscopic insufflations*. Jounrla of Surgical Research, vol. 141, pages 40–7, 2009.

[Penne et al., 2009] J. Penne, K. Holler, M. Sturmer, T. Schrauder, A. Schneider, R. Engelbrecht, H. Feussner, B. Schmauss and J. Hornegger. *Time-of-Flight 3-D Endoscopy*. In *Medical Image Computing and Computer-Assisted Intervention - MICCAI 2009*, vol. 5761 of *Lecture Notes in Computer Science*, edited by G.-Z. Yang, D. Hawkes, D. Rueckert, A. Noble and C. Taylor, pages 467–474, Springer Berlin Heidelberg, 2009, ISBN 978-3-642-04267-6.

[Perriollat et al., 2011] M. Perriollat, R. Hartley and A. Bartoli. *Monocular Template-based Reconstruction of Inextensible Surfaces*. International Journal of Computer Vision, vol. 95, no. 2, pages 124–137, 2011, ISSN 0920-5691.

[Peterlík et al., 2012] I. Peterlík, C. Duriez and S. Cotin. *Modeling and real-time simulation of a vascularized liver tissue.* In *Medical Image Computing and Computer-Assisted Intervention*, pages 50–57, Springer-Verlag, 2012, ISBN 978-3-642-33414-6.

[Picinbono et al., 2003] G. Picinbono, H. Delingette and N. Ayache. *Non-linear anisotropic elasticity for real-time surgery simulation.* Graphical Models, vol. 65, no. 5, pages 305 – 321, 2003, ISSN 1524-0703, special Issue on {SMI} 2002.

[Pilet et al., 2008] J. Pilet, V. Lepetit and P. Fua. *Fast Non-Rigid Surface Detection, Registration and Realistic Augmentation.* Int. J. Comput. Vision, vol. 76, no. 2, pages 109–122, 2008, ISSN 0920-5691.

[Pizarro and Bartoli, 2012] D. Pizarro and A. Bartoli. *Feature-Based Deformable Surface Detection with Self-Occlusion Reasoning.* International Journal of Computer Vision, vol. 97, no. 1, pages 54–70, 2012, ISSN 0920-5691.

[Plantefeve et al., 2014] R. Plantefeve, N. Haouchine, J.-P. Radoux and S. Cotin. *Automatic Alignment of pre and intraoperative Data using Anatomical Landmarks for Augmented Laparoscopic Liver Surgery.* In *International Symposium on Biomedical Simulation 2014*, 2014.

[Pratt et al., 2010] P. Pratt, D. Stoyanov, M. Visentini-Scarzanella and G.-Z. Yang. *Dynamic Guidance for Robotic Surgery Using Image-Constrained Biomechanical Models.* In *Medical Image Computing and Computer-Assisted Intervention*, vol. 6361, pages 77–85, 2010, ISBN 978-3-642-15704-2.

[Przemieniecki, 1985] J. S. Przemieniecki. *Theory of Matrix Structural Analysis.* 1985, ISBN 0-486-64948-2, reprint of McGraw Hill, 1968.

[Puerto, 2011] A. M.-C. J. M. G. Puerto, G.. *Adaptive multi-affine (AMA) feature-matching algorithm and its application to minimally-invasive surgery images.* In *Proc. IEEE/RSJ Int. Conf. Intel. Rob. Syst. 2011*, page 2371, 2011.

[Puerto and Mariottini, 2012] G. Puerto and G.-L. Mariottini. *A Comparative Study of Correspondence-Search Algorithms in MIS Images.* In *Medical Image Computing and Computer-Assisted Intervention - MICCAI 2012*, vol. 7511 of *Lecture Notes in Computer Science*, edited by N. Ayache, H. Delingette, P. Golland and K. Mori, pages 625–633, Springer Berlin Heidelberg, 2012, ISBN 978-3-642-33417-7.

[Puerto-Souza and Mariottini, 2013] G. Puerto-Souza and G. Mariottini. *Toward long-term and accurate Augmented-Reality display for minimally-invasive surgery.*

In *Robotics and Automation (ICRA), 2013 IEEE International Conference on*, pages 5384–5389, 2013, ISSN 1050-4729.

[Richa, 2010] R. Richa. *Robust 3D Motion Tracking for Robotic-Assisted Beating Heart Surgery*. Ph.D. thesis, Montpellier II University, 2010.

[Richa et al., 2010a] R. Richa, A. P. L. Bó and P. Poignet. *Robust 3D visual tracking for robotic-assisted cardiac interventions*. In *Proceedings of the 13th international conference on Medical image computing and computer-assisted intervention*, MICCAI2010, pages 267–274, Springer-Verlag, 2010a, ISBN 3-642-15704-1, 978-3-642-15704-2.

[Richa et al., 2010b] R. Richa, A. P. L. Bó and P. Poignet. *Robust 3d visual tracking for robotic-assisted cardiac interventions*. In *Proceedings of the 13th international conference on Medical image computing and computer-assisted intervention: Part I*, MICCAI'10, pages 267–274, Springer-Verlag, Berlin, Heidelberg, 2010b, ISBN 3-642-15704-1, 978-3-642-15704-2.

[Richa et al., 2010c] R. Richa, P. Poignet and C. Liu. *Three-dimensional Motion Tracking for Beating Heart Surgery Using a Thin-plate Spline Deformable Model*. Int. J. Rob. Res., vol. 29, no. 2-3, pages 218–230, 2010c, ISSN 0278-3649.

[Rohl et al.] S. Rohl, S. Bodenstedt, S. Suwelack, H. Kenngott, B. P. Muller-Stich and R. Dillmann. *Dense GPU-enhanced surface reconstruction from stereo endoscopic images for intraoperative registration*.

[Roth, 1982] S. D. Roth. *Ray casting for modeling solids*. Computer Graphics and Image Processing, vol. 18, no. 2, pages 109 – 144, 1982, ISSN 0146-664X.

[Rousseeuw and Leroy, 1987] P. J. Rousseeuw and A. M. Leroy. *Robust Regression and Outlier Detection*. Wiley Series in Probability and Mathematical Statistics, John Wiley and Sons, 1987.

[Rueckert et al., 1999] D. Rueckert, L. Sonoda, C. Hayes, D. Hill, M. Leach and D. Hawkes. *Nonrigid registration using free-form deformations: application to breast MR images*. Medical Imaging, IEEE Transactions on, vol. 18, no. 8, pages 712–721, 1999, ISSN 0278-0062.

[Saad, 2003] Y. Saad. *Iterative Methods for Sparse Linear Systems*. Society for Industrial and Applied Mathematics, Philadelphia, PA, USA, 2nd ed., 2003, ISBN 0898715342.

[Salzmann and Fua, 2011] M. Salzmann and P. Fua. *Linear Local Models for Monocular Reconstruction of Deformable Surfaces*. Pattern Analysis and Machine Intelligence, IEEE Transactions on, vol. 33, no. 5, pages 931–944, 2011, ISSN 0162-8828.

[Salzmann et al., 2007a] M. Salzmann, R. Hartley and P. Fua. *Convex Optimization for Deformable Surface 3-D Tracking.* In *Computer Vision, 2007. ICCV 2007. IEEE 11th International Conference on*, pages 1–8, 2007a, ISSN 1550-5499.

[Salzmann et al., 2007b] M. Salzmann, J. Pilet, S. Ilic and P. Fua. *Surface Deformation Models for Nonrigid 3D Shape Recovery.* IEEE Trans. Pattern Anal. Mach. Intell., vol. 29, no. 8, pages 1481–1487, 2007b, ISSN 0162-8828.

[Sanchez-Margallo et al., 2011] F. Sanchez-Margallo, J. Moyano-Cuevas, R. Latorre, J. Maestre, L. Correa, J. Pagador, L. Sanchez-Peralta, J. Sanchez-Margallo and J. Uson-Gargallo. *Anatomical changes due to pneumoperitoneum analyzed by MRI: an experimental study in pigs.* Surgical and Radiologic Anatomy, vol. 33, no. 5, pages 389–396, 2011, ISSN 0930-1038.

[Saupin et al., 2008] G. Saupin, C. Duriez and S. Cotin. *Contact Model for Haptic Medical Simulations.* In *Biomedical Simulation*, vol. 5104, pages 157–165, 2008, ISBN 978-3-540-70520-8.

[Schaerer et al., 2010] J. Schaerer, C. Casta, J. Pousin and P. Clarysse. *A dynamic elastic model for segmentation and tracking of the heart in {MR} image sequences.* Medical Image Analysis, vol. 14, no. 6, pages 738 – 749, 2010, ISSN 1361-8415.

[Sederberg and Parry, 1986] T. W. Sederberg and S. R. Parry. *Free-form Deformation of Solid Geometric Models.* SIGGRAPH Comput. Graph., vol. 20, no. 4, pages 151–160, 1986, ISSN 0097-8930.

[Selmi et al., 2013] S.-Y. Selmi, G. Fiard, E. Promayon, L. Vadcard and J. Troccaz. *A virtual reality simulator combining a learning environment and clinical case database for image-guided prostate biopsy.* In *Computer-Based Medical Systems (CBMS), 2013 IEEE 26th International Symposium on*, pages 179–184, 2013.

[Sermesant et al., 2003] M. Sermesant, C. Forest, X. Pennec, H. Delingette and N. Ayache. *Deformable biomechanical models: Application to 4D cardiac image analysis.* Medical Image Analysis, vol. 7, no. 4, pages 475–488, 2003.

[Shaji et al., 2011] A. Shaji, A. Varol, P. Fua, Yashoteja, A. Jain and S. Chandran. *Resolving occlusion in multiframe reconstruction of deformable surfaces.* In *Computer Vision and Pattern Recognition Workshops (CVPRW), 2011 IEEE Computer Society Conference on*, pages 31–36, 2011, ISSN 2160-7508.

[Shen et al., 2010] S. Shen, W. Shi and Y. Liu. *Monocular 3-D tracking of inextensible deformable surfaces under L2-norm.* Trans. Img. Proc., vol. 19, no. 2, pages 512–521, 2010, ISSN 1057-7149.

[Shen et al., 2011] T. Shen, H. Li and X. Huang. *Active Volume Models for Medical Image Segmentation*. IEEE Trans. Med. Imaging, vol. 30, no. 3, pages 774–791, 2011.

[Shi and Tomasi, 1994] J. Shi and C. Tomasi. *Good features to track*. In *Computer Vision and Pattern Recognition, 1994. Proceedings CVPR '94., 1994 IEEE Computer Society Conference on*, pages 593–600, 1994, ISSN 1063-6919.

[Sifakis and Barbic, 2012] E. Sifakis and J. Barbic. *FEM Simulation of 3D Deformable Solids: A Practitioner's Guide to Theory, Discretization and Model Reduction*. In *ACM SIGGRAPH 2012 Courses*, SIGGRAPH 2012, pages 20:1–20:50, ACM, New York, NY, USA, 2012, ISBN 978-1-4503-1678-1.

[Silcowitz-Hansen et al., 2010] M. Silcowitz-Hansen, S. Niebe and K. Erleben. *A Nonsmooth Nonlinear Conjugate Gradient Method for Interactive Contact Force Problems*. Vis. Comput., vol. 26, no. 6-8, pages 893–901, 2010, ISSN 0178-2789.

[Snavely et al., 2006] N. Snavely, S. M. Seitz and R. Szeliski. *Photo Tourism: Exploring Photo Collections in 3D*. In *ACM SIGGRAPH 2006 Papers*, SIGGRAPH '06, pages 835–846, ACM, New York, NY, USA, 2006, ISBN 1-59593-364-6.

[Speidel et al., 2011] S. Speidel, S. Roehl, S. Suwelack, R. Dillmann, H. Kenngott and B. Mueller-Stich. *Intraoperative surface reconstruction and biomechanical modeling for soft tissue registration*. In *Proc. Joint Workshop on New Technologies for Computer Robot Assisted Surgery*, 2011.

[Spillmann and Harders, 2012] J. Spillmann and M. Harders. *Robust Interactive Collision Handling Between Tools and Thin Volumetric Objects*. IEEE Transactions on Visualization and Computer Graphics, vol. 18, no. 8, pages 1241–1254, 2012, ISSN 1077-2626.

[Stephen and Eubanks, 2004] W. Stephen and M. Eubanks. *Mastery of Endoscopic and Laparoscopic Surgery*. Lippincott Williams and Wilkins, second ed., 2004.

[Stoyanov and Yang, 2005] A. D. Stoyanov, D. and G.-Z. Yang. *Laparoscope Self-calibration for Robotic Assisted Minimally Invasive Surgery*. In *Medical Image Computing and Computer-Assisted Intervention*, pages 114–121, 2005.

[Stoyanov, 2012] D. Stoyanov. *Stereoscopic scene flow for robotic assisted minimally invasive surgery*. In *Proceedings of the 15th international conference on Medical Image Computing and Computer-Assisted Intervention*, MICCAI2012, pages 479–486, Springer-Verlag, 2012, ISBN 978-3-642-33414-6.

[Stoyanov et al., 2005] D. Stoyanov, G. P. Mylonas, F. Deligianni, A. Darzi and G. Z. Yang. *Soft-tissue motion tracking and structure estimation for robotic assisted MIS procedures*. In *Proceedings of the 8th international conference on Medical image computing and computer-assisted intervention - Volume Part II*, MICCAI'05, pages 139–146, Springer-Verlag, Berlin, Heidelberg, 2005, ISBN 3-540-29326-4, 978-3-540-29326-2.

[Su et al., 2009] L.-M. Su, B. P. Vagvolgyi, R. Agarwal, C. E. Reiley, R. H. Taylor and G. D. Hager. *Augmented Reality During Robot-assisted Laparoscopic Partial Nephrectomy: Toward Real-Time 3D-CT to Stereoscopic Video Registration*. Urology, vol. 73, no. 4, pages 896 – 900, 2009, ISSN 0090-4295.

[Suthau and Hellwich, 2002] V. M.-H. P. M. H.-P. Suthau, T. and O. Hellwich. *A concept work for Augmented Reality visualisation based on a medical application in liver surgery*. The International Archives of Photogrammetry, Remote Sensing and Spatial Information Sciences, Proceedings ISPRS Commission V Symposium Corfu, vol. 34, no. 5, pages 274 – 280, 2002.

[Szekely et al., 2000] G. Szekely, C. Brechbuhler, R. Hutter, A. Rhomberg, N. Ironmonger and P. Schmid. *Modelling of soft tissue deformation for laparoscopic surgery simulation*. Medical Image Analysis, vol. 4, no. 1, pages 57 – 66, 2000, ISSN 1361-8415.

[Talbot et al., 2014] H. Talbot, F. Spadoni, C. Duriez, M. Sermesant, S. Cotin and H. Delingette. *Interactive Training System for Interventional Electrocardiology Procedures*. In *Biomedical Simulation*, vol. 8789 of *Lecture Notes in Computer Science*, edited by F. Bello and S. Cotin, pages 11–19, Springer International Publishing, 2014, ISBN 978-3-319-12056-0.

[Talbot et al., 2015] H. Talbot, N. Haouchine, J. Dequidt, I. Peterlik, C. Duriez, H. Delingette and S. Cotin. *Surgery Training, Planning and Guidance Using the SOFA Framework*. In *Eurogrpahics 2015, Medical Prize (Accepted)*, 2015.

[Teber et al., 2009] D. Teber, S. Guven, T. Simpfendorfer, M. Baumhauer, E. O. Guven, F. Yencilek, A. S. Gozen and J. Rassweiler. *Augmented Reality: A New Tool To Improve Surgical Accuracy during Laparoscopic Partial Nephrectomy? Preliminary In Vitro and In Vivo Results*. European Urology, vol. 56, no. 2, pages 332 – 338, 2009, ISSN 0302-2838.

[Teran et al., 2003] J. Teran, S. Blemker, V. N. T. Hing and R. Fedkiw. *Finite Volume Methods for the Simulation of Skeletal Muscle*. In *Proceedings of the 2003 ACM SIGGRAPH/Eurographics Symposium on Computer Animation*, SCA '03, pages 68–74, Eurographics Association, Aire-la-Ville, Switzerland, Switzerland, 2003, ISBN 1-58113-659-5.

[Terzopoulos et al., 1987] D. Terzopoulos, J. Platt, A. Barr and K. Fleischer. *Elastically Deformable Models.* SIGGRAPH Comput. Graph., vol. 21, no. 4, pages 205–214, 1987, ISSN 0097-8930.

[Toledo, 2003] S. Toledo. *Taucs:A library of sparse linear solvers.* 2003, `http://www.tau.ac.il/stoledo/taucs/`.

[Trefethen and Bau, 1997] L. N. Trefethen and D. Bau. *Numerical Linear Algebra.* SIAM, third ed., 1997.

[Umale et al., 2011] S. Umale, S. Chatelin, N. Bourdet, C. Deck, M. Diana, P. Dhumane, L. Soler, J. Marescaux and R. Willinger. *Experimental in vitro mechanical characterization of porcine Glisson's capsule and hepatic veins.* Journal of Biomechanics, vol. 44, no. 9, 2011, ISSN 0021-9290.

[Verscheure et al., 2013] L. Verscheure, L. Peyrodie, A. Dewalle, N. Reyns, N. Betrouni, S. Mordon and M. Vermandel. *Three-dimensional skeletonization and symbolic description in vascular imaging: preliminary results.* International Journal of Computer Assisted Radiology and Surgery, vol. 8, no. 2, pages 233–246, 2013, ISSN 1861-6410.

[Wang et al., 2007] F. Wang, L. Duratti, E. Samur, U. Spaelter and H. Bleuler. *A Computer-Based Real-Time Simulation of Interventional Radiology.* In *Engineering in Medicine and Biology Society, 2007. EMBS 2007. 29th Annual International Conference of the IEEE,* pages 1742–1745, 2007.

[Wesarg S., 2004] S. H. Z. P.-S. M. S. G. Wesarg S., Schwald B.. *An augmented reality system for supporting minimally invasive interventions.* In *Workshop Augmented Environments for Medical Imaging,* pages 41 – 48, 2004.

[Westebring et al., 2008] E. P. Westebring, R. H. M. Goossens, J. J. Jakimowicz and J. Dankelman. *Haptics in Minimally Invasive Surgery - A Review.* Minimally Invasive Therapy and Allied Technologies, vol. 17, pages 3–16, 2008.

[Wuhrer et al., 2012] S. Wuhrer, J. Lang and C. Shu. *Tracking Complete Deformable Objects with Finite Elements.* In *3DIMPVT,* pages 1–8, IEEE, 2012.

[Yamada, 1970] H. Yamada. *Strength of biological materials.* The williams and Wilkins Company, Baltimore, 1970.

[Yip et al., 2012] M. C. Yip, D. G. Lowe, S. E. Salcudean, R. N. Rohling and C. Y. Nguan. *Tissue Tracking and Registration for Image-Guided Surgery.* Medical Imaging, IEEE Transactions on, vol. 31, no. 11, pages 2169–2182, 2012, ISSN 0278-0062.

[Yushkevich et al., 2006] P. A. Yushkevich, J. Piven, H. Cody Hazlett, R. Gimpel Smith, S. Ho, J. C. Gee and G. Gerig. *User-Guided 3D Active Contour Segmentation of Anatomical Structures: Significantly Improved Efficiency and Reliability*. Neuroimage, vol. 31, no. 3, pages 1116–1128, 2006.

[Zhang, 2000] Z. Zhang. *A Flexible New Technique for Camera Calibration*. IEEE Trans. Pattern Anal. Mach. Intell., vol. 22, no. 11, pages 1330–1334, 2000, ISSN 0162-8828.

[Zhang and Zhang, 1997] Z. Zhang and Z. Zhang. *Parameter Estimation Techniques: A Tutorial with Application to Conic Fitting*. Image and Vision Computing, vol. 15, pages 59–76, 1997.

[Zhong et al., 2005] H. Zhong, M. P. Wachowiak and T. M. Peters. *A real time finite element based tissue simulation method incorporating nonlinear elastic behavior*. Computer Methods in Biomechanics and Biomedical Engineering, vol. 8, no. 3, pages 177–189, 2005.

[Zhu and Lyu, 2007] J. Zhu and M. R. Lyu. *Progressive finite newton approach to real-time nonrigid surface detection*. In *Computer Vision and Pattern Recognition, 2007. CVPR'07. IEEE Conference on*, pages 1–8, IEEE, 2007.